ABSTRACT

Title: ADVANCES IN CHARACTERIZING FIRE SPRINKLER SPRAYS

Ning Ren, PhD, 2010

Directed By: Andre Marshall, Associated Professor, Department of Fire Protection Engineering

Knowledge of the initial spray characteristics of sprinklers is critical for fire suppression performance analysis. Although numerous tests and studies have been conducted on fire sprinkler sprays, measurements were mostly conducted in the far-field due to spray diagnostics limitations. Although these far-field measurements are useful for evaluating the ultimate sprinkler performance, they are convoluted by the dispersion process and yield little useful information regarding the initial sprinkler discharge characteristics. With the development of advanced non-intrusive spray diagnostics, high fidelity initial spray measurements are possible, providing sprinkler discharge characteristics which are useful alone for nozzle development or together with analytical tools for prediction of suppression performance.

In this study, a laser diagnostic technique based on Shadowgraphy was used to characterize the initial spray for actual fire sprinklers and nozzles having more basic configurations. The shadowgraphs revealed important information on the effect of nozzle geometry on sheet formation (from the injected jet) and sheet fragmentation into drops. Three breakup modes were observed depending on the injection conditions quantified

through the *We* and the geometric details of the nozzle. Based on these breakup modes, scaling laws were developed to quantify the effect of nozzle geometry and injection condition on sheet breakup distance and drop size. The sheet breakup location followed a $We^{-1/3}$ power law for all observed breakup modes. However, drop sizes followed a $We^{-1/3}$ power law only for the ligament breakup mode which was observed to occur at very high *We* ($We > 10^4$). The shadowgraphs also provided spatially resolved measurements of drop size and velocity on a hemisphere 0.3 m away from the nozzle. Based on these detailed measurements, a comprehensive spray initiation model was developed for the purpose of providing a high fidelity analytical description of the initial spray useful for spray modeling. A simple dispersion analysis, accounting only for drag forces on the droplet in a quiescent environment, was performed to compare with volume density measurements taken 1 m below the sprinkler. Predicted and measured volume densities compared favorably providing some validation of the initial spray measurements and simple dispersion analysis.

ADVANCES IN CHARACTERIZING FIRE SPRINKLER SPRAYS

By

Ning Ren

Dissertation submitted to the Faculty of the Graduate School of the
University of Maryland, College Park, in partial fulfillment
of the requirements for the degree of
Doctor of philosophy
2010

Advisory Committee:
Professor André W. Marshall (FPE/ME), Chair
Professor Arnaud Trouvé (FPE/ME)
Professor James Quintiere (FPE/ME)
Professor Kenneth Kiger (ME)
Professor Sheryl Ehrman (ChBE) Dean's representative

Acknowledgements

First of all, I want to thank my advisor, Professor Marshall for his guidance support and countless time to help me to complete this work. One of the methodologies in this study is initiated by Prof. Howard Baum. I want to thanks Prof. Baum for his support.

This work is supported by FM Global. I would like to thank the program manager Dr. Burt Yu for his support for this project and my research work.

I would like to thank the rest of my committee members Professor Arnaud Trouvé, Professor James Quintiere, Professor Kenneth Kiger and Professor Sheryl Ehrman for their support and valuable suggestions for my PhD study.

During my five years of Ph.D study, a lot of friends have been working with me in this project. They are Andy Blum, Chi Do, Yinghui Zheng, Bryan Saylers, Paolo Santangelo, Géraldine Steger, Fredric. Especially, I would like to thank my major partner Andy Blum, Chi Do for sharing the ideas and data in the last several years. In addition, I would like to emphasis the help from visiting scholars from France, Géraldine Steger who spend a whole summer help me measure the volume flux, and Fredric who spend a lot of time help me characterizing the sheet breakup locations.

I also would like to thank all my friends, especially Sherri, Walid, Haiwen Ding, Charles Chen and Paolo Santangelo, in the Department of Fire Protection Engineering for their assistance and encouragement during my study.

Finally, I would like to thank my parents who support me all the time. Without their encouragement and support, I cannot achieve my goal and finish my work.

Table of Contents

List of Figures

List of Tables

Nomenclature

A	Wave amplitude, m
A_0	Initial wave amplitude, m
a_n	Coefficient for Fourier cosine function
LDD	Spray actual delivered density (mm/min or L/m^{2}S)
C	Coefficient
C_d	Drag coefficient
C_n	Coefficient for Legendre polynomials
C_N	Coefficient related on number of droplet per injection
c_p	Specific heat, J/kgK
CVF	Cumulative volume fraction
d	Droplet diameter, mm
d_{10}	Spray arithmetic mean diameter, mm
d_{30}	Spray volume mean diameter, mm
d_{32}	Spray Sauter mean diameter (SMD), mm
d_{lig}	Ligament diameter, mm
$\overline{d}$	Droplet mean diameter, mm
d_{v50}	Volume median diameter, mm
D_{inlet}	Inlet diameter for sprinkler, mm
D_o	Orifice diameter, mm
D_{slot}	Deflector diameter for slot, mm
D_{def}	Deflector diameter, mm
f	Dimensionless wave amplitude, $ln(A/A_0)$

f_0 Critical Dimensionless wave amplitude at breakup location, $ln(A/A_0)d$

f_v Volume probability density function

f_{v0} Magnitude for Gaussian distribution

F_v Cumulative probability density function

g Gravity, ms^{-2}

h Measurement elevation, m

K K-factor of sprinkler, $Lmin^{-1}bar^{-1/2}$

L_{arm} Length of sprinkler arm, m

LDD Spray local delivered density, mm/min or L/m^2S

L_{inlet} Length of sprinkler head inlet, m

L_{jet} Length of jet, m

M Spray momentum parameter

Mg Critical Spray momentum parameter

n Wave number, m^{-1}

n_{crit} Critical wave number, m^{-1}

n_t Number of tine

n_s Number of slot

P Pressure, bar or Pa

Pe Penetration ratio

P_n Legendre polynomials

q' Linear volume density

q'' Measured volume flux, kg/sm^2

q''_{ave} Average volume flux, kg/sm^2

q^* Volume flux ratio, q''/q''_{ave}

Q Volumetric flow rate, lpm

Q_i Estimated drop-wise volume flux, lpm

QF_i Estimated flux-based drop-wise volume flux fraction

Q_T Volumetric flow rate from tine stream, lpm

Q_S Volumetric flow rate from slot stream, lpm

Q_r Radiative heat flux, W/m^2

r Radius, m

r^* Dimensionless radius, r/R_{max}

r_d Deflector radius, m

r_d^* Dimensionless deflector diameter, r_d / D_0

r_{bu}^* Dimensionless sheet breakup distance, r_{bu} / D_0

r_{bu}, Sheet breakup distance, mm

R Maximum spray distance, m

Re Reynolds Number

RTI Sprinkler response time index

t Time, s

T Sheet thickness, mm

T_d Sheet thickness at the edge of deflector, mm

T_d^* Dimensionless sheet thickness at the edge of deflector, T_d / D_0

T_{plume} Plume temperature, K

T_e Sprinkler link temperature, K

T_{arm} Thickness of sprinkler arms

U Sheet velocity, m/s

U_{jet} Jet velocity, m/s

u_d Drop velocity, m/s

u_{air} Air velocity, m/s

$(v_o)_r$ Initial radial sheet velocity, m/s

$(v_o)_z$ Initial vertical sheet velocity, m/s

We Jet Weber number, $\rho_l U_{jet}^{\ 2} D_o / \sigma$

We_T Sheet Weber number, $\rho_l U^{\ 2} T / \sigma$

Greek letters

α Angle between the median streamline and axial direction z

β Sheet thickening factor

γ Rosin-Rammler / log-normal correlation coefficient

γ_t Flow split factor for tine

γ_s Flow split factor for slot

δ Boundary-layer thickness, m

θ Angle in elevation direction

θ_{boss} Angle for the boss in center of sprinkler deflector

θ_{ini} Initial sheet trajectory angle

θ_{tine} Angle for tine

θ_{slot} Angle for slot

λ Wavelength

μ Dynamic viscosity, kg/ms

ξ Position in curvilinear body-fitted coordinate

ρ_{air} Air density, kg/m^3

ρ_l Water density, kg/m^3

ρ^* Density ratio, ρ_{air} / ρ_l

σ Surface tension, N/m

ψ Angle in azimuthal direction

Chapter 1: Introduction

Sprinklers have been proven to be an effective fire suppression device through more than one hundred years of use. Compared to other fire suppression systems, sprinklers are cheap, reliable, or easy to install, maintain and operate. Although sprinklers have been widely used, the mechanisms for spray formation have not been fully understood. Several studies have been conducted focusing on optimizing the drop size and mass flux distribution for optimal suppression performance. Other studies have focused on characterizing fire sprinklers by measuring these distributions. Despite these efforts, physical models for predicting the initial spray from sprinklers have yet to be developed. This study involves a comprehensive study of understanding the initial sprinkler spray. This chapter introduces the objective and accomplishments of this study, followed by a description of the thesis organization.

1.1 Objectives and Accomplishments

The objectives of the current study are focused on characterizing sprinkler sprays through 1) performing detailed sprinkler spray measurements; 2) representing these measurements in a format easily integrated into CFD codes; 3) understanding basic spray formation physics through visualization of the spray topology; and 4) establishing scaling laws.

Major accomplishments for this study include

1. applying advanced diagnostics and sophisticated spray post-processing analysis to provide high fidelity initial spray characteristics for fire sprinklers;

2. establishing a mathematical framework to describe and generate the initial spray, which can be used as input for CFD simulation of sprinkler sprays;
3. revealing that the spray formation topology responsible for sprinkler sprays results from two orthogonal streams generated by flow along the sprinkler tines and flow formed through the sprinkler slots. This basic understanding guided measurement, modeling, and sprinkler characterization approaches in general;
4. developing scaling laws for sheet breakup locations and drop sizes in the high Weber number regime relevant to fire sprinklers.

1.2 Thesis Organization

This thesis is presented in a format of a collection of five relevant research papers, which were published or submitted for publication during the current PhD study. Each paper focused on a different stage of the sprinkler research, which provides the main body of this thesis with each paper presented as an individual chapter. A brief introduction of each paper will be presented in the next section. The last chapter provides a summary and conclusions. One appendix is provided to describe the detailed experiment approach followed by the imaging post processing approach and data post processing methodology for sprinkler spray measurements.

1.3 Paper Introduction

Three of the five papers had been published and two of them will be submitted shortly. The first paper is a review paper which is related to the current study. The second two papers focus on the experimental approaches and results. The fourth

paper focused on post processing and analysis. The last paper involves basic study of atomization physics. The layouts of those papers are adjusted to fit the UMD thesis format. The link of those papers will be provided in the final reference. The following provides a brief description for each paper.

1. "Sprinkler Sprays", will be submitted to *Fire Safety Journal*. This paper is a review paper, which provides a detailed review of sprinkler spray characteristics and performance. This paper will serves as a literature review of this study. However, this review paper is not limited to the objective of the current study. It also includes a brief review of sprinkler spray – fire interaction.
2. "Quantifying the Initial Spray from Fire Sprinklers" was published in the proceeding of *International Association of Fire Safety Science*, Germany, 2008. This paper included early measurements of liquid sheet breakup and drop size characteristics from fire sprinklers. A light-diffraction based measurement technique provided detailed local drop size distributions at various locations 1 m below the nozzle. The overall spray distribution was obtained through spatial integration of the combined local drop size distribution and local volume flux distribution.
3. "Atomization and Dispersion Measurements in Fire Sprinkler Sprays" was published in *Atomization and Sprays*, Vol.19, 2009. In this paper, laser based Shadowgraphy measurements of drop size are provided in the near-field of the spray for fire sprinklers and nozzles with more basic

geometries. Volume flux measurements 1 m below the nozzle are also presented.

4. "A Comprehensive Methodology for Characterizing Sprinkler Sprays" was published in the 33rd proceeding of *Combustion Institute*, 2010. This paper provides a comprehensive methodology for characterizing and describing the initial spray. Spatial profiles of initial spray quantities and a mathematical formulation to compress the initial spray data were presented in this paper. A spray dispersion model accounting only for droplet drag and gravitational acceleration provided good volume flux agreement with measurements one meter below the sprinkler.
5. "Characterizing the Initial Spray from Large Weber Number Impinging Jets", will be submitted to *International Journal of Multiphase Flow*. This paper focuses on spray formation physics. A basic spray relevant to sprinklers was formed by impacting a round jet onto a flat deflector. The effect of several parameters, such as nozzle orifice diameter, deflector diameter, injection pressure, and jet length, on the drop size and break-up location were investigated. Scaling laws for break-up location and drop size were developed and extended to sprinkler applications.

Chapter 2: Sprinkler Sprays

Ning Ren, André W. Marshall*

Department of Fire Protection Engineering

University of Maryland, College Park, MD, USA

2.1 Abstract

Sprinklers have been successfully used in fire suppression applications. Different sprinklers have been developed and installed in a variety of fire scenarios. Numerous studies have focused on evaluating the performance of sprinklers and predicting the spray interaction with fire. Both experimental and CFD modeling of spray fire interaction require the detailed initial spray characteristics. In this paper, detailed initial spray studies were reviewed with special attention given to the initial spray characteristics. In particular, the use of spray initiation models for the input to CFD simulations was discussed.

2.2 Introduction

Compared to other fire suppression agents, water is unbeatable. Many advantages make water a natural fire suppression agent. First of all, water is abundant, cheap and easy to excess. In contrast to other suppression agents like CO_2 and Halon 1301, water is humane and environmental friendly. The large specific heat and latent evaporation energy make water very effective in cooling the fire plume and pre-wetting the combustible materials. Although there are some limitations for special fire scenarios where water cannot be used as the suppressant, using water is still the most effective way to suppress fire. The basic mechanisms for water suppression are

wetting, cooling, oxygen depletion and radiation attenuation. The three water-based suppression systems are sprinkler system, water mist system and water hose systems.

The sprinkler system has been in use for over a hundred years. The first sprinkler was an upright sprinkler aimed at delivering the spray to the ceiling to prevent fire spread upstairs. The design of the sprinkler did not change until 1950, when people had a better understanding of sprinkler performance. The purpose of the sprinkler was expanded not only to prevent fire spread, but also control and suppress the fire. Since then, all kinds of sprinklers have been designed for a wide range of fire scenarios.

Water mist systems have become popular in recent decades. The aim of water mist systems differs from the objectives of than sprinklers. The major suppression mechanism of sprinklers is wetting the combustion material and pre-wetting the combustible material to prevent fire growth. However, one of the major purposes of water mist is to cool the fire plume. The tiny droplets that have a large surface to volume ratio evaporate very fast and absorb a large amount of heat reducing the plume and flame temperature. Meanwhile, a large amount of vapor is also generated, reducing the oxygen concentration, especially in a confined compartment. Without enough oxygen, the fire would be easier to control. Also, the water mist system requires a low flow rate, which means the water damage will be smaller than in sprinkler systems. The disadvantages of the water mist system are the high injection pressure it requires and the high cost relative to the sprinkler system.

The water hose system is mostly used by fire fighters to extinguish fires because a large amount of water can be delivered to a target point, which is very effective in extinguishing fires. Nowadays, new technologies for water hose systems are being

developed. One new system is called water cannon that can automatically search for the location of a fire. The computer can automatically calculate and control the injection pressure needed to deliver the water to the fire. This system is more effective than sprinklers and water mist when the fire is in an early stage and is easier to control. These systems are still under development and their performance still needs to be evaluated.

The focus of the current paper is the sprinkler spray system. Much attention is given to initial sprinkler spray studies. An attempt is made to discuss the spray initiation method. Spray interactions with fire are briefly discussed to address the importance of initial spray characteristics to the spray fire interaction study.

2.3 Sprinkler Geometry and General Spray Description

The numerous sprinklers available on the market can be categorized by several ways. For example, based on the design and performance, NFPA 13[1] defined 14 sprinkler types, such as the Early Suppression Fast Response Sprinkler (ESFR), Large Drop Sprinkler, Residential Sprinkler, Standard Spray Sprinkler, etc. When categorized by the installation orientation, sprinklers can be divided into 6 groups, such as the pendent sprinkler, upright sprinkler, sidewall sprinkler, etc. According to the sprinkler activation method, sprinklers can be divided into two major classes: Fusible sprinklers made by a low melting point metal alloy and Bulb sprinklers which are supported by a small bulb, usually made of glass. The performance of sprinklers has to be evaluated based on several criteria, such as the activation temperature, reliability, spray pattern, drop size distribution, etc. Once the sprinkler is successfully

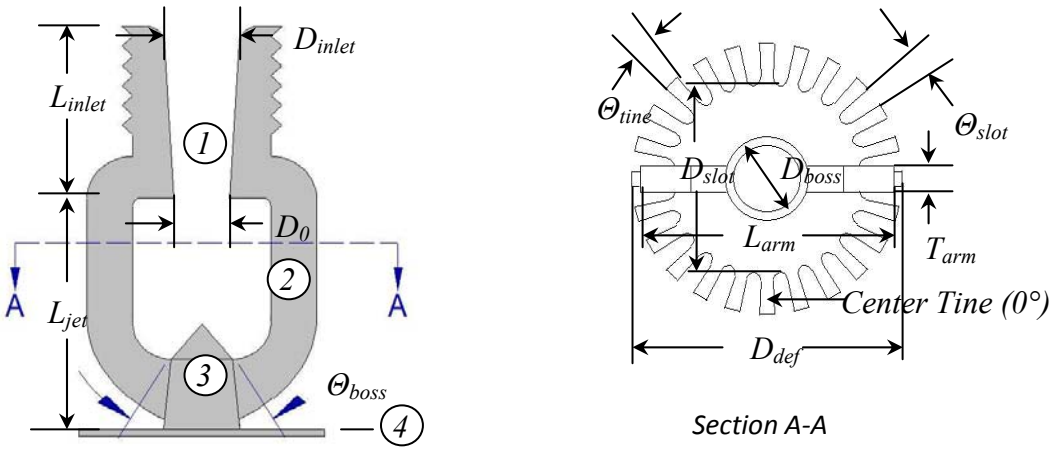

Figure 2.1 Anatomy of sprinkler head

activated, the performance will be determined by the spray drop size distribution and spray pattern, which is the focus of this study.

The spray distribution is very sensitive to the sprinkler geometry. While some sprinklers have similar geometries, their spray distributions may differ greatly. Generally, the most important geometric parameters are the nozzle orifice size and sprinkler deflector. The spray pattern is very sensitive to the deflector geometry with minor changes in deflector design making major differences in spray discharge characteristics. Figure 2.1 shows a detailed geometry of a sprinkler. Among those parameters, D_0 determines the sprinkler K-factor and overall characteristic drop size. The spray pattern is usually determined by the deflector geometry. For example, θ_{tine} and θ_{slot} are the angles of the tine and slot, which are geometrically related to how much water goes both outwards and downwards. They have major effects on spray pattern and minor effects on drop size and velocity. Some sprinkler deflectors may have little notches and holes. Those minor structures help the sprinkler to distribute the water more evenly and can be helpful for passing the standard spray volume

delivered density test. However, those structures make the spray formation process more complicated, making the drop size distribution harder to predict.

The drop size distribution can be characterized based on the number of droplets or the volume occupied by those droplets. In spray measurements, usually number based distributions will be measured directly and converted to volume based distributions, which are more commonly used in spray analysis. In the following discussion, the drop size distribution will be referred to as the drop volume based distribution. Although it has not been proven, the drop size distribution usually follows some well formatted functions, such as the Nukiyama-Tanasawa function, Rosin-Rammler function or Log-Normal function, etc. Related to the distribution function, there are several characteristic drop sizes used to represent the spray, such as d_{10}, d_{30}, d_{32}, d_{v50}, etc. Assuming the drop size distribution is a continuous function given by $f(D)$, these characteristic drop sizes are defined as

$$d_{10} = \frac{\int f(D)/D^2 dD}{\int f(D)/D^3 dD}, \tag{2-1}$$

$$d_{30} = \left(\frac{\int f(D) dD}{\int f(D)/D^3 dD} \right)^{1/3}, \tag{2-2}$$

$$d_{32} = \frac{\int f(D) dD}{\int f(D)/D dD}. \tag{2-3}$$

d_{v50} is the volume median diameter, meaning the drop sizes below d_{v50} take 50% of the total spray volume. Similar to d_{v50}, d_{v10} and d_{v90} are used occasionally. SMD represent the total drop volume to surface area ratio, which related to droplet heat transfer and evaporation. SMD is normally used in water mist characterization, where

cooling is the primary suppression mechanism. For sprinkler sprays, d_{v50} is more widely used as a characteristic drop size, while a combined Log-Normal and Rosin-Rammler function is used for spray distribution recommended by Yu [2]. The combined Log-Normal and Rosin-Rammler function are given as a Cumulative Volume Fraction (CVF) which is defined as

$$CVF(d) = \int_0^d f(D)dD = \begin{cases} \frac{1}{\sqrt{2\pi}} \int_0^d \frac{1}{\sigma D} e^{\left(-\frac{[\ln(D/d_{v50})]^2}{2\sigma^2}\right)} dD & (D < d_{v50}) \\ 1 - e^{(-0.693(D/d_{v50})^{\gamma})} & (D > d_{v50}) \end{cases} . \quad (2\text{-}4)$$

To make a smooth connection between the Log-Normal and the Rosin-Rammler parts, the parameter σ in a log-normal formulation should be correlated with γ by

$$\sigma = 2/\left(\sqrt{2\pi}(\ln 2)\gamma\right) \approx 1.15/\gamma , \quad (2\text{-}5)$$

However, some researchers found that the combined Log-Normal and Rosin-Rammler distribution cannot be applied for all sprinkler sprays. Sheppard [3] found that the combined distribution describes the spray for only a portion of the measurements. The rest of the data did not conform to Log-Normal, Rosin-Rammler or combined distribution. In general, most of the data can be described by the Log-Normal distribution below d_{v50} and part of the data can be described by the Rosin-Rammler above d_{v50}. Although not perfect, the combined Log-Normal and Rosin-Rammler distribution is the best function for sprinkler spray available.

2.4 Spray Study

2.4.1 Standard Tests

NFPA 13 provides the requirements for sprinkler usage and installation of sprinkler systems. The requirements for a single sprinkler is covered by UL199 [4],

which mandates a sprinkler undergo a series of standard sprinkler tests. These standards include chemical tests (corrosion test, thermal shock test, etc.), mechanical tests (physical strength, operating test, etc.), water distribution tests and fire tests. Among the tests, the water distribution test is the focus of this study. Figure 2.2 shows sample flow contours from a pendent sprinkler. However, the standard test does not require such detailed flow contours. The water distribution standard tests include a 10 pan test and a 16 pan test. For the 10 pan test, the spray distribution pattern shall not exceed a 16 foot (4.88 m) diameter circular area located in a horizontal plan 4 foot (1.22 m) below the sprinkler deflector. The size of each pan is one square foot. Several of these pans are placed in a row with the first pan right below the sprinkler deflector. The pans are mounted on a movable wheel, which rotates at 1 revolution per minute. The measurements are at a rate of 15 gallons per minute (0.95 L/S) for 1.4, 1.9, 2.8, 4.2 and 5.6 nominal K-factor sprinklers and last a minimum of 10 minutes or until a pan is filled with water. The volume distribution is actually an average distribution in the azimuthal direction. In the 16 pan test, 4 sprinklers are arranged in the shape of 10 foot (3.0 m) square with 16 pans in the middle of the four sprinklers. Volume density distribution is usually expressed in unit of Gal/ft^2s or L/m^2s or mm/min. A minimum average volume flux and minimum individual pan volume are criteria for passing the test based on the sprinkler K-factor.

Standard spray pattern tests are performed in a quiescent, cool environment. The local volume flux can be referred as Local Delivered Density (LDD). Volume density in fires is referred to as the Actual Delivered Density (ADD). One example is the ADD test for Early Suppression Fast Response (ESFR) Sprinklers. UL 1767 [5]

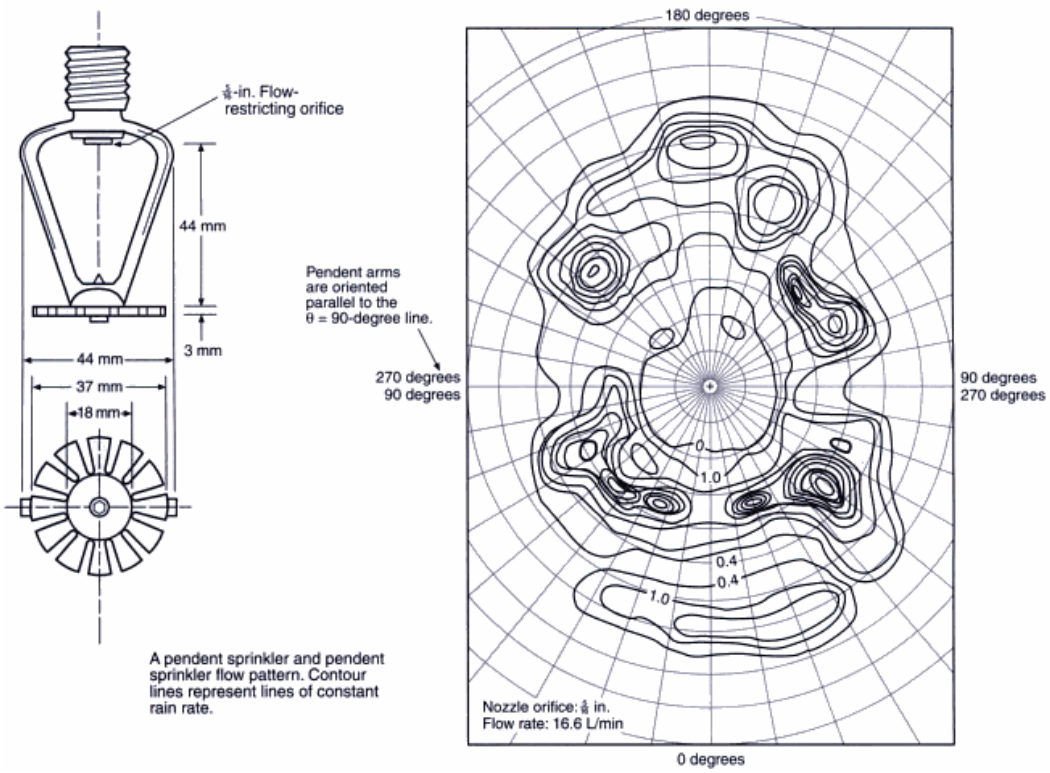

Figure 2.2 Pendent spray sprinkler and flow contour, NFPA [6]

provide the ADD Standard for Safety of ESFR Sprinklers. The test apparatus consists of 20 half-meter-square water collection pans. Sixteen of the water collectors are positioned approximately 90 inches above the floor in four groups of four. A six inch longitudinal and transverse flue space separates each group. Four additional water collectors are positioned below the upper array of 16 collectors to gather the water passing through the flue spaces. Eight groups of three heptane nozzles are arranged below the upper array and above the flue space collectors. These nozzles are capable of generating a fire plume from 0.1 to 3.5 MW. The array simulates a rack storage configuration commonly found in warehouses. The equipment is used to characterize and evaluate the storage capability and ESFR sprinkler's ability to penetrate the fire plume in rack storage warehouses.

Standard tests provide a benchmark for evaluating the spray distribution pattern. However, they are not detailed enough to fully characterize the spray features. In addition to volume delivered density, a systematic study of the spray requires detailed knowledge of the distribution of drop size and drop velocity. Limited by the instruments, early sprinkler spray characterizations were usually measured the far field local delivered density and local drop size distributions.

2.4.2 Analysis of Local Delivered Density

In addition to the standard tests, more volume density measurements have been conducted to get more detailed LDD. The standard tests are performed at a fixed pressure. However, for the same sprinkler, different pressures can change the spray pattern. Measurements show LDD changes in both radial and azimuthal directions. Similar to drop size distribution, LDD can also be expressed as a cumulative volume fraction, as given by Chen [7], who measured the LDD of ESFR and CPK sprinkler, 3.2 m below the deflector. Chen showed the cumulative volume fraction the of volume density distribution follows a Rosin-Rammler distribution. However, there is no data from other sprinklers to support the universality of Rosin-Rammler distribution for describing LDD.

LDD depends on the initial drop size, velocity and drop density. Spray dispersion in cool environment only involve drag effects, without considering droplet heat transfer and evaporation. Droplet are assumed to be spherical, while the droplet trajectory is determined by

$$\frac{d\overrightarrow{u_d}}{dt} = \vec{g} - \frac{3}{4}\frac{\rho_{air}}{\rho_d}\frac{C_d}{d}\left(\overrightarrow{u_d} - \overrightarrow{u_{air}}\right)\left|\overrightarrow{u_d} - \overrightarrow{u_{air}}\right| . \qquad (2\text{-}6)$$

C_d is the drag coefficient determined by [8]

$$C_d = \begin{cases} 24/\mathrm{Re} & \mathrm{Re} < 1 \\ 24(1+0.15\,\mathrm{Re}^{0.687})/\mathrm{Re} & 1000 > \mathrm{Re} > 1 \\ 0.44 & \mathrm{Re} > 1000 \end{cases} \quad \mathrm{Re} = \frac{\rho_{air} u_d d}{\mu_{ari}} . \tag{2-7}$$

The LDD can be non-dimensionalized to provide insight for spray dispersion eliminating the pressure effects. Prahl [9] and Nam [10] are such non-dimensional methods. In Prahl's method, the volume delivered density becomes to a linear density, where the delivered density is integrated along the azimuthal direction. Assuming the distance between the sprinkler and measurement plane is *h*, and then the maximum spray cover distance without drag effects is

$$R = U\sqrt{2h/g} . \tag{2-8}$$

Assuming the LDD is axisymmetric, the LDD, *q"*, is a function of radial location, *r*. The total flow rate is given by the integral

$$Q = \int_0^R \int_0^{2\pi} q'' r\,d\theta\,dr = \int_0^R 2\pi r q''\,dr = K\sqrt{P} . \tag{2-9}$$

Eq. (2-9) can be rearranged to give

$$\frac{Q}{\pi R^2} = \int_0^1 2\frac{r}{R} q''\,d\frac{r}{R} . \tag{2-10}$$

Using the dimensionless radius, $r^* = r/R$, and linear density $q' = 2r^* q''/\left(Q/\pi R^2\right)$, Eq. (2-10) becomes

$$\int_0^1 q'\,dr^* = 1 . \tag{2-11}$$

The linear volume density is already integrated in the azimuthal direction. Linear volume density shows the drag effects. For the same sprinkler, non-dimensional LDD will be similar at different pressures as showed in Figure 2.3. For the same nozzle, the

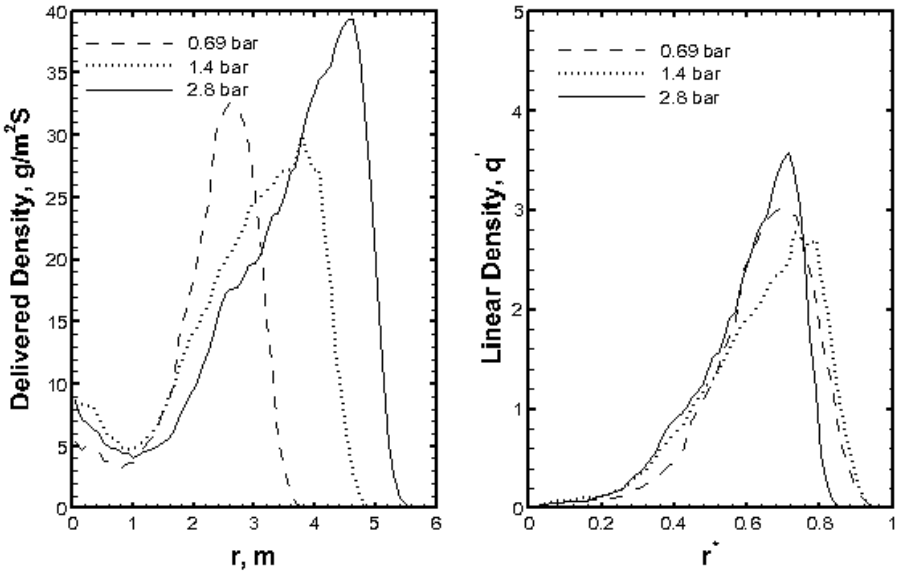

Figure 2.3 Local delivered density and corresponding linear density, created from impinging jet (D_{jet} = 9.7 mm) onto a round deflector (Blum [11])

linear density profiles at three injection pressures are similar. Due to the drag effect, in the linear density plot, the spray never reaches the non-dimensional location of 1.

Another non-dimensional method is provided by Nam [10]. A reference radius *R* was defined in such a way that half of the total water flow distributed in the area was less than *R*. The radius location is normalized by this *R*. An average volume density is defined as

$$q''_{ave} = \frac{Q/2}{\pi R^2}. \tag{2-12}$$

The dimensionless volume density is defined as

$$q^* = q''/q''_{ave}. \tag{2-13}$$

Nam's dimensionless volume flux showed the remarkable similarity between different ESFR sprinklers at several pressures.

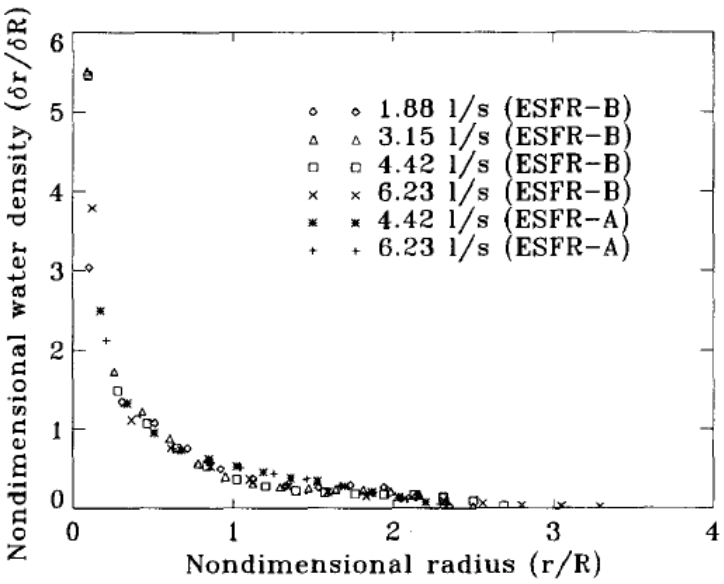

Figure 2.4 Dimensionless volume density for ESFR sprinklers (Nam [10])

2.4.3 Drop Size and Drop Velocity Characterization

Since the 1970's, efforts have been devoted to measuring the drop size distribution. Several particle sizing techniques have been explored. These techniques include the drop frizzing method (Yao and Kalelka [12]), particle shadow based method (Dundas [13], Yu [2], Chen [7], Walmsley and Yule [14], Do [15], Ren [16]), light diffraction method (Blum [11]), light scattering method (Gandhi and Steppan [17], Sheppard [3], Widmann [18, 19]) and PIV/PTV method (Putorti [20]).

Yao and Kalelkar's work was one of the earliest measurements in spray characterization. They measured the drop size distribution by freezing the falling drops in liquid nitrogen and then measured the frozen drops by means of a series of sieves. A 'Reliable' upright sprinkler with orifice diameter of 12.7 mm was tested under various pressures. They found that the drop size distribution is very close to a log-normal distribution, with most of the drop size between 0.5 mm and 2 mm. d_{30}

was used as a characteristic drop size, but no correlation was provided between the drop size and pressure.

Shadow based techniques were very popular in the history of spray research. First, a high speed photograph technique was used by Dundas. A high-speed electronic flash (~1μs) was used to "freeze" the droplets. The drop size was measured manually and in some instances by an electronic scanner. In Dundas's measurement, each measurement had about 500 – 2000 valid droplets to provide a drop size distribution. Walmsley and Yule measure two commercial sprinklers using a Kodak ES1.0 camera combined with a Pulse Photonics argon double spark flash unit, which is capable of obtaining two images in rapid succession, thus measuring both drop size and velocity. Compared to flash light, laser is much more suitable for high speed flash, thus "freezing" the droplet with more accuracy. One of the laser based high-speed drop sizing and counting systems was provided by PMS Inc., which was modified to measure sprinkler sprays by Yu, Chan. The instrument is a laser-illuminated optical array imaging device originally designed to measure the particle size of clouds and precipitation. The sampling area is about 61 mm × 6.4 mm. When droplets pass through the laser beam, successive image slices are recorded, providing both drop size and drop velocity information. Recently, Do and Ren used a laser based shadowgraphy system which shares the basic equipment with a PIV system but has an optical diffuser to provide a large area background instead of a laser sheet. The drop size and velocity can be measured simultaneously with high accuracy.

Another laser based drop size measuring system is provided by Malvern Inc. based on the principle of Fraunhofer diffraction. Blum conducted spray

measurements produced by flat disk and Tyco D3 nozzles. Malvern Instrument provided very accurate drop size measurement for small diameter sprays. However, when the spray d_{v50} is larger than 0.85 mm, the measurement will be not accurate. For large K-factor sprinklers operating at low pressure, Malvern Instrument may not be suitable for spray measurement. Another drawback of Malvern Instrument is the lack of ability to measure the drop velocity. Drop velocity is essential for measuring a flux-based drop size. Without knowing the drop velocity the characteristic drop size is spatial-based measurement and is biased towards droplets with lower velocities. More detailed discussion about flux based drop size can be found in Wu et al. [21].

Phase Doppler Interferometry (PDI) is also a popular technique in spray measurement. PDI provides both drop size and velocity measurement based on the light scattering and Doppler phase shift. Widmann and Sheppard used PDI for measuring residential sprinklers. The disadvantage of the PDI measurement is the small sample volume. In the far field of the spray where the spray is very sparse, the droplet sample number is not very large.

In contrast to the small sample volume of PDI measurements, Particle Image Velocimetry (PIV) measurements can provide a large sample field. PIV has been successfully used in measuring the velocity field, but it is not capable of measuring particle size. Putorti, however, extended the PIV system for measuring drop size. He developed a Particle Tracking Velocimetry and Imaging (PTVI) technique using laser induced fluorescence to visualize particle for measuring the drop size and velocity simultaneously. It should be noted that there are a few disadvantages to use laser sheet diagnostics to characterize the drop size. Errors can be introduced by film

resolution, camera diffraction error, optical component distortion, beam sheet thickness, camera depth of focus effects, etc. For example, the laser sheet thickness should be larger than the largest possible drop size in order to illuminate the droplet completely. There is a possibility that the laser sheet only illuminate half or a portion of the droplet. The larger the drop size, the higher chance to be 'cut' by the laser sheet. Also, the light intensity profile across the laser sheet will affect the drop detection. In order to overcome these disadvantages, Putorti developed a systematic testing procedure. Depth of Focus (DOF) is appropriately chosen based on drop sizes and laser sheet thickness. Dual-fluorescence method was developed to reduce the scatted signal effects. The laser sheet thickness is as big as 13mm, which is almost 3 times bigger than the largest drop size in typical sprinkler spray. The sprinkler tested by Putorti was not a commercial sprinkler, but specially manufactured to produce a symmetrical umbrella shape spray. More details regarding PTVI technique can be found in Putorti [20].

Expect for the different measurement techniques used for characterizing the drop size, the measurement locations are also different. Generally, the measurement location can be categorized as far field measurements (Yao and Kalelka, Dundus, Yu, Chen, Widmann, Blum) and near field measurements (Walmsley and Yule, Sheppard, Putorti, Do, Ren). Early spray drop size measurements were usually conducted in far field of the spray. Yu measured the drop size of three upright sprinklers with orifice diameter of 16.3, 13.5 and 12.7 mm at elevations of 3.05 m and 6.1 m below the sprinkler respectively. Measurements at these two elevations were almost the same, suggesting that effects of drop breakup and coalescence are negligible below 3.05m

and these downstream measurements can be used for spray characterization. Pitch [22] performed some research on droplet secondary breakup. He found if the drop Weber number defined as $We = \rho_{air} U^2 d / \sigma$ is larger than 12, the droplet is not stable and will breakup into several smaller droplets. Yao and Kalelkar found that the largest stable water drop, which does not breakup easily, is about 6 mm in diameter with a terminal velocity of 10 m/s. The corresponding Weber number for this droplet is about 9, and according to Pilch's theory of secondary breakup, it will be stable. For sprinkler applications, the characteristic drop sizes usually on the order of 1 mm. Thus, for the drop size characteristics, the far field measurement can be performed instead of near field measurement as a representative drop size for that sprinkler.

The near field spray characterization is more challenging due to high drop density and large flow momentum. In Walmsley and Yule's measurement, a very thin slice of the spray was removed from the overall spray measurement, by applying two knife edge barriers in front of the camera and flash light. The gap between the two barriers was 35 mm. Sprinklers was set 217 mm away from the camera. Measurement locations were changed by rotating the sprinkler head. Nine measurement positions were used, corresponding to either a tine or a slot. Two pressures were investigated for each sprinkler. A similar experimental setup was adopted by Do [15], Ren [16] in measuring several nozzles and fire sprinklers.

Although the measurement techniques and experimental setup are different, the dimensionless drop size is following a similar trend proposed by Heskestad [23]. The dimensionless sprinkler characteristic drop size, d_{v50}/ D_0, can be scaled with jet Weber number, which is given by

$$d_{v50} / D_0 = CWe^{-1/3} \quad (2\text{-}14)$$

Dundas summarized the drop size from previous researchers with sprays produced by nozzles other than sprinklers [24-26]. The author found that the coefficient, C, is in the range $1.74 < C < 3.21$. Dundas found the coefficient C in his application is 1.41, which is smaller than the reported value in previous investigations. Dundas compared the drop size distribution with a Rosin-Rammler distribution and found they are very close and accurately represent the experimental data. In Yu's measurements, the coefficient, C, is between 2.33 and 4.48, which changes depending on the sprinkler type. The drop sizes provided by Walmsley and Yule are slightly different, namely

$$d_{v50} / D_0 = 7.05 \cdot We^{-0.3682} \quad (2\text{-}15)$$

The coefficient, C, is much larger than others. Widmann reported mean volume diameter, d_{30}, instead of d_{v50}, which also follows $We^{-1/3}$, except at low pressures (below 0.69 bar).

However, not all the spray measurements show that the dimensionless d_{v50} follows a (-1/3) Weber number power law decay. Putorti found that in some Weber number regions, the drop size decreases faster to follow a (-2/3) power law. On the other hand, Blum found that sprays were produced by a flat disk have drop size decay following approximately a (-1/6) Weber number power law. Tyco D3 nozzle sprays behave the same as sprinklers described by Eq. (2-14). The reason of those different drop size behaviors may be related to different sheet breakup modes, which have not been fully understood and are still under research.

One important parameter that should be pointed out in spray characterization is the drop sample number. For the sprinkler spray distribution, the largest drop size can be larger than 3 mm, and the smallest drop size can be in the order of 0.1mm. The volume ratio of the largest droplet to the smallest droplet is in the order of $10^3 – 10^4$. In order to have a reliable drop size distribution, the sampling number should be large enough to capture the few large droplets. Grant [27] provided a correlation between the error and sample size. For a sample size of 500, the error can be as high as 17%. The error goes down quickly as the sample size increases. When the sample size is 5000, the error reduces to about 5%. As the sample size increases over 5000, the error reduces slowly with the sample size. As limited by the experimental equipment, Dundas's sample number is not very large, and it can be estimated that the error of Dundas's drop size measurement will be around 7% - 10%. As Dundas pointed out, the major cause of the scatter of the drop size is thought to be attributable to an insufficient drop sample. The same problem arises in Widmann's measurement. Due to the small size of the PDI sample volume and low spray density in the measuring plane, the sample number is below 2000 at each measuring location. For the near field spray measurement, the sample size can be increased easily because of the high drop density. In Sheppard's measurements, the average drop sample number is 10286 to provide a smooth drop size distribution. The drop sample number is even higher in Do and Ren's measurements with a larger sample area and high initial spray density. The sample number is between 10^5 and 10^6 depending on the pressure and sprinkler K-factor. Large sampling number reduces the statistical error and provides a smooth distribution curve.

The velocity of the spray was reported by several researchers. Unlike the drop size, the drop velocity changes with measurement location. Widmann measured drop velocity in a horizontal plane 1.12 m below the sprinkler and found most of the droplets have velocities higher than the corresponding terminal velocity, indicating most drops left the sprinkler with greater momentum and have not yet decelerated to the terminal velocity at the measurement plane. In Chen's measurement, the drop velocity was recorded approximately 3 m below the sprinkler. He found that at this elevation, the measured drop velocity is close to the terminal velocity for different pressures. The droplet terminal velocity is sensitive to the diameter. Both Grant and Sheppard provide detailed discussion about the relationship between drop diameter and terminal velocity. In order to penetrate the plume, the drop size has to be big enough to have a terminal velocity higher than the plume velocity or the droplet initial momentum has to be large enough to penetrate the plume to wet the combustion surface before it slows down significantly. A more detailed discussion will be presented in the following section.

When referring to the spray velocity, one means the initial drop velocity, at the location where the droplet is initially formed. Sheppard measured the initial spray velocity for a variety of commercial fire sprinklers in the near field about 0.38 m from the sprinkler head. He got detailed velocity fields and found the velocity profiles change with elevation angle but are not sensitive to the azimuthal angle. The average velocity can be approximated by

$$u_{avg} \approx 0.6\sqrt{P/\rho} \quad . \tag{2-16}$$

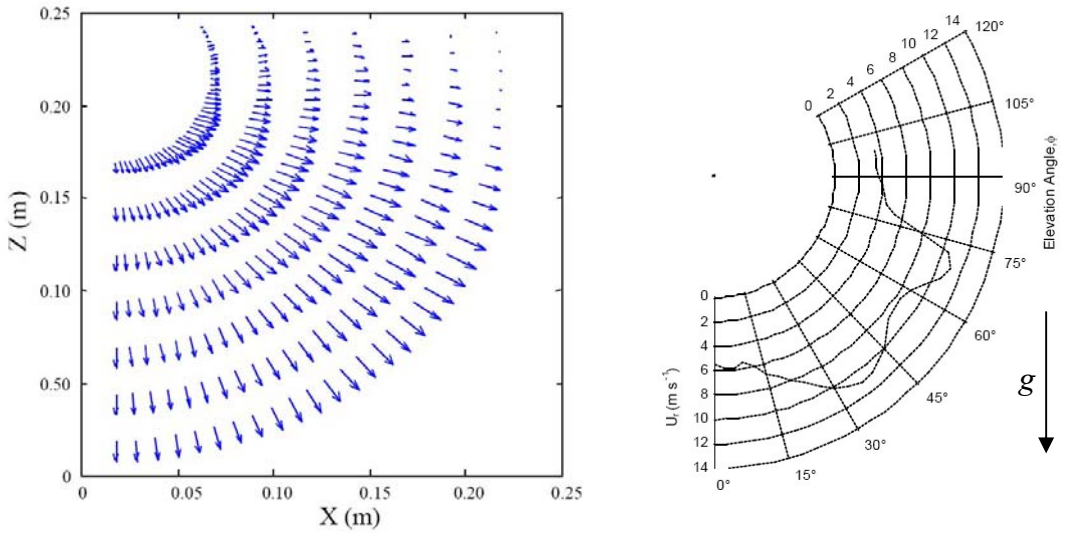

(a) (b)

Figure 2.5 Near field spray velocity, P=1.31 bar; (a) velocity vector; (b) average velocity in elevation direction

It should be noted that the effect of sprinkler arms has not been fully studied. As shown in Figure 2.2, the LDD reflects the effect of sprinkler arms. NFPA 13 requires the sprinkler arm to be aligned with the pipe direction. For upright sprinklers, not only the sprinkler arms, but also the pipe itself will change the flow pattern slightly. Chen's measurement shows that when considering the sprinkler arms, the LDD for the two ESFR sprinklers were roughly symmetrical. However, the initial drop size distribution around the sprinkler arm has yet to be reported.

2.4.4 Atomization Theory

To better understand the drop size behavior of Eq. (2-14), the atomization physics are reviewed in this section. Generally, the atomization mechanism related to sprinkler sprays can be categorized as a sheet instability mechanism. An illustration of the atomization process is shown in Figure 2.6. A jet is formed from the sprinkler orifice and it impinges on the deflector to form an expanding liquid sheet. The

unstable sheet will breakup into ligaments or droplets. The sheet structure for sprinkler sprays is more complicated. Blum, Do [15] studied the sheet structure created by a Tyco D3 nozzle similar to a sprinkler and found that the sheet has a three dimensional structure. Horizontal sheets are created along the tine stream, while vertical sheets are created along the slot stream. Figure 2.7 shows the slot sheet and tine sheet respectively. Although the sprinkler spray has a more complicated structure, the atomization physics still follow the illustration described by Figure 2.6. The key point to understand is that the drop formation is governed by sheet instability theory.

The sheet instability is usually the Kelvin-Helmholtz type instability, where there is sufficient velocity difference across the interface between two fluids. Early work of sheet instability study started from Squire [28], who investigated the instability of a moving two-dimensional sheet with constant sheet thickness. In his analysis, the

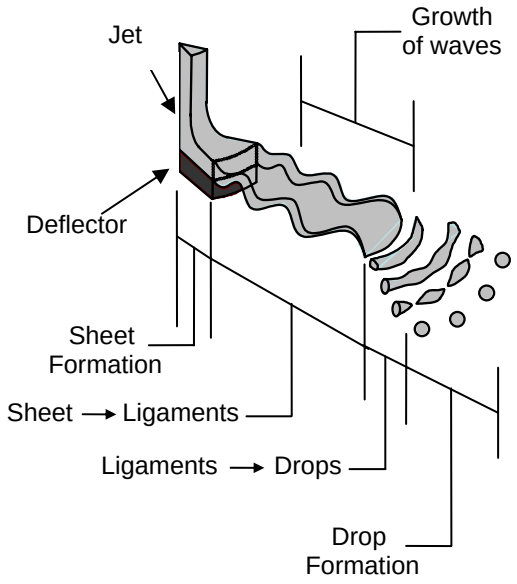

Figure 2.6 Description of atomization process [21]

gravity force is ignored. Considering the sheet atomization process is fast, gravity force is negligible. Squire used the classical methods given by Lamb [29]. The governing forces determining the sheet motion are surface tension and pressure forces. Squire assumed the disturbance is in the form of a sinusoidal wave, and found that if the sheet Weber Number ($\rho U^2 T / \sigma$) > 1, the sheet will be unstable. For the case of *We* >> 1, the unstable wavelength can be simplified as

$$\lambda \approx 4\pi\sigma / \rho_{air} U^2 . \qquad (2\text{-}17)$$

Squire compared the calculation with measurements provided by the National Gas Turbine Establishment. The atomization photography was taken under normal and reduced ambient pressure for different air density situations. Squire's calculation is in the same order as the measurements. Although Squire gave a good estimation of the unstable wavelength, his theory does not provide when and how the sheet will breakup.

Although Squire assumes the disturbance is in the form of a sinusoidal wave, there are two modes of disturbance, which are sinusoidal and dilatational disturbance. These two disturbance modes are also reffered to as antisymmetrical and

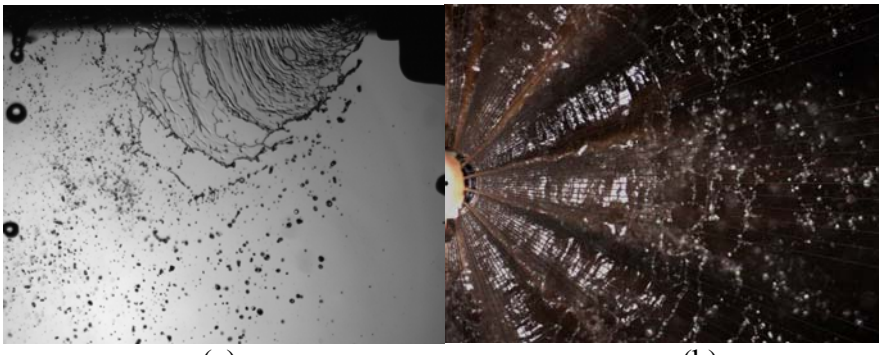

(a) (b)

Figure 2.7 Images for expanding sheet from Tyco D3 Nozzle; (a) Shadowgraphy side view images for sheet from slot flow; (b) Top view image for sheet from tine flow [15]

axisymmetrical disturbances, respectively. Which disturbance mode dominates the instability depends on the Weber Number. Hagerty and Shea [30] studied the sheet instability for both of these modes and compared the wave growth rate for both cases.

$$\frac{\partial f_{\sin usoidal} / \partial t}{\partial f_{dialtional} / \partial t} = \coth \frac{nT}{2} \quad \text{(2-18)}$$

When $nT/2 < 1.5$, $coth(nT/2) > 1$, so that the sinusoidal wave is always greater than the dilatational waves. For flapping thin sheets, the sheet thickness is in the order of 10^{-4} m, which is much smaller than the wavelength. Sinusoidal waves are usually observed for sheet instability, while dilatational waves are usually observed on jet instability. Figure 2.8 shows a side view image for a sheet produced from fan spray nozzle [31]. Smoke tracers were used to visualize the air movement on one side of the sheet. The Sinusoidal wave clearly shows when the sheet is expanding. Xianguo Li and R. S. Tankin [32] further studied these two modes and concluded that dilatational waves control the instability process for small Weber numbers while sinusoidal waves dominate for large Weber numbers. Sinusoidal waves dominate over a wide range of Weber numbers, which is the range of interest for most of the researchers focused on.

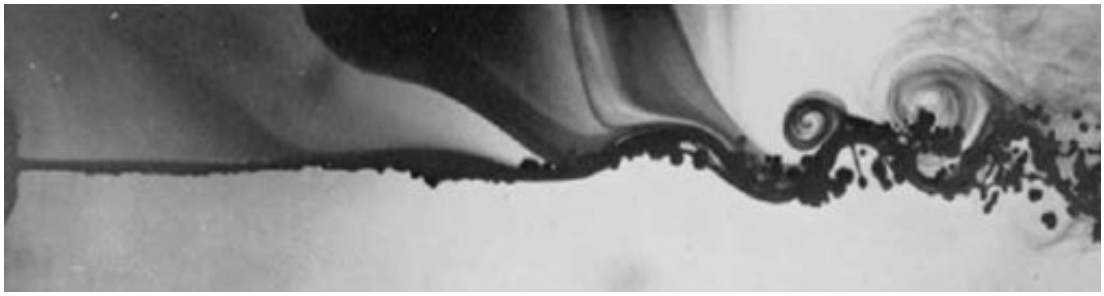

Figure 2.8 Shadowgraphy image for expanding sheet (Crapper [31])

Following Squire [28], Dombrowski [24, 26, 33, 34] and his co-workers studied the instability of fan spray nozzles, which produce a smooth expanding sheet. In the instability analysis, Dombrowski considered not only the surface tension force and pressure force, but also viscous force and inertial force inside the sheet. With the balance of these four forces, the instability of the sheet is simplified to one equation in terms of dimensionless wave amplitude.

$$\left(\frac{\partial f}{\partial t}\right)^2 + \frac{\mu n^2}{\rho_L}\left(\frac{\partial f}{\partial t}\right) + \frac{2\left(\sigma n^2 - \rho_{air} n U^2\right)}{\rho_L T} = 0 . \qquad (2\text{-}19)$$

where $f = ln(A/A_0)$, A_0 is the initial wave amplitude. Eq. (2-19) is a non-linear differential equation. The first term is related to the inertial force, the second term comes from viscous force, and the last term is determined by the pressure force and surface tension force. For the growing wave, the wavelength can be any possible number; however, only one wavelength will lead to maximum wave growth rate, which is the characteristic wavelength. From Eq. (2-19), the characteristic wave number is implicit due to the non-linear term. The viscosity of water is relatively small and the second term in Eq. (2-19) is orders of magnitude smaller than other terms. Eq. (2-19) can be linearized by neglecting the second term.

$$\left(\frac{\partial f}{\partial t}\right) = \left(\frac{2\left(-\sigma n^2 + \rho_{air} n U^2\right)}{\rho_L T}\right)^{1/2} . \qquad (2\text{-}20)$$

Maximizing the right hand side, the critical wave number can be determined by

$$n_{crit} = \frac{\rho_{air} U^2}{2\sigma} = \frac{2\pi}{\lambda_{crit}} . \qquad (2\text{-}21)$$

The critical wavelength is the same as Squire's. Dombrowski compared the viscous solution and inviscid solution. The viscous effect will dampen the dispersion and

reduce the wave growth rate, and the critical wavelength will be slightly larger than the inviscid wavelength solution. The wave growth increases with decreasing sheet thickness.

Dombrowski also provided a criterion to determine the sheet breakup condition. Weber studied the jet instability and found that the dimensionless ratio of amplitude to f_{crit} at breakup has a constant value of 12. Dombrowski extended this criterion to the sheet instability analysis independent of operating conditions. Although the critical amplitude ratio is arbitrary, the drop size predicted by the instability theory does not change significantly.

Dombrowski also provided a drop formation model, which is based on the critical wavelength. As the waves grow on the sheet until they reach the critical amplitude, the sheets will breakup into ligaments every one-half wavelength. Weber [35] has analyzed the property of jet flow with co-current air flow where jet-air interaction helps the disintegration. However, in this case, the ligaments move transversely in the air. Dombrowski neglected the air interaction and assumed the instability was only caused by the surface tension. A very simple correlation between droplet diameter and ligament diameter is given by

$$d \approx 1.88 d_{lig} , \tag{2-22}$$

Dombrowski compared the predicted drop size with the measured d_{32} provided by Hasson and Mizrahi [36]. The measured drop size lies satisfactorily around the straight line

$$d_{32} = 0.676 d . \tag{2-23}$$

Squire and Dombrowski's formulated stability equations based on two dimensional waves infinite in the third dimension; while Weihs [37] equations were based on axisymmetric two dimensional waves, properly accounting for thinning of the radially expanding sheet. These complex equations simplified to provide similar results as Dombrowski in the near field.

Sheet breakup under forced disturbance was studied by Prahl and Wendt [9]. They use a modified deflector to represent a sprinkler head. The deflector can vibrate in a sinusoidal motion acting as the forced disturbance. The vibration frequency and amplitude can be well controlled by a sinusoidal signal generator. The sheet breakup location and wave amplitude at the breakup location was recorded under various jet flow rates, deflector vibration frequencies and amplitudes. If the deflector vibration frequency is close to the resonance frequency of the sheet, the wave growth rate is enhanced and the sheet breakup will occur faster. The theoretical resonance frequency is obtained from their theoretical maximum wave growth wave number, which is

$$n_{crit} = \frac{\rho_a U^2}{2\sigma}\left(\frac{1}{2} - \frac{5}{We_T} + \left(\frac{1}{4} + \frac{7}{We_T} + \frac{1}{We_T^2}\right)^{1/2}\right). \qquad (2\text{-}24)$$

where We_T is the Weber number based on the sheet thickness at the edge of deflector. In sprinkler applications, the spray velocity is on the order of 10m/s, the sheet thickness at the edge of the deflector is on the order of 1 mm. We_T will be on the order of 1000 and the effect of We_T can be neglected. Thus, Eq. (2-24) is the same as Eq. (2-21). Prahl and Wendt's result shows that close to the natural wave frequency, the sheet breakup radius reduces by more than 20% and the wave amplitude at the breakup also reduces compared to the wave amplitude without forced disturbances.

Huang [38] studied the sheet breakup of axisymmetric liquid sheets formed by the impingement of two co-axial jets. Huang studied the sheet breakup motion for various sheet velocities. Three regimes are defined based on the jet Weber Number. The first regime, $100 < We < 500$, corresponds to a stable liquid sheet regime. In this regime, the sheet is flat and has a nearly perfect circular edge. Droplets are detached along the periphery. The sheet breakup distance increases as the jet Weber Number increases. The liquid sheet is assumed free from any external disturbances and at the breakup location, the inertia force exerted radially outwards on the edge of the circular sheet is balanced by the inward radial and circumferential surface force. Based on this assumption, Huang obtained the sheet breakup correlation for the first regime as

$$\frac{r_{bu}}{D_0/2} = 0.167We. \tag{2-25}$$

The second regime is a transition regime starts with $500 < We < 2000$. The sheet breakup distance first increases then decreases slowly with Weber Number. The expanding sheet is not smooth; sinusoidal waves are observed at the breakup location. As the jet Weber Number exceeds 2000, the sheet is more unstable. Huang determined the critical wavelength yielding maximum wave growth rate. His critical wavelength is consistent with Squire and Dombrowski's result. In this sheet flapping regime, the sheet breakup distance decreases as the jet Weber Number increases. Huang determined a semi-empirical formula for sheet breakup distance, which is

$$\frac{r_{bu}}{D_0/2} = 1250We^{-1/3}. \tag{2-26}$$

Huang's study clearly shows the axisymmetric sheet behavior. However, little is known for the corresponding drop size.

More recently, Villermaux and Clanet [39, 40] studied both the smooth liquid sheet and flapping liquid sheet. Both water and ethanol were used in the study. Sheet breakup distance and drop size were plotted. For the smooth sheet, the breakup distance increases linearly with Weber number and for the flapping sheet, the breakup distance decreases following $We^{-1/3}$ power law, which is consistent with Huang's result. Unfortunately, for the drop size, the author used an average drop size which is d_{10} in the plots instead of using the popular drop size of d_{v50}. The author found the mean drop diameter decreases with Weber number, first slowly following $We^{-1/3}$ for $We < 1200$ and more strongly for higher value of the Weber number following We^{-1}. Above a certain value that corresponds to the point where the liquid sheet becomes turbulent, the drop size seems to reach a limit.

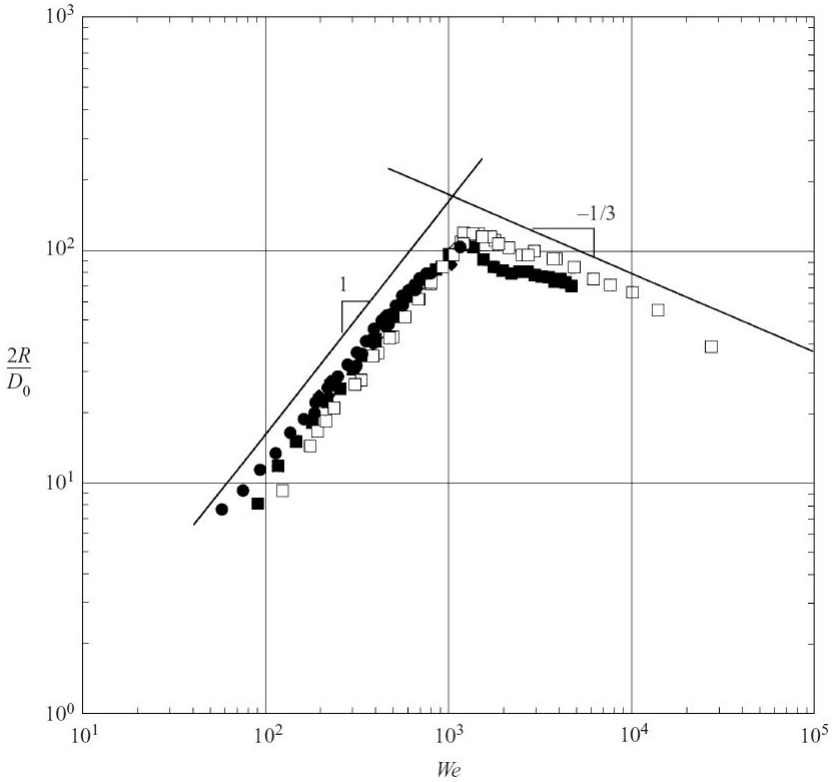

Figure 2.9 Sheet breakup distance, Villermaux and Clanet [39]

These two liquid sheet breakup regimes, were categorized as absolute and convective instability regime by S.P. Lin and W.Y. Jiang [41]. They analyzed the inviscid expanding liquid sheet and found that when the local Weber number based on the sheet thickness and velocity is 1, absolute instability occurs and convective instability occurs only when the local sheet Weber number is larger than 1. They compared their theory to Huang's measurements. They converted the jet Weber number to the local sheet Weber number at the breakup location. In the smooth sheet regime, the local sheet Weber number at breakup location is indeed 1, and in a flapping sheet regime, the local sheet Weber number is larger than 1 and increases with jet Weber number. They also calculated the theoretical wave amplitude at the breakup location. In the flapping sheet regime, when the jet Weber number is larger than 2000, the critical wave amplitude f_0 is about 12, which confirms Dombrowski's assumption. However, f_0 is not a constant, and increases slightly with jet Weber number. For jet Weber number of 16000, f_0 is about 17. Ren [42] also found that f_0 increases with jet Weber number in the study of a jet impinging on a large diameter deflector. Lin and Jiang explain that this may be due to the non-linear effect, when jet Weber number is too large, the wave amplitude at the breakup location is comparable to the wavelength (see Figure 2.7), and the analysis based on linear stability is not legitimate. Fortunately, in Dombrowski's atomization model, the drop size is not very sensitive to f_0, and a constant f_0 of 12 will provide a reasonable drop size prediction.

Sheet instability studies are only the first step of modeling spray atomization. Even if the sheet breakup location can be predicted precisely, there are still several uncertainties about drop size prediction. The first uncertainty is how the sheet breaks

up. Dombrowski assumed the sheet breaks up every half wavelength to form ligaments. However, sheet breakup images [15, 42, 43] show that the sheet breakup mode is much more complicated. There are several sheet breakup modes. The sheet may breakup into droplets directly, or into large fragments or ring like ligaments. The second uncertainty is how those fragments or ligaments breakup. So far, there are no accurate models to predict the ligament breakup.

Although there are several drawbacks, Dombrowski's model works well for a high pressure swirl nozzle. Corradini [44] adapted and modified Dombrowski's model for prediction of high-speed liquid sheet atomization. The prediction and measurements match well. Recently, Santangelo [45] measured the drop size distribution for high pressure swirl nozzle. In his application, a very thin liquid sheet is formed with sheet velocity in the order of 100 m/s. He found the drop sizes indeed decreases following $We^{-1/3}$ power law and match with Dombrowski's prediction well.

To predict the drop size, the initial sheet thickness and sheet velocity are required. For simple geometry spray (i.e. imaging jet onto a round deflector), the sheet thickness and velocity can be estimated using Watson's [46] boundary layer model. Di and Marshall [21] developed a first principle spray atomization model using Dombrowski's model and introducing stochastic spray behavior. Ren [42] modified Di's sprinkler model and put the deceleration of expanding liquid sheet effect. The methodology of expanding sheet deceleration is given by Ibrahim [47] using a curvilinear coordinate system. The surface tension and air friction forces are considered for the sheet trajectory. Calculation shows that the trajectory is close to a straight line at high sheet velocity and the air friction only has a minor effect of the

sheet deceleration and sheet thickening (less than 5%). But the sheet trajectory can be changed a lot at low pressure below 0.5 bar, which is the minimum sprinkler operation pressure. Based on Dombrowski's model, Ren extended the drop size scaling law to include more geometric effects, which is

$$\frac{d_{v50}}{D_0} = 4.5\left(\frac{\rho_{air}}{\rho_l}\right)^{-1/6}\left(\cos^{1/2}\theta_{ini}\frac{r_d^* T_d^* \beta^2}{f_0}\right)^{1/3} We^{-1/3} = CWe^{-1/3}. \qquad (2\text{-}27)$$

where θ_{ini} is the initial sheet trajectory angle, usually a few degrees lower than the horizontal line, r_d^* is the dimensionless deflector size, T_d^* is dimensionless sheet thickness, and β is a sheet thickening factor describing the sheet velocity deceleration along the deflector. The coefficient in traditional scaling law can be expanded as an expression related to sprinkler geometry as shown in Eq. (2-27).

As discussed in the previous section, the coefficient, *C*, varies for different sprinklers. This is because the initial sheet thickness and sheet velocity is sensitive to the sprinkler geometry. Unfortunately, no model has been developed to quantify the initial sheet status for sprinkler spray. Do [15] did a simple measurement to measure how much flow goes in tine stream and how much flow in slot stream. Based on the flow ratio between tine and slot flow, the sheet thickness can be estimated. The split factor for tines and spaces are defined by

$$\begin{cases} \gamma_t = \dfrac{Q_T / Q}{n_t \theta_{tine} / 2\pi} \\ \\ \gamma_s = \dfrac{Q_S / Q}{n_s \alpha / 2\pi} \end{cases}. \qquad (2\text{-}28)$$

where $n_{t,s}$ is the number of tine and slot, θ_{tine} is the angle of tine sheet, α is the angle of slot sheet and Q is the flow rate. And the characteristic drop size for tine stream and space stream can be scaled using the same format as

$$\frac{d_{v50,t,s}}{D_0} \sim \left(\frac{\rho_{air}}{\rho_l}\right)^{-1/6} \beta\gamma_{t,s} f_{0,t,s}{}^{-1/3} We^{-1/3}. \tag{2-29}$$

The subscript *t,s* means for tine stream and space stream respectively. Do's spray measurement shows the drop size along the slot stream is smaller than the drop size along the tine stream, which can be explained by Eq. (2-28, 2-29). For sprinkler spray, the stream angle for slot flow (~ π/2) is much larger than the tine flow (~ π/6, depending on the number of tine and slot). γ_s is usually smaller than γ_t, yielding a smaller drop size given by Eq. (2-29). In other words, the slot flow is distributed to a more wide area leading to a thinner sheet, thus the drop size will be smaller.

2.5 Spray Interaction with Fire

Generally, spray interaction with fire involves several sub-topics, such as spray penetration, droplet evaporation, spray cooling, wetting, oxygen depletion, radiation attenuation, spray induced flow, spray interaction with plume, flame and smoke layer, etc. Major spray suppression mechanisms include cooling, wetting, radiation attenuation and oxygen depletion. However, for a specified spray, the dominate mechanism depends on the spray characteristics. For example, the cooling effect is more important for water mist sprays. If the fire is in an enclosed compartment, the oxygen depletion will play an important role associated with cooling effect. However, for sprinklers, the cooling and oxygen depletion are not major suppression mechanisms. Big droplets have smaller resident time to make the droplet have

significant evaporation. Also, the surface to volume ratio is too small to support strong evaporation. The major suppression mechanism is wetting the burning surface and pre-wetting the unburned materials. Cooling the plume and flame is less important.

To successfully wet the burning surface, the spray has to penetrate the plume. The penetration ability of the spray is determined by the drop size and initial velocity. Droplet terminal velocity is very sensitive to the drop size. For example, a 1 mm diameter water droplet has a theoretical terminal velocity of 5.64 m/s. The plume velocity could be estimated by Yokoi's [48] theory. For a fire with heat release rate about 500 KW, the plume velocity 3 m above the fire is about 5.61 m/s, which is almost the same as the droplet terminal velocity. The 1 mm drop could barely penetrate the 500 KW plume to wet the burning surface. Yao [12] studied the effect of drop size on sprinkler performance. He measured the ADD of four half-inch standard sprinklers and compared with deliver density in the case without fire. The fire is provided by burning gasoline at a flow rate of 1.5 gpm. Tests were conducted by locating the collecton pans 5 ft. and 29 ft. below the sprinkler. Four pressures were performed on the sprinkler head to investigate the penetration with different drop sizes. Those tests show the penetration decreases with increasing pressure. Although higher pressure will provide higher initial drop velocity, the drop sizes decreases and the penetration decreases. Penetration also decreases when increasing the distance between the collection pans and the sprinkler. More research about spray penetration was reported by Yao [49] in a sprinkler overview paper. He found that the spray penetrates the fire plume in two modes: the gravity mode and the momentum mode.

In the gravity mode, the droplets penetrate the plume by gravity force and only large drops in the hot plume that have terminal velocities larger than the plume velocity can penetrate the plume. In the gravity mode, the penetration is proportional to the drop size. Based on the dimensional analysis, the penetration ratio (*Pe*) for sprinklers of similar geometry is expressed as:

$$Pe \propto d_{v50} \propto \frac{D^{2/3}}{P^{1/3}} \propto \frac{D^2}{\dot{Q}_w^{2/3}}. \tag{2-29}$$

In the momentum mode, the penetration ratio is a function of momentum parameter, *M,* which is the ratio of the downward momentum of the water spray and upward momentum of the fire plume. Under the momentum, the sprinkler spray creates a significant effect on the plume, and the drop size is no longer important. There is a critical momentum parameter, $Mg = 0.204$, below which gravity mode happens. The momentum ratio is determined by the sprinkler K-factor, injection pressure, sprinkler spacing, distance between sprinkler and fire source and convective heat release rate. Yao provided several methods for increase the momentum parameter, include: (1) use of fast response sprinklers to reduce convective heat release rate at the sprinkler operation, (2) increase sprinkler orifice size, (3) reducing sprinkler spacing, (4) reducing clearance. Those suggestions serve as the guidelines for sprinklers and sprinkler system designs.

Although cooling is not the major suppression mechanism for sprinkler spray, it may play an important role in sprinkler activation. The plume temperature will be reduced and the activation of adjacent sprinklers may be delayed. The activation of sprinkler is modeled based on the heat transfer between the fire plume and sprinkler link, which is called RTI model. The temperature of the sprinkler link is given by

$$\frac{dT_e}{dt} = \frac{\sqrt{U}(T_{plume} - T_e)}{RTI} + \frac{Q_r}{mc_p} - \frac{C(T_e - T_\infty)}{RTI}, \tag{2-30}$$

where T_{plume} is the plume temperature, U is plume velocity, Q_r is radiative flux, C is the conduction parameter and RTI is the sprinkler Response Time Index. Experiments on warehouse fires indicate that the RTI model [50] is not always adequate to predict the response of an array of fire sprinklers. The model works good to predict the activation for sprinkler close to the fire, but fails to predict the activation of surrounding sprinklers. Ruffino and diMarzo [51] conducted experiments to model the sprinkler response with adjacent sprinkler sprays. Small droplets less than 0.1 mm are only a tiny portion of the total spray. However, those small droplets will be carried by the plume and reduce the heat transfer rate to the sprinkler link. If the radiation terms are ignored, the sprinkler link temperature will be

$$\frac{dT_e}{dt} = \frac{\sqrt{U}(T_g - T_e)}{RTI} - \frac{EU\beta\sqrt{d_l}}{RTI}, \tag{2-31}$$

where E is evaporative cooling parameter, is water volume fraction and is simulated sprinkler link diameter. The evaporative cooling parameter is given by

$$E = \frac{\rho_L A \kappa \Lambda}{S} \frac{\sqrt{u/d}}{h}, \tag{2-32}$$

where ρ_l is the water density, A is the sprinkler link cross-sectional area orthogonal to the flow, κ is water collection efficiency on the sprinkler link, Λ is water latent heat of vaporization, and S is sprinkler link surface. The collection efficiency refers to how many droplets will deposit on the sprinkler link which can be regarded as a constant of 0.97. Ruffino test three sprinklers in both dry and wet conditions, and the comparison with experiment is favorable. However, to successfully predict the

adjacent sprinkler activation, the initial spray characterization should be accurate enough to provide the right amount small droplets. Ruffino and diMarzo's model was adopted in Fire Dynamic Simulator (FDS) to predict the activation of sprinklers.

When the sprinkler is activated in a smoke layer, the smoke layer may be descended due to the spray induced flow and spray cooling effect. The spray drag force could pull the stratified smoke layer downward to the floor and block the corridor, lowering the visibility for people to evacuate. Study of spray and smoke layer interaction is provided in abundant literatures. Cooper [52] studied the sprinkler spray and smoke layer interaction and developed a two layer model to predict the interaction. Cooper categorizes the interaction into 6 conditions based on the smoke layer thickness and the momentum of the spray. Cooper's model requires specification of the sprinkler head characteristics for sprinkler flow rate, drop size and velocity as the model input. Recently, Li [53] conducted experiments on the sprinkler and smoke layer interaction and provided a mathematical model for the interaction to improve the prediction where Cooper's model contradicts with Li's experiments, which showed that increasing the sprinkler pressure, the smoke layer descends lower until it reach to the floor. Li's model agreed fairly well with his experimental data. The model was a little bit lower due to the fact that he ignored the water density distribution which was not uniform in the horizontal cross-section of the spray region. Detailed discussion of spray evaporation, spray cooling, wetting and thermal radiation attenuation are provided in Grant's review paper. The initial spray characteristics are critical for spray and fire interaction study.

2.6 Spray Modeling

Modeling the spray interaction with fire is one of the ultimate goals in fire research. To successfully model the interaction, a list of sub-models must be provided, such as spray initiation model, dispersion model, spray heat and mass transfer model, radiation attenuation model, combustion model, etc. Simulations of spray fire interaction have been investigated by Alpert [54], Bill [55], Nam , Chow [56], Hoffmann [57], Novozhilov [58], Hua [59], etc. Detailed review of suppression simulations can be found in Grant [27] and Novozhilov [60]. The scope of this paper will not cover all aspects of spray modeling, but will emphasize the spray initiation model, which is the first step of spray modeling and is critical for the following spray sub-models.

Several spray initiation models have been explored by different researchers. A simple spray generation model assumes the drop size, drop velocity and drop density are not correlated and those quantities can be specified independently. As mentioned in §2.3, the spray drop size distribution is usually expressed by a combined Log-Normal and Rosin-Rammler distribution. Every time a droplet is generated, the drop size is specified from Eq. (2-4), and the drop velocity is specified using Eq. (2-16). The drop density is assumed to be uniform in the lower hemisphere. This model is very simple but cannot reflect the characters of the sprinkler spray. One can expect that the predicted LDD using this model will not match with the measured LDD. In order to match with the measured LDD, more sophisticated models are developed.

Nam simulated the spray plume interaction. In his simulation an *ad hoc* spray initiation model is provided. Nam's sprinkler spray model simulated the entire spray

by employing a few hundred trajectories and each trajectory was assigned a drop size, drop velocity, mass flow rate, and discharge angle. Nam adjusted droplet discharge speeds and discharge angles until they yielded reasonable matches with the water flux distribution and spray momentum measurements in a scenario without fire. Nam simulated spray from two ESFR sprinklers. The overall drop size distribution is given by a combined Log-Normal and Rosin-Rammler distribution. Ten representative drop sizes were used to describe the CVF profile corresponding to an increase percentage of every 10%. For each drop size, he used 25 trajectories for a total of 275 trajectories, to describe the whole spray, including additional 25 trajectories close to the axis. The drop size distribution was obtained from experiment. However, the discharge speed and discharge angles of the droplets could only be estimated in conjunction with experimental data. The discharge speed was assumed to be uniform, and the discharge angles differed depending on the size of each drop. Starting with an initial estimate, the discharge speed and angles of the trajectories were changed until they yielded a reasonable match to the measured water flux distributions and spray momentums. The discharge angle of the first trajectory with a given drop size was the innermost discharge angle, θ_i, and that of the last trajectory was the outermost discharge angle, θ_o. Any discharge angle between these two trajectories was assigned as

$$\theta_j = \theta_i + (\theta_o - \theta_i)\left(\frac{j-1}{n-1}\right)^P, \tag{2-33}$$

where *j* denotes the *j*th trajectory from the innermost trajectory, *n* is the total number of trajectories (25 for Nam's study), and *p* is an exponent which determines how the

angles will be distributed (1.25 for Nam's study). The mass flow rate allocated to the *j*th trajectory was given by

$$\dot{m}_j = \dot{M}\left(\frac{\theta_j - \theta_{j-1}}{\theta_o - \theta_i}\right), \tag{2-34}$$

where $\dot{M}$ is the total mass flow rate of the water allocated to the given representative drop size. The flow was assumed uniform in azimuthal angle. In order to simulate the water jets close to the axis of the sprinkler, large drops of diameters ranging from 2.0 to 4.0 mm were allocated close to the axis with 10% to 20% higher than the average discharge speed. Fine adjustments were made until the combination of discharge speeds and angles provided results that compared reasonably well to the measurements. After the initial spray adjustment was complete, Nam simulated the spray and plume interaction to predict the plume temperature and ADD. Good agreements were obtained compared with his experiments.

Nam's approach to generate the initial spray was adopted by Hua [59], who used an improved model to simulate the interaction of water spray with a fire plume. Hua's focus was on studying the effect of water spray characteristics on fire suppression mechanism and efficiency, such as water spray pattern (hollow or solid spray cones), drop size and spray flow rate.

Walmsley and Yule measured two sprinklers and simulate the spray dispersion using the Spray-3D code developed by Watkins and his co-workers [61]. The spray is simulated by introducing twenty four droplet parcels every time step. Each of these parcels represents the flow from a tine or a slot, and is given properties accordingly. These properties have been determined by trial and error in order to provide agreement with experimental observations of the sprays. These observations were

made using a number of techniques such as filming and high speed photograph. Droplets flowing from the tines are given an initial trajectory with an azimuthal angle based on that of a tine. Droplets flowing from the slot are given trajectories with an azimuthal angle the same as the slot location, and given a random elevation angle between 10 and 75 degrees below the sprinkler deflector. A random fluctuation of 8 degrees in the plan of the deflector is added for the slot flow. For the spray around the sprinkler arm, the droplet velocity is set lower than elsewhere to take account the arm effect. The drop size was randomly chosen from a log-normal distribution. The different drop size distributions in the proximity of the arms were not considered in these predictions. For conventional sprinkler models, it has been assumed that half the water flows along the tines. For the spray sprinklers whose arc length of tine and slot is different, the flow weighting is based on the arc length ratio between tine and slot. The simulated water deliver density was compared with the measurement at locations along the sprinkler arm, perpendicular the sprinkler arm, and at 45 degree angle to the plan of the arms. The prediction shows good agreement with his measurements.

Fire Dynamic Simulator (FDS) is a popular tool in the area of fire simulation. The spray initiation model has been improved in FDS. Early version of FDS (Version 4) has a simple spray generation model. The combined Log-Normal and Rosin-Rammler function was used for the drop size distribution. The user can specify the initial spray location (radial distance from sprinkler head). In the elevation direction, the user can specify an angle range and the spray will be uniformly distributed between these two angles. Two options can be used for specify spray velocity. First option is to set all the droplets a constant velocity. Second option is to set the velocity as a function of

elevation angle (θ) and azimuthal angle (ψ) point by point if the detailed spray velocity distribution is known. If using the first option to specify the velocity, there is no need to set the flux. However, if using the second option for velocity, the local flux should be specified the same way as velocity does. The drop size can be set using the global drop size distribution, or can be set as a function of solid angle. More information can be found in FDS user guide and technical guide [62, 63]. The spray generation method has changed in the latest version of FDS (Version 5). A spray pattern table was used to provide the detail distribution of the spray. Detailed spray information, such as velocity and flux fraction, can be specified for a certain solid angle. However, there is less freedom to specify the drop size information.

2.7 Conclusion

In this study, the initial spray characteristics have been reviewed both experimentally and theoretically. Spray fire interaction and spray modeling is discussed briefly to address the importance of initial spray characteristics.

Sprinklers work successfully in fire suppression applications. The standard test evaluates the ability of sprinklers to deliver required amount of water to the cover area. However, the standard tests conducted in cool air environments are not enough to provide a comprehensive evaluation for sprinklers. To better understand the spray suppression mechanisms, research has been performed to study the spray fire interaction. The initial spray characteristics are very important in order to understand how much spray penetrates the fire plume, how much spray evaporates, how the spray affects the adjacent sprinkler activation and how the smoke layer changes with spray, etc. Efforts have been devoted to initial spray measurements using different

techniques. The overall spray drop size has been characterized following a (-1/3) Weber number power law. The spray characteristic drop size is also a complex function of sprinkler geometry.

Theoretical study based on the atomization physics were performed trying to related the characteristic drop size with sprinkler geometry. Preliminary results were obtained to quantify the spray characteristics from the tine and slot flows respectively. However, the effect of sprinkler arms has not been explored comprehensively.

Spray initiation models were addressed in the application of modeling, which is the first step in spray modeling and critical for the sub-models. Several models were used which provided a connection between initial spray characteristics and spray fire interaction modeling.

Chapter 3: Quantifying the Initial Spray from Fire Sprinklers

Ning Ren, Andrew F. Blum, Ying-Hui Zheng, Chi Do, and André W. Marshall*

Department of Fire Protection Engineering

University of Maryland, College Park, MD, USA

3.1 Abstract

The performance of water-based fire suppression systems is governed largely by the spray discharge characteristics associated with the nozzle geometry and injection conditions. In many nozzle configurations such as sprinklers, this initial spray is produced by injecting a water jet onto an orthogonal deflector, resulting in thin, unstable, radially expanding streams. These streams ultimately disintegrate into a complex population of drops forming the spray. The initial spray is generated in distinct stages, which include sheet formation, sheet breakup, and ligament breakup. A Sprinkler Atomization Model (SAM) has been developed based on these physics to predict the initial drop velocity, location, and size based on the nozzle geometry and injection conditions. The initial spray from a simplified yet realistic sprinkler geometry has been quantified through detailed measurements to provide insight into these atomization processes and to evaluate SAM performance. Flow visualization revealed that the deflector produces a continuous radially expanding stream resulting from the flow directed over the tines and a connected underlying orthogonal stream resulting from the flow through the spaces. The measured and predicted breakup locations and drop sizes follow $We^{-1/3}$ scaling laws, previously established by other researchers in similar canonical configurations. However, SAM over predicts the

volume median drop diameter by as much as 40%, probably due to the absence of models to characterize the orthogonal stream underlying the radially expanding sheet. This orthogonal stream generated by the spaces was measured to consist of nearly 50% of the flow and produces smaller drops than the radially expanding sheet. The detailed breakup mechanisms for this stream are currently being characterized to improve fidelity of the atomization model.

3.2 Introduction

Automatic fire sprinklers are accepted as the fire protection system of choice for a wide variety of applications. To support the development of many types of fire protection systems and the design of fire safe environments, modern engineering practices are currently being established like performance-based design, which requires the prediction of fire behavior using physics-based analytical methods and tools. Despite the simplicity of the basic operating principles for fire sprinklers, the complex physics governing water-based suppression including multi-phase transport processes, flame sheet extinction, and extinction of condensed phase reactions, present profound analytical and modeling challenges. Even the physical mechanisms controlling the sprinkler's simple action to generate a dispersed spray are quite complex and do not yield readily to analysis. Yet, as advanced fire protection engineering practices continue to gain popularity, the need to model fire sprinklers for suppression system and even component analysis is inevitable. In this study, the challenge to characterize the initial spray from sprinklers is addressed to advance understanding of the atomization process in fire sprinklers and to develop models for predicting sprinkler spray characteristics.

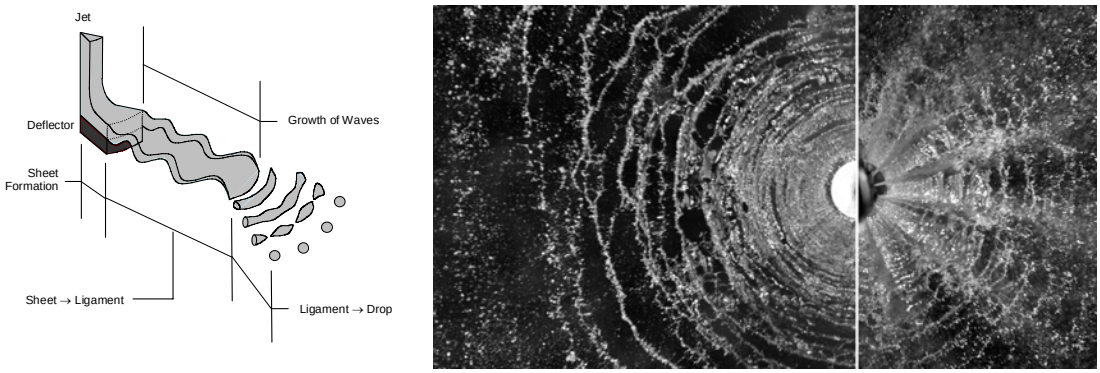

(a) (b)

Figure 3.1 (a) Illustration of the atomization process [21]; (b) Photograph of the atomization process with p = 2.07 bar for a solid deflector nozzle (left) having geometry similar to the nozzle used in this study (right).

The atomization process for sprinklers can be described fundamentally by distinct stages, as illustrated and photographed in Figure 3.1 (a) and (b), respectively. The injector forms a vertical water jet that impinges upon a deflector. The redirected jet forms a thin, horizontal film traveling along the top of the deflector. Once the film travels past the deflector, it becomes an unconfined, expanding sheet. The sheet expands radially outwards from the deflector becoming increasingly unstable creating aerodynamic waves. These sinuous waves grow until the sheet begins to breakup at a critical wave amplitude. The sheet disintegrates into ring-like ligaments that are also inherently unstable. Dilatational waves grow on the ligaments until they reach a critical wave amplitude, initiating ligament breakup into even smaller fragments. These fragments will eventually contract to form spherical drops. A more detailed discussion of these atomization processes can be found in Dombrowski [26], Wu [21] and Ren [42].

The key characteristics of fire suppression sprays have been summarized recently in a review paper by Grant and Drysdale [27]. Detailed sprinkler spray measurements

have been reported by Dundas [13], Yu [2] and Wendt and Prahl [9]. More recent studies have been conducted by Widmann et al. [18, 19], Sheppard [10] and Putorti [20]. These studies characterized drop sizes, volume flux distributions, and velocities produced by a wide variety of sprinkler configurations operating over a range of injection pressures. From this body of work, it is clear that the drop size is reduced with increasing pressure as quantified by the empirical relationship $d_{v50} / D_o = CWe^{-1/3}$. Although these studies verified this $We^{-1/3}$ trend more or less, the constant of proportionality varied significantly between sprinkler configurations. The simple scaling law provides very little insight into the important parameters governing the initial spray from sprinklers suggesting that higher fidelity predictive methods are required to explain the effect of sprinkler geometry on the spray. In order to move beyond empirical relationships to higher fidelity models, a better understanding of the basic atomization mechanisms from sprinklers is required.

Fire sprinklers are based on variations of the essential impinging jet configuration. A focus on this canonical configuration is therefore useful for understanding basic atomization physics relevant to sprinkler atomization. From this perspective, Blum [11] and Ren [42] have conducted experimental and modeling studies providing break-up details, drop size, and dispersion characteristics in the impinging jet configuration operating at sprinkler injection pressures. Even more fundamental studies have been conducted by Villermaux and Clanet [40] in this configuration. They observed drop formation by rim breakup at the sheet as opposed to the ligament breakup mode observed by Dombrowski [26]. However, Blum and Ren observed that the rim breakup mode occurs at lower pressure (or *We*) while the ligament breakup

mode occurs at higher pressures as shown in Figure 3.1 (b). Blum and Ren observed many similarities between atomization measurements taken in realistic sprinkler configurations and canonical impinging jet configurations confirming that the fundamental atomization mechanisms described in Figure 3.1 provides an appropriate basis for the Sprinkler Atomization Model (SAM) [21]. The current study focuses on the development and evaluation of SAM based on comparisons with detailed atomization measurements taken in a simplified yet realistic sprinkler configuration.

3.3 Approach

When dissected, the anatomy of a sprinkler is complex. A thoughtful approach is thus required to evaluate the effect of individual features on spray discharge characteristics. Figure 3.2 details the nozzle configuration investigated in this study as well as the important geometric characteristics common to most sprinklers. A commercially available Tyco D3 nozzle was selected to represent a standard sprinkler due to its similarities with conventional sprinklers and its distinct well-characterized geometric features. Table 3.1 summarizes the important geometric and flow characteristics for all three nozzles used in this study. Detailed measurements were taken at various stages in the atomization region and also within the sprinkler spray to provide insight into the spray formation process, while providing valuable data for evaluation of University of Maryland's Sprinkler Atomization Model (SAM).

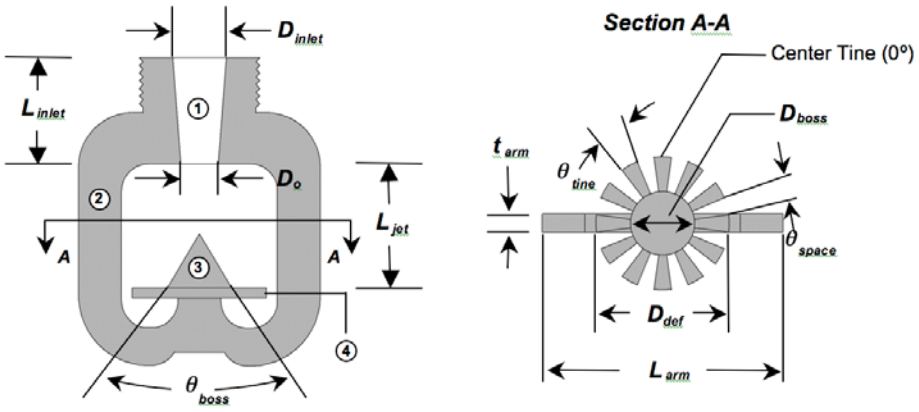

Figure 3.2 The anatomy of a sprinkler: (1) Inlet (2) Frame Arms (3) Boss (4) Deflector.

Table 3.1 Nozzle Dimensions

Inlet					Deflector			Boss	
D_{inlet} (mm)	L_{inlet} (mm)	L_{jet} (mm)	D_o (mm)	K-Factor (lpm/bar$^{1/2}$)	D_{def} (mm)	θ_{tine} (º)	θ_{space} (º)	D_{boss} (mm)	θ_{boss} (º)
19.5	19.7	23	6.35	25.9	25.4	20	10	12	65

3.3.1 Model

The atomization process in SAM is described with physics based sub-models for sheet formation, sheet trajectory, sheet breakup, and ligament breakup stages. Although first principle multiphase flow models have been established, they are not suitable for large-scale multi-physics engineering level applications. To simplify the complex multi-phase interactions, SAM uses free surface flow theory in the sheet formation and trajectory sub-models, and stability theory for the breakup sub-models. SAM provides the initial velocities, locations, and drop sizes that characterize the spray. After the spray is formed, the problem becomes one of a discrete liquid phase in a continuous gas where spray dispersion can be predicted through Lagrangian tracking models available in codes such as FDS [63]. While a summary of SAM is provided in this section, a detailed description can be found in Wu et al. [21].

3.3.1.1 Sheet Formation and Trajectory

The liquid sheet in sprinklers is formed by impinging a liquid jet onto a deflector. The sheet thickness and velocity are determined from Watson's theory [46] based on a free-surface similarity boundary-layer concept. Following Watson's turbulent theory, when boundary thickness is smaller than the sheet thickness, the sheet thickness is given by

$$T = \begin{cases} D_0^{\,2}/8r + 0.0245 D_0^{\,1/5} r^{4/5} / \mathrm{Re}^{1/5} & T > \delta \\ 1.022 D_0^{\,2}/8r + 0.0224 r^{5/4} / (D_0 Re)^{1/4} & T > \delta \end{cases}. \tag{3-1}$$

where $Re = \rho_l U D_o / \mu_l$ is the Reynolds number and the boundary-layer thickness is $\delta = 0.303 D_0^{\,1/5} r^{4/5} / Re^{1/5}$. In order to show the effect of viscous interaction with the deflector, a non-dimensional sheet thickness is defined as the actual thickness compared to an inviscid sheet thickness solution, which is given by $\beta = T / T_0$ where $T_0 = D_0^{\,2} / 8r$. The non-dimensional form of sheet thickness is the sheet thickening factor, which is

$$\beta = \begin{cases} 1 + 0.196\,\mathrm{Re}^{-1/5} \left(r / D_0\right)^{9/5} & T > \delta \\ 1.022 + 0.179\,\mathrm{Re}^{-1/4} \left(r / D_0\right)^{9/4} & T < \delta \end{cases}. \tag{3-2}$$

The average velocity of sheet at the edge of deflector is determined by

$$U = Q / 2\pi r_d T_0 \beta\,. \tag{3-3}$$

where r_d is the radius of the deflector. The most important parameter in sheet formation is the sheet thickening factor β and average sheet velocity U. The sheet velocity governs the wave growth rate and the sheet thickness influences the diameter of the drop. It is also worth noting that the velocity profile of the sheet will have some

influence on the sheet break-up. However, in the following analysis, the average sheet velocity is used to simplify the problem.

After leaving the deflector, the external forces acting on the liquid sheet are only the friction force and gravity force. Distinct from a discrete object (i.e. drop), the liquid sheet is a continuous expanding stream, which has a more complex trajectory. Furthermore, the thickness of the sheet changes as the sheet expands radially outwards. Internal forces also affect the trajectory of the sheet especially when the liquid sheet is very thin and the curvature of the trajectory is large. To determine the trajectory of the sheet, a group of differential equations have been developed by Ibrahim [47]:

$$\begin{cases} rT\dfrac{dU}{d\xi}+UT\dfrac{dr}{d\xi}+Ur\dfrac{dT}{d\xi}=0;\dfrac{dr}{d\xi}=\sin\alpha;\dfrac{dz}{d\xi}=\cos\alpha \\ \rho_l U\dfrac{dU}{d\xi}=-\dfrac{\rho_a U^2}{2T}[0.79(1+150T/r)Re_{sh}^{-1/4}]+\rho_l g\cos\alpha\,. \\ \rho_l U^2\dfrac{d\alpha}{d\xi}=-\dfrac{2\sigma}{T}\left(\dfrac{\cos\alpha}{r}-\dfrac{d\alpha}{d\xi}\right)-\rho_l g\sin\alpha \end{cases} \tag{3-4}$$

The trajectory model is based on curvilinear body-fitted coordinates where r and z are the radial and vertical coordinate of the cylindrical coordinate system. The variable ξ is the position in curvilinear body-fitted coordinate, T is the local sheet thickness, U is the local sheet velocity, α is the angle between the median streamline and axial direction z, and g is the gravitational acceleration constant, $Re_{sh}=2\rho_a r_d\,|U_a-U|/\mu_a$.

The initial conditions are specified where the sheet leaves the deflector $(\xi=0)$. The boundary conditions for the sheet velocity and thickness are provided by the

impinging jet model. Because there are no good models to predict the initial angle, the initial angle is currently determined empirically. It is not possible to solve the non-linearly equations analytically, a fourth order Runge-Kutta method is used to find the solution of U, T, θ, r, z . The purpose of the trajectory model is to predict the local sheet thickness and sheet velocity. In previous atomization studies, the sheet velocity was regarded as a constant by all researchers and the sheet thickness was also treated as a simple function of radius. The trajectory sub-model provides those values with more fidelity for improved coupling with the sheet break-up model.

3.3.1.2 Breakup

As shown in Figure 3.1, the sheet formed by the sprinkler is inherently unstable resulting in the growth of aerodynamic waves, which cause the sheet to break. The wavelength at sheet break-up governs the resulting fragment size and ultimately the ligament diameter. A theory based on linear stability has been developed by Dombrowski [26] to predict the wave instability for two dimensional waves in an inviscid gas. In this model, sinusoidal waves are assumed to exist on the liquid sheet. A force balance is performed on the sheet considering inertial, pressure, viscous, and surface tension forces associated with the wave displacement. After considerable reformulation and simplification, the force balance can be expressed in terms of the growth rate of the waves present on the liquid sheet

$$\left(\frac{\partial f}{\partial t}\right)^2 + \frac{\mu}{\rho_l} n^2 \left(\frac{\partial f}{\partial t}\right) - \frac{2(\rho_a n U^2 - \sigma n^2)}{\rho_l T} = 0 . \qquad (3\text{-}5)$$

where t is time, f is a dimensionless wave amplitude defined by $f = \ln(A / A_0)$, A is the wave amplitude and A_0 is initial wave amplitude, μ is the liquid viscosity, T is

sheet thickness, n is wave number defined by $n = 2\pi / \lambda$, and λ is wavelength. The sheet velocity, U, and sheet thickness, T, is given by the trajectory model. The trajectory and sheet break-up analysis are only weakly coupled. According to the linear wave dispersion theory, the wave amplitude is small compared to the wavelength. The effect of waves on the sheet trajectory can be neglected. However, the sheet thickness and velocity significantly affect the wave growth rate. From the wave dispersion equation, it is apparent that the pressure (or inertial) force accelerates the wave growth while the surface tension attenuates the waves. As the density ratio, ρ_{air} / ρ_l increases, the wave growth rate also increases. In real fire scenarios, the gas temperature increases and the density decreases. As a result, the wave growth rate will decrease. Although the wave number, n, can be any real number, there is only one wave number that makes the wave grow the fastest. This critical wave number, n_{crit}, is considered to be the most unstable wave that will first lead to breakup. The sheet won't breakup until f reaches the critical dimensionless wave amplitude f_0. In Dombrowski's theory, f_0 is a constant with a value of 12 regardless of working conditions. Other researchers also found that f_0 is a constant, which is close to 12. It should be noted that in our experiment, f_0 was assumed to be a function of nozzle configuration and could be determined by experiment. The break-up time is recorded when f reaches f_0. From the trajectory model, the corresponding sheet velocity, sheet thickness, and the break-up location r_{sh} are found according to the breakup time.

The thin flapping sheet is assumed to break up into ring-like fragments having a radial extent of one half wavelengths. The ligament diameter can be determined from conservation of fragment mass. The ligament diameter is not only related to the ligament mass, but also related to the sheet break-up location. The sheet break-up analysis reveals that the critical wave number and sheet break-up location are important quantities governing atomization behavior. In this study, the sheet break-up location is carefully measured for evaluation of the atomization model. The ligaments produced by the sheet are also unstable. Different from the sheet break-up model, the surface tension force plays a positive role for the wave growth. Weber [35] provided an analysis (similar to the sheet breakup analysis) where the critical wave number is given by

$$n_{cirt,lig} d_{lig} = \left[\frac{1}{2} + \frac{3\mu}{2(\rho_l d_{lig} \sigma)^{1/2}} \right]^{1/2} . \tag{3-6}$$

The unstable waves on the ligament are dilational waves, which will lead to break-up every one wavelength. From conservation of mass, the drop diameter can be expressed as

$$d = d_{lig}^{2/3} \left(3\pi / n_{crit,lig} \right)^{1/3} . \tag{3-7}$$

The ligament breakup time related to the ligament diameter is

$$t = 24 \left(\frac{2\rho_l}{\sigma} \right)^{1/2} \left(\frac{d_{lig}}{2} \right)^{3/2} . \tag{3-8}$$

and the initial drop locations are estimated by $r = r_{sh} + U_{lig} t$.

The important physics and associated governing equations have been summarized. SAM provides both deterministic and stochastic formulations for

predicting the initial spray based on these governing equations. The deterministic formulation provides characteristic values for the initial drop velocity, location, and size; however, fire suppression sprays show strong stochastic behavior. For example, the sheet does not always breakup at the same distance and the drops do not have only one diameter. In order to model these stochastic behaviors, probability distributions are introduced into the model to treat the various stages of the breakup process. The sheet critical breakup amplitude, the sheet breakup wavelength, and the ligament breakup wavelength are all treated stochastically. This physics-based technique provides an alternative to specifying a standard distribution about a calculated characteristic drop size. The stochastic model ultimately provides distributions for initial drop velocity, size, and location. A detailed discussion on the stochastic model is provided by Wu [21]

3.3.2 Measurements

Sheet breakup, volume density, and local drop size experiments were conducted to quantify discharge characteristics for the representative nozzle. The experiments were performed at 0.69, 1.38, 2.07, and 2.76 bar to investigate the effect of injection pressure on spray characteristics. Table 3.1 summarizes the pertinent experimental injection parameters including injection pressure p, jet velocity U_{jet}, nozzle flow rate Q, Weber number We, and Reynolds number Re.

3.3.2.1 Flow Visualization

Photographic and Planar Laser Induced Fluorescence (PLIF) techniques were used in this study to visualize the breakup process and measure sheet/ligament breakup locations. These experiments were conducted inside a vented 1.7 m x 1.7 m

x 1.9 m chamber illustrated in Figure 3.3. Using a purely photographic method, the flow was illuminated with two synchronized Canon EX Series flashes reflected from above and orthogonal to the radially expanding sheet, and having discharge times of 15.6 s. A Canon 40D 10.1 MP Digital SLR camera was placed above the nozzle to photograph the sheet breakup producing images similar to the one depicted in Figure 3.1. At least 20 images were recorded at each experimental condition. Breakup locations were obtained in each image at 37 equally spaced circumferential stations between – 45° and 45° and relative to the centerline of a reference tine. Planar Laser Induced Fluorescence was utilized to visualize a cross-section of the expanding sheet. Illumination was provided by a 500 mW, air cooled, argon ion laser and a 20 face rotating mirror spinning at 20 Hz. The water supply was seeded with Rhodamine 6G dye having a mass concentration of 0.5 mg/l. The sheet was imaged with a low noise, 16-bit, 2.0 MP, Cooke SE © high-speed digital video camera fitted with a high pass optical filter operated with an electronic shutter speed of 900 μs at 5 frames per second. These fluorescent planar images provided insight into the structure of the

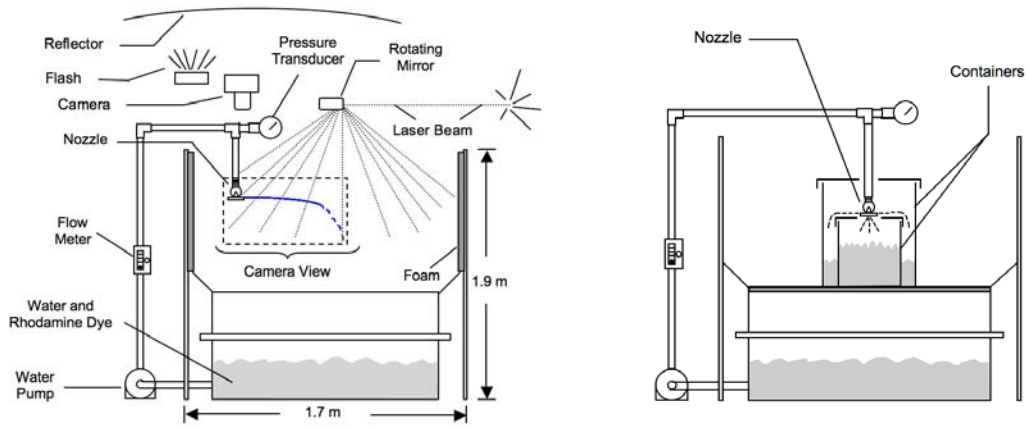

(a) (b)

Figure 3.3 (a) Flow visualization experimental set-up; (b) Flow-split experimental setup.

continuous stream before breakup and the liquid fragments during the breakup process.

3.3.2.2 Flow Split

The fraction of the total flow divided between the radial expanding sheet (generated by flow along the tines) and the downward directed streams (generated by flow through the spaces) is measured with two concentric 38 L and 144 L containers. The inner container collects the flow through the spaces and the outer container collects the radially expanding flow from the tines as shown in Figure 3.3 (b). The opening in the lid of the small container is designed to fit the size and shape of the sprinkler deflector exactly, providing complete separation between the space and tine generated flow streams.

3.3.2.3 Dispersion

Volume density distributions were obtained using a 2.6 m patternator positioned 1 m below the nozzle deflector surface and 1 m above the floor. To permit analysis of the entire sprinkler spray, volume density measurements were conducted inside a large 8.6 m x 7.2 m x 3 m room located at the Maryland Fire Rescue Institute, as illustrated in Figure 3.4. The nozzles were discharged for 10 minutes to average over short time scale aerodynamic or water supply fluctuations, after which the water in each cup was weighed to determine the volume at each radial station. Volume density distributions were aligned with the middle of the center tine (0° station) and the adjacent space (15° station).

A characteristic dispersion length scale, R, first introduced by Wendt and Prahl [9], was employed to facilitate analysis of the measurements. This reference quantity

provides an inviscid radial location at the measurement elevation for each experimental condition, and is given by

$$R = (v_o)_r \left(\frac{2h}{g}\right)^{1/2} \left[\left(1 + \frac{(v_o)_z^{\,2}}{2gh}\right)^{1/2} - \left(\frac{(v_o)_z^{\,2}}{2gh}\right)^{1/2} \right]. \qquad (3\text{-}9)$$

where h is the measurement elevation (below the nozzle), g is the gravitational constant, $(v_o)_r$ is the initial radial sheet velocity, and $(v_o)_z$ is the initial axial sheet velocity. The velocity magnitude is estimated from the model described in §3.3.1.1 and the angle is determined empirically from flow visualization experiments, yielding sheet velocities $(v_o)_r$ and $(v_o)_z$. The resulting volume density distributions in the r/R coordinate describe the relative effect of drag on dispersion. The volume density measurements were described non-dimensionally so that $\sum q_j' \Delta r^* = 1$, where $\Delta r^* = \Delta r / R$ is the dimensionless station width and the dimensionless linear density of dispersed volume flow, q_i', is given by

$$q_j' = \frac{q_j}{Q/\pi R^2}\left(2r^*\right). \qquad (3\text{-}10)$$

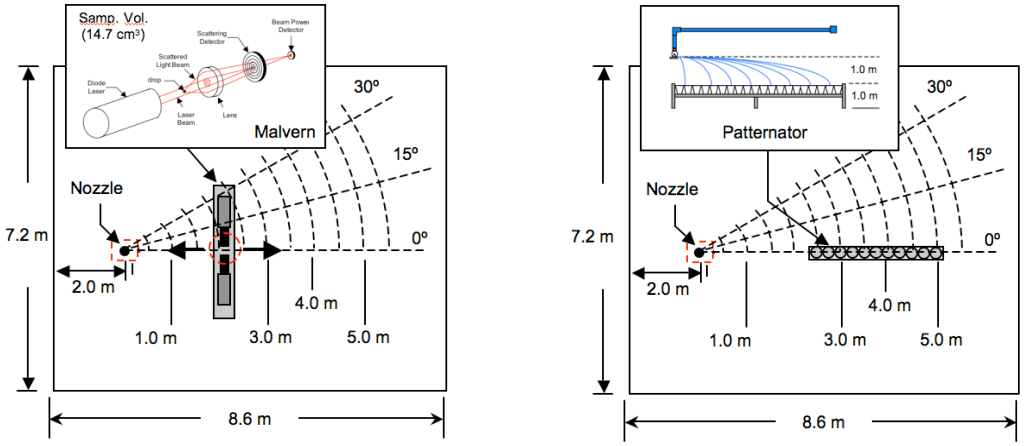

Figure 3.4 (a) Drop size measurement experimental set-up; (b) volume flux distribution experimental set-up.

where q_j is the linear volume density measured at measurement location *j* and Q is the flow rate. The length scale *R* was modified at every experimental condition for the measurements aligned with the tine (0º). For measurements aligned with the space, the adjacent tine-aligned *R* values were used for the reference length scale.

3.3.2.4 Drop Size

Local drop size measurements were also conducted inside the large room illustrated in Figure 3.4 to investigate the drop size variations along the radial span of the spray. An overall drop size distribution and a characteristic drop size, d_{v50}, for each experimental condition can be derived from these measurements. The local drop sizes were measured using a Spraytec spray particle analyzer developed by Malvern Instruments. This laser-based instrument employs a light diffraction technique for counting and sizing drops or particles as illustrated in Figure 3.4. Local measurements were taken at 12 radial stations starting at 0.5 m and separated by 0.5 m, positioned 1 m below the nozzle and 1 m above the floor. The Spraytec measurement volume was configured to be 12 mm in diameter and 130 mm long. At least 100 drops were estimated to fill the measurement volume at any given station. Measurements were taken at each station for 1 minute at 50 Hz providing local drop size distribution realizations. The drop sizes were measured at the same circumferential stations as the volume flux experiments. The drop size distribution determined by the Malvern RTSizer software is a local drop size distribution within the Spraytec's measurement volume. However, in this study an overall characteristic drop size, d_{v50}, for the entire spray is of interest. To determine the overall d_{v50} the local Spraytec measurement is weighted with the local volume density measurements

to transform the spatial Malvern measurements into the flux-based drop size distributions described by

$$QF_i = Q_i / Q;\ Q_i = \sum_{j=1}^{N} (q'_j)\Delta r^* VF_{i,j};\ Q = \sum_{i=1}^{M} \sum_{j=1}^{N} (q'_j)\Delta r^* VF_{i,j}. \qquad (3\text{-}11)$$

where $VF_{i,j}$ is the local spatial volume fraction within the Spraytec measurement volume for the *i*th drop size at the *j*th measurement location. The spray quantities Q_i and Q are estimates of the drop-wise volume flux and total volume flux from all drops, respectively. The quantity QF_i is the flux-based drop-wise volume flux fraction for the entire spray. Drop size distributions based on 60 drop size bins ranging from 0.29 – 2000 μm are easily calculated from QF_i for determining flux based drop characteristics.

3.4 Results

Flow visualization, breakup characterization, drop size measurements along with atomization modeling provided insight into the discharge characteristics of a simple yet realistic sprinkler geometry operated over a range of operating pressures. The nozzle geometry detailed in Figure 3.2 and Table 3.1 was operated at 0.69, 1.38, 2.07, and 2.76 bar. The results from the combined measurements and physics based atomization model are analyzed to help explain the connection between the measured spray behavior and the well-characterized nozzle geometry.

Flow visualization revealed the structure of the thin sheet created by the nozzle. A radially expanding sheet is formed from the jet impinging on the tined deflector used in this study as shown in the right most image presented in Figure 3.1 (b). This

sheet disintegrates into ring-like ligaments similar to the reference sheet created from the solid deflector (having D_{def} = 25 mm and L_{jet} = 75 mm) shown on the left in the same figure. However, the sheet structure generated in the realistic tined configuration breaks up earlier than the sheet generated in the canonical configuration and clearly has a more complex three dimensional structure. Although the sheet is continuous, despite the presence of the spaces in this configuration, there appears to be an underlying flow stream aligned with the spaces. This underlying flow stream is deliberately imaged out of focus using a narrow depth of field to better visualize the continuous radially expanding sheet in the overhead images shown in Figure 3.1 (b). The underlying stream is better represented in the Figure 3.5 PLIF images obtained orthogonal to the central tine (0°) at various distances from the centerline. These planar images show flow through the spaces in the 12.7 mm plane just at the edge of the deflector. Perhaps, the development of an underlying orthogonal sheet structure is most clearly imaged in the 22.7 mm plane. By 62.7 mm the orthogonal sheet appears to have disintegrated completely; however, remnants of the radially expanding sheets aligned with the tines appear to persist. An atomization model has yet to be developed describing disintegration of the flow stream generated by the spaces. To support model developed, more detailed visualization is currently being conducted to capture the important atomization mechanisms in this flow stream.

Determination of the flow split between the radially expanding sheet created from the tines and the orthogonal flow created with the spaces is crucial, not only to understand the contribution of the orthogonal stream to the overall spray, but also to determine the sheet thinning impact from flow divergence through the spaces. This

sheet thinning effect is accounted for in Eq. (3-3). For the nozzle used in this study 51% of the flow was directed into the radially expanding sheet and approximately 49% of the flow was directed into the orthogonal stream (virtually independent of p), which would result in a significantly thinner sheet than that generated in the canonical configuration and explain the earlier sheet breakup.

Detailed analysis of the flow visualization images provides quantitative data for evaluating modeling results at intermediate stages of the atomization process. Consistent with the images provided in Figure 3.1 (b), measurements and modeling results are presented in Figure 3.6 showing that drops do not initiate at the deflector edge, but instead are formed at some distance beyond the deflector depending on the operating conditions. In fact, even after the sheet breaks up, ligament disintegration must be complete before drops are formed. It is only after disintegration is complete (i.e. drops are formed) that discrete drops should be introduced into the continuous flow domain for CFD analysis. The measured sheet and breakup location

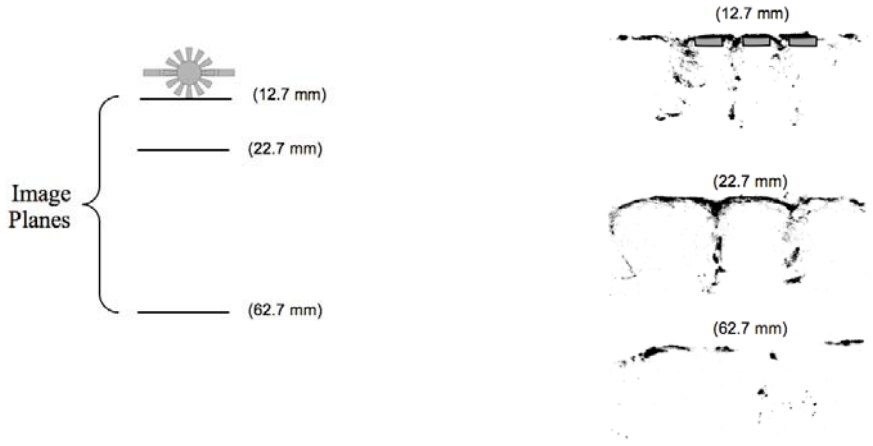

(a) (b)

Figure 3.5 Inverted PLIF images depicting flow through sprinkler spaces; (a) top view of measurement locations; (b) three-dimensional stream generated with a tined deflector.

distributions at p = 2.07 bar presented in Figure 3.6 (a) show that the breakup process is indeed stochastic having Gaussian-like distributions. In fact, these distributions demonstrate that sheet breakup and drop formation events frequently overlap following visual observations from images.

The mean sheet and ligament breakup results showing the effect of injection condition are provided in Figure 3.6 (b). The $We^{-1/3}$ scaling law first observed by Huang [38] in opposing impinging jets in the high We regime is also observed in this more complex sprinkler configuration. The results in this study show that the sheet breakup and ligament breakup locations follow this scaling law. At very high We (i.e injection pressure), the agreement between the modeled and measured sheet breakup locations is excellent; however, at low pressure the scaling law does not apply. This breakup location deviation is consistent with observations made from flow visualization showing that at low pressure the atomization behavior changes from a 'sheet to ligament' breakup mode to one where the sheet breaks up directly to form drops. The divergent low-pressure behavior is consistent with sprinkler operating recommendations where low pressure injection is avoided to ensure a well-defined spray.

The measured drop size distribution taken at the 0° station aligned with the tine at p = 2.07 bar is provided in Figure 3.7 (a). The measured drop size distribution follows a log-normal Rosin-Rammler distribution with d_{v50} = 393 μm and γ = 2.0. The measured distribution shows that the drop sizes range from 70 μm to 2 mm. The drop size model performance is evaluated through comparing the dashed predicted CVF curve and the solid modeled CVF curve. The shape of the modeled and

measured CVF distributions is very close; however, the model is unable to predict the small drops created by the sprinkler configuration with its distribution starting at 200 μm. The measured small drops may result from the orthogonal stream or another breakup mechanism not accounted for in SAM. Drop size measurements at a variety of injection pressures are plotted against *We* in Figure 3.7 (b). Measurements at the space (15°) and tine (0°) measurement stations appear to follow the $We^{-1/3}$ scaling law at sufficiently high operating pressures. It is also clear from the measurements that orthogonal space stream produces a distinctly different and smaller drop size than the radially expanding sheet formed from the tines.

At first blush, the stochastic model shows a significant over-prediction of the measured drop size. The deviation is expected when comparing the predictions and the measurements aligned with the space, because the model does not account for orthogonal sheet breakup mechanisms. However, the model is based on sheet breakup mechanisms and accounts for the significant loss of flow from the sheet into the orthogonal space stream. Considering the fidelity included in the model, better agreement was expected and this modeling discrepancy deserves closer examination. To understand this discrepancy, the significant difference between drop sizes measured at the station aligned with the center of the tine (0°) and the station aligned with the narrow stream generated through the space (15°) should be recognized. Next it should be noted that just over 50% of the flow is directed into the sheet, while almost 50% of the flow forms the orthogonal stream produced by the spaces. Although the two measurements were aligned with the center of the tine and space generated streams, the drops from these streams may be dispersed widely even

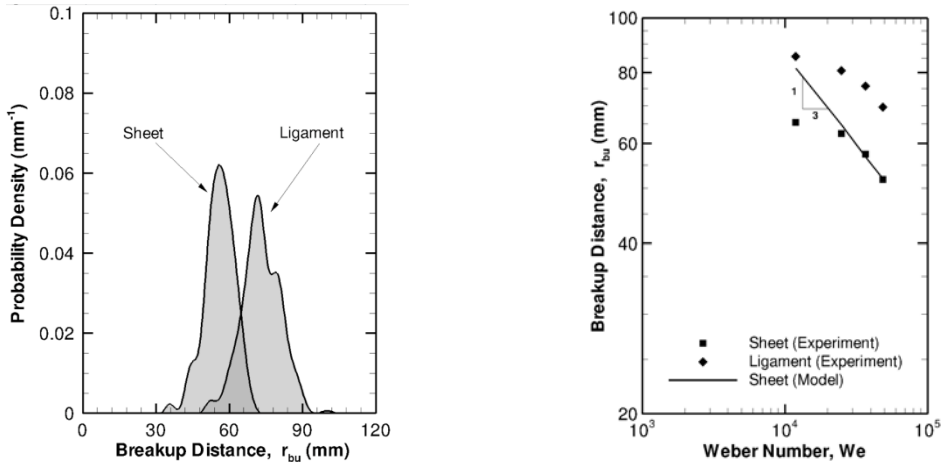

(a) (b)

Figure 3.6 (a) Breakup distance distributions for the sheet and ligaments (p = 2.07 bar); (b) Breakup distances at various injection pressures (or We).

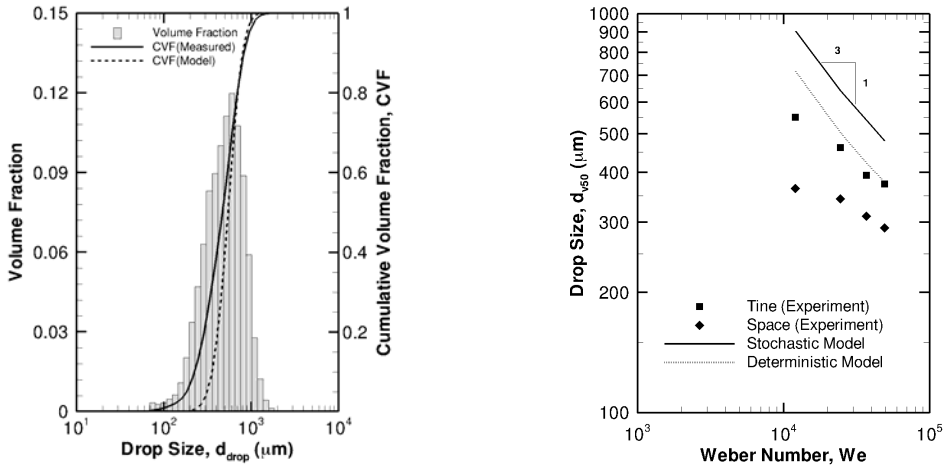

(a) (b)

Figure 3.7 Drop size measurements and predictions; (a) 0° station distribution at 2.07 bar; (b) volume median drop diameter at various injection pressures (or We).

reaching the adjacent measurement stations 1 m below the deflector. This dispersion could result in contamination of the drop size measurements and prevent definitive measurement of the distinct initial drop sizes originating from the streams. The mixing of the sheet and space generated drops at their respective measurement stations would bias the sheet generated drop sizes downward and the space generated drop sizes upward. Indeed the volume density measurements provided in Figure 3.8

reveal this mixing effect. Figure 3.8 (a) shows a strong volume density peak close to the nozzle centerline at the 15° station aligned with the space. The high volume density near the centerline is consistent with expectations from this configuration, where flow from the jet is forced downward through the spaces by the boss. In contrast, the volume density at the 0° station aligned with the tine shows distinctive inner and outer peaks at all operating pressures. It becomes apparent from comparison of the distributions at the 0° and 15° stations that these two distinctive peaks result from drops generated by the inner directed space flow streams and the outer directed tine generated streams verifying the previous dispersion, mixing and biasing arguments. The small secondary peaks observed at the 15° station also appear to result from this dispersion effect. With this bias in mind, it follows that SAM predictions from the stochastic model (based purely on sheet breakup physics) would produce larger drop sizes than the measurements even for the station aligned with the tine generated stream. Furthermore, it appears that the good agreement between the

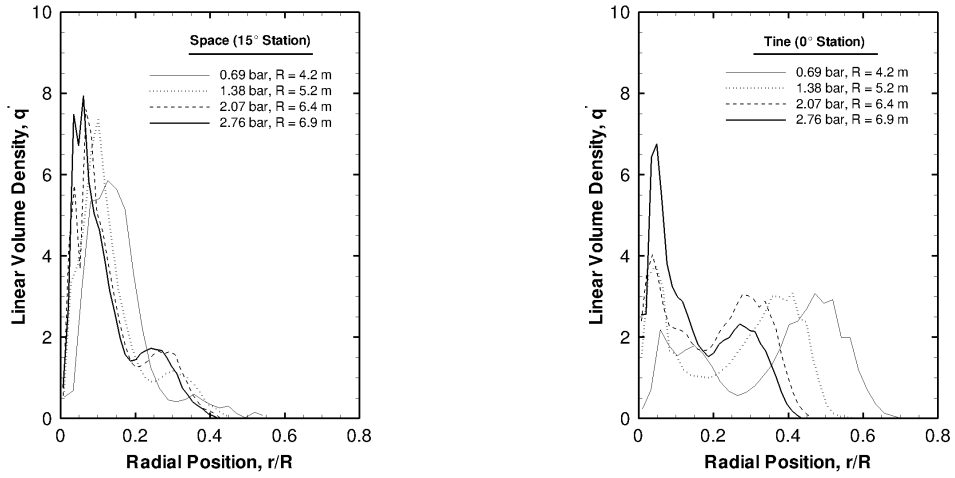

Figure 3.8 Linear volume density for all injection pressures (or We);(a) 15° station aligned with space; (b) 0° station aligned with tine.

lower fidelity deterministic model and the measurements aligned with the tine is purely fortuitous as the deterministic model is missing models not only for the space stream breakup physics, but also for stochastic breakup effects.

The volume density flux measurements provide excellent information to support understanding the drop size predictions and measurements, but they are also interesting in their own right. Figure 3.8 (a) shows a central peak corresponding to the space generated drops which consistently move inward with pressure (except perhaps the 0.69 bar condition). More convincingly, Figure 3.8 (b) also shows the outer tine generated peaks move inward with increasing pressure. Recognizing that the location has been normalized with the maximum inviscid radial extent a drop would span before reaching the measurement elevation, the dimensionless location reveals information about the drag on the drops and thus the drop sizes. The outer peaks move in with increasing pressure suggesting that the spray consists of smaller drops, which is consistent with the measurements and model predictions presented in Figure 3.8.

3.5 Conclusion

This study helped to explain the relationship between discharge characteristics and the nozzle geometry through detailed spray measurements and physics based atomization modeling. The comprehensive set of measurements provided insight into the spray generated by a simple yet realistic sprinkler geometry. Flow visualization revealed strong similarities between the sheet atomization mechanisms in the canonical impinging jet configuration and the sprinkler nozzle configuration. However a space generated stream orthogonal to the tine generated sheet was also

observed through flow visualization and measured to constitute nearly 50% of the overall flow. These two streams followed $We^{-1/3}$ sheet breakup and drop size scaling laws determined from previous impinging jet [38] and sprinkler [2, 3, 13, 19] studies, respectively. Measurements also revealed that the drop sizes created from the space stream are much smaller than those created from the tine generated sheet. The stochastic sprinkler atomization model (SAM) predictions were closer to measurements of the drop size from the tine generated sheet, which is consistent with the basis of the model. The model does not include the space generated stream physics and additional work is currently underway to characterize the atomization mechanisms in this stream in support of SAM development. Measurements are also planned closer to the nozzle exit using a laser based shadowgraphy technique to provide improved unbiased estimates of the distinct drop sizes generated from the space and tine generated streams.

Chapter 4: Atomization and Dispersion Measurements in Fire Sprinkler Sprays

N. Ren, A. Blum, C. Do, and A. W. Marshall

Department of Fire Protection Engineering

University of Maryland, College Park, MD, USA

4.1 Abstract

Water sprays are commonly used in fire suppression applications for cooling the fire environment. This cooling is achieved through the evaporation of droplets (dispersed in the fire gases) and through the wetting of surfaces (from hot or burning materials), inhibiting both the growth and spread of the fire. The suppression performance of these sprays is determined by their ability to penetrate the fire (i.e. the induced flow) to reach burning surfaces below, while dispersing water throughout the hot environment. Spray penetration and dispersion are governed by the initial drop size and velocity characteristics of the spray, which depend on the injection conditions and nozzle configuration. In many fire suppression devices such as sprinklers, a jet is injected onto a deflector to generate the water spray. Although there are many variations on this basic concept, most sprinklers include a central boss surrounded by a deflector having both tines and spaces. In order to study the essential physics of the atomization process, discharge characteristics from simplified nozzles were measured. These measurements were compared with those from a more realistic sprinkler configuration. Flow visualization experiments revealed that the canonical impinging jet configuration produces a radially expanding sheet. While

similar atomization mechanisms were observed, the realistic sprinkler configuration produces a three-dimensional sheet with two distinct flow streams generated by the tines and spaces of the nozzle. Comprehensive experiments were conducted to describe atomization (e.g. sheet break-up locations and initial drop sizes) and dispersion (e.g. volume density and local drop size profiles) in these sprays.

4.2 Introduction

Fire sprinkler systems have been used for more than one hundred years to suppress fires [1]. Compared to other fire suppression systems, sprinklers are inexpensive, reliable, and easy to operate. Those advantages make sprinklers an optimal choice for many fire suppression applications.

The basic suppression mechanisms for water based fire suppression are wetting, cooling, oxygen depletion, and radiation attenuation [64]. The characteristics of the initial spray determine the effectiveness of those mechanisms. For example, small droplets have higher surface to volume ratios, resulting in better cooling, oxygen depletion and radiation attenuation performance. However, the momentum of the smaller drops may be insufficient to penetrate the fire plume. Recognizing the importance of the spray characteristics in fire suppression performance, many spray-focused experiments have been conducted. Although full-scale spray characterization is tedious, it provides invaluable information for sprinkler design and provides a foundation for atomization model development.

The fire sprinkler uses an impinging jet configuration for atomization and dispersion. In these devices, a vertical jet injected onto a deflector forms a radially expanding sheet. Aerodynamic waves grow on the inherently unstable sheet,

eventually causing the sheet to break up into fragments, and ultimately forming drops. Basic features of the atomization process are presented in an illustration shown in Figure 4.1 (a) and in a photograph provided in Figure 4.1 (b).

Several fundamental studies have been conducted focusing on the break-up of unstable expanding sheets. Dombrowski and Johns [26] studied atomization in sheets formed from expanding fan nozzles. They developed an atomization model to predict break-up time and drop size based on stability theory and experimental observations, which showed that the unstable expanding sheet first breaks up into ligaments, and then into drops. Their model and measurements showed the importance of ambient density increases in reducing the drop size. Huang [38] studied the break-up of axisymmetric liquid sheets formed by the impingement of two co-axial jets. His results show that the break-up distance of the sheet is a function of the Weber number, $We = \rho_l U^2 d / \sigma$; however, the relationship between the break-up distance and *We* changes significantly depending on the *We* range. For example, for low $We \leq$ 500 the sheet break-up distance increases linearly with *We*, but for $We > 2000$, the sheet break-up distance decreases following the power law $We^{-1/3}$. Clanet and Villermaux [39] studied the break-up of liquid sheets generated by liquid jets impinging onto a small deflector. They studied sheet break-up using water and ethanol and found results similar to Huang. In addition to their liquid sheet characterization, they found that the droplet mean arithmetic diameter follows the scaling law, $\overline{d} / D_0 = (\rho_{air} / \rho_l)^{-2/3} We^{-1}$ for relatively small *We*, $1{,}000 \leq We \leq 2{,}000$.

Some limited experimental studies involving more complex sprinkler-like geometries have also been conducted. Dundas [13] used a high-seed photographic

and laser shadowing technique to measure drop size distributions from six sprinklers with nozzle diameters ranging from 3.1 – 25.4 mm and with pressures ranging from 0.345 – 5.25 bar. Dundas's research confirmed the correlation first proposed by Heskestad [23] that $d_{v50} / D_0 = CWe^{-1/3}$, where d_{v50} is the volumetric median diameter, D_0 is the orifice diameter, C is a constant depending on sprinkler geometry. Dundas summarized the C value from different researchers showing values in the range $1.74 < C < 3.21$. Detailed sprinkler measurements have also been reported by Yu [2], Prahl and Wendt [9], Widmann [19], and Sheppard [3]. They also verified that drop size can be reasonably correlated with $We^{-1/3}$; however, the respective coefficients vary with sprinkler configuration. On the other hand, Putorti's measurements [20] demonstrated a $We^{-2/3}$ correlation. It was hypothesized that this contrasting behavior resulted from differing atomization mechanisms in Putorti's sprinkler geometry.

In this study, full-scale measurements of discharge characteristics in a canonical sprinkler configuration (i.e. impinging jet) and realistic sprinkler configurations are presented. Short exposure time photographic techniques were used to characterize the break-up process near the injector. The overall flux based drop size distributions were obtained very close to the injectors (between 100 and 400 mm depending on sheet break-up location). Spatially distributed measurements of drop size and volume flux were also performed 1 m below the nozzle. The atomization and dispersion measurements, taken over a wide range of operating conditions, reveal strong correlations governed by the Weber number and the characteristics of the injector geometry.

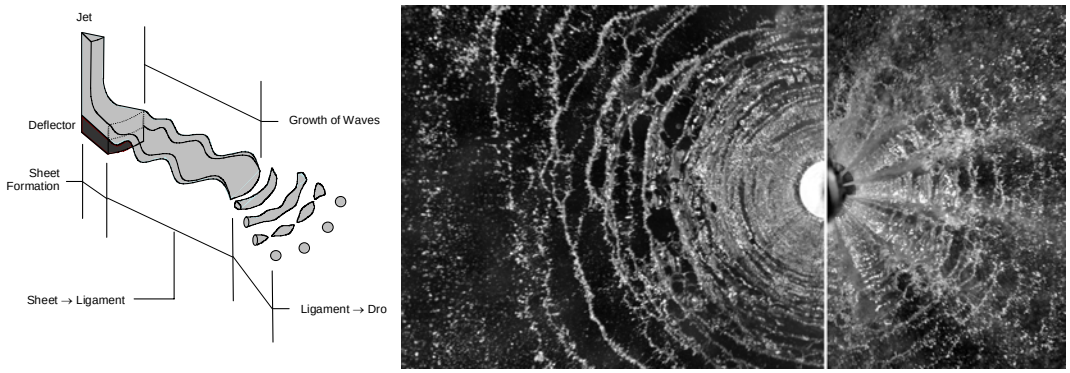

(a) (b)

Figure 4.1 (a) Illustration of the atomization process[21]; (b) Photograph of the atomization process with p = 2.07 bar for a solid deflector nozzle (left) having geometry similar to the nozzle used in this study (right).

4.3 Approach

The break-up process responsible for the initial spray was characterized through several measurements focused on the disintegrating sheets generated by fire sprinklers of varying complexity. These measurements included visualizing sheet topology and quantifying sheet break-up locations. In the more complex configurations, novel experiments were conducted to determine the flow split between the streams generated from the flow along the tines and the streams created from the flow forced through the void spaces between the tines. This measurement is important in determining the stream-wise flow rate and associated stream thickness, which has a primary effect on drop size. The drop size distribution of the overall spray is measured just outside the break-up region using a combined Shadowgraphy and Particle Tracking Velocimetry (PTV) system developed by LaVision GmbH, Sizing Master Shadow [65]. The Shadowgraphy configuration used in this study can measure individual drop size and drop velocity simultaneously with a lower limit on drop size of 0.1mm. Finally, the radial distribution of volume flux was measured with a mechanical patternator 1 m below the sprinkler. The drop size was also measured at

several radial locations (also 1 m below the nozzle) using a Spraytec Particle Analyzer developed by Malvern Instruments, Malvern/INSITEC [66]. The Malvern Spraytec Particle Analyzer can measure drop sizes having distributions ranging between 0.002 to 2mm. To investigate the effect of injection pressures, the experiments were performed at inlet pressures of 0.69, 1.38, 2.07, and 2.76 bar. The effect of nozzle geometry was also explored as described in the following section.

4.3.1 Nozzle Configuration

Two sprinkler configurations were characterized in these experiments representing both canonical and realistic geometries. The Basis Nozzle consists of a separate injector and deflector. The deflector of Basis Nozzle is supported from below. It does not have tines, frame arms, or a boss. This canonical configuration provides a useful baseline for evaluating the impact of additional geometric features on discharge characteristics. A conventional commercially available Tyco D3 nozzle was utilized for the Standard Nozzle adding boss and tine effects. Figure 4.2 shows the geometry of the nozzles used in this study and Table 1 provides the critical dimensions.

4.3.2 Spray Visualization

The slender flow streams generated from the jet impact on the deflector were imaged using Planar Laser Induced Fluorescence (PLIF) to gain insight into the atomization process. The experiments were conducted inside a vented 1.7 m × 1.7 m × 1.9 m chamber illustrated in Figure 4.3 (a). Illumination was provided by a 500 MW, air-cooled, argon ion laser and a 20 face rotating mirror spinning at 20 Hz. The

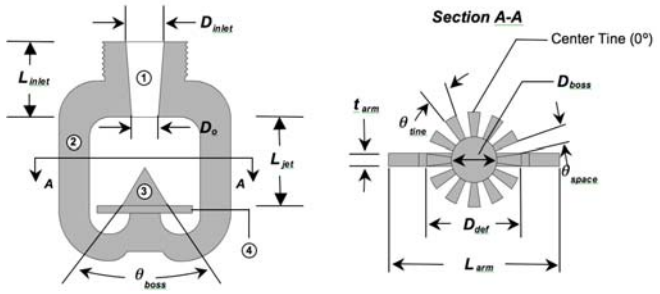

Figure 4.2 The anatomy of a sprinkler; (1) Inlet, (2) Frame Arms, (3) Boss, (4) Deflector.

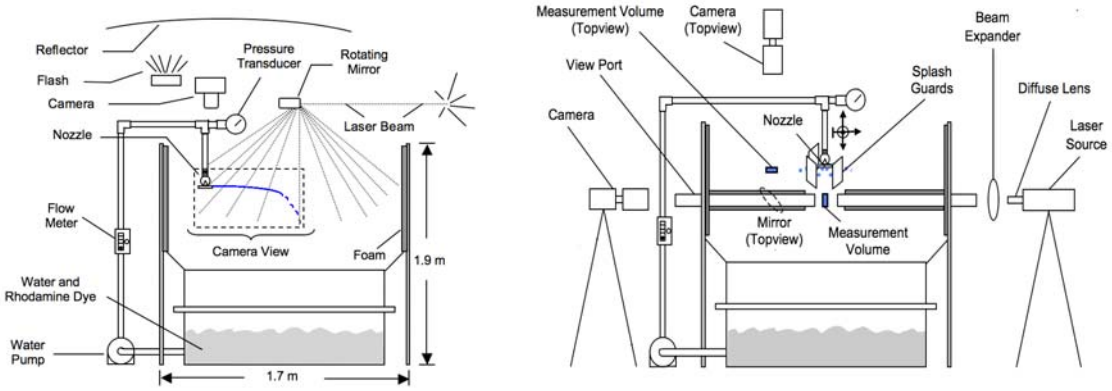

(a) (b)

Figure 4.3 Experimental set-up; (a) Flow visualization; (b) Drop size measurement.

water supply was seeded with a Rhodamine 6G dye having a mass concentration of 0.5 mg/l. The illuminated plane was imaged with a low noise, 16-bit, 2.0 mega-pixel, Cooke SE © high-speed digital video camera fitted with a high pass optical filter operated with an electronic shutter speed of 900 μs at 5 frames per second.

4.3.3 Sheet Break-up

In the sheet break-up experiments, a direct photographic imaging technique was used. As illustrated in Figure 4.3 (a), two Canon EX Series flashes operating with a minimum discharge time of 15.6 μs were synchronized to illuminate the liquid sheet from different angles. A Canon 40D 10.1 MP Digital SLR camera was placed above

the nozzle to capture the sheet break-up process. For each nozzle, 20 images were obtained at each pressure. In each image, break-up locations were determined at 37 equally spaced (2.5°) circumferential stations spanning 90° to provide an adequate sample for breakup statistics.

4.3.4 Initial Drop Size

The initial drop size and velocity are measured using a *LaVison* shadowgraphy-based direct imaging technique, as shown in Figure 4.3 (b). For these measurements, a dual-cavity frequency doubled NdYag laser was used to produce 30 mJ / pulse of 532 nm light. The beam was directed through a 50 mm diffuser and expanded to approximately 200 mm with a Fresnel lens. A 4 MP digital camera fitted with a 50 mm Canon f1.4 lens was aimed at the illumination field and focused approximately 100 mm in front of the Fresnel lens producing a 150 mm square field of view with a depth of field of approximately 28 mm. The spray was directed in front of the illumination field and through the camera's imaging region partially blocking the light received by the camera and producing distinct shadow images of drops. The pulsed laser and camera were synchronized to provide double images of the drops separated by a short time interval (~ 60μs). Spatial calibration and image-processing provides the drop sizes in each image; while, the drop velocities were determined through comparison of drop trajectories obtained from image pairs and the image pair separation time. Two hundred image pairs were obtained providing tens of thousands of drop sizes and velocities at a given imaging station (i.e. 150 × 150 × 28 mm imaging region). The sprinkler was traversed and rotated to sweep out a large hemispherical interrogation region (from multiple imaging stations) extending

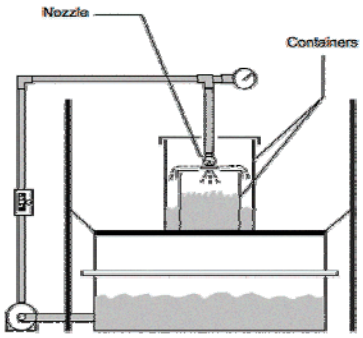

Figure 4.4 Flow-split experimental set-up.

radially between approximately 100 mm and 400 mm. The overall flux based drop size distribution in an integral quantity describing all drops generated by the nozzle independent of the relative location within the spray. The velocity data was used as a weighting function in the overall flux based drop size distribution calculation to remove the spatial bias for drops moving at different velocities [21].

4.3.5 Flow Split

In the sprinkler configurations, the fraction of the flow from the tine and space streams was measured with two containers as shown in Figure 4.4. The small container has a volume of 38 L, which measured the flow from the space. The large container has a volume of 144 L, which measured the flow from the tine. The opening in the lid of the small container was designed to fit the size and shape of the sprinkler deflector exactly, providing complete flow separation between the space and tine streams. Due to the complex flow pattern generated by the multifaceted deflector geometry, the flow rates from the tine and space streams may not be proportional to their respective geometric areas. Determining these flow rates was important for the

atomization analysis because they govern the thickness of the sheets formed from these streams and the size of the drops formed during sheet disintegration.

4.3.6 Volume Density

Knowledge of the volume distribution below the nozzle was critical for the determination of the overall drop size distribution and for evaluating dispersion characteristics. Volume density distributions were obtained over a range of pressures and nozzle geometries using a 2.6 m long mechanical patternator positioned 1 m below the nozzle deflector surface. To permit analysis of the entire sprinkler spray, volume density measurements were conducted inside a large 8.6 m × 7.2 m × 3 m room located at the Maryland Fire Rescue Institute (MFRI) as illustrated in Figure 4.5 (a). The nozzles were discharged for 10 minutes providing a sufficient averaging period to remove effects from short time scale aerodynamic or water supply fluctuations. After verifying the axisymmetry and repeatability of the Basis Nozzle spray, radial volume density distributions were obtained only at the 0º station.

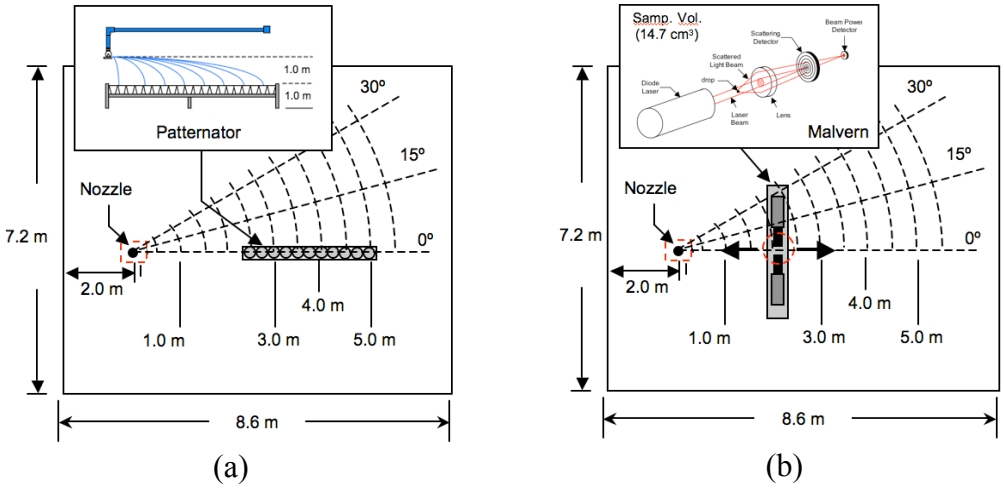

Figure 4.5 Experiment set-up; (a) Volume flux distribution, measured along 0º, 15º and 30º.; (b) Drop size, measured along 0º, 15º and 30º location with a step of 0.5m.

Meanwhile, after verifying axisymmetry in the more complex Standard Nozzle, this nozzle was tested only at the 0º and 15º stations, corresponding to the middle of the center tine and the adjacent space, respectively, as illustrated in Figure 4.5 (a).

A characteristic dispersion length scale, *R*, first introduced by Prahl and Wendt [9], was employed to facilitate analysis of the measurements. This reference quantity provides a maximum radial location that the spray can reach without air friction, and is given by

$$R = (v_o)_r \left(\frac{2h}{g}\right)^{1/2} \left[\left(1 + \frac{(v_o)_z^{\,2}}{2gh}\right)^{1/2} - \left(\frac{(v_o)_z^{\,2}}{2gh}\right)^{1/2} \right], \qquad (4\text{-}1)$$

where *h* is the measurement elevation (below the nozzle), *g* is the gravitational constant, $(v_o)_r$ is the initial radial sheet velocity, and $(v_o)_z$ is the initial vertical sheet velocity. The resulting volume density distributions in the $r^* = r/R$ coordinate describe the relative effect of drag on dispersion. The dimensionless linear density of dispersed volume flow, q_i', is given by

$$q' = \frac{q''}{Q/\pi R^2}\left(2r^*\right), \qquad (4\text{-}2)$$

where q'' is the area volume density (i.e. volume flux) and Q is the nozzle flow rate. The length scale, *R*, was based on the velocities estimated from injection conditions and the measured flow stream trajectories [11]. For the Standard Nozzle at measurements aligned with the spaces (15º station), the *R* determined from the adjacent tined flow stream (0º station) was used to facilitate comparisons between these two streams.

4.3.7 Local Drop Size

Local drop size measurements were also conducted in the large MFRI space to investigate the drop size variations along the radial span of the spray. The local drop sizes were measured over a range of operating pressures and nozzle geometries using a Malvern Instruments Spraytec particle analyzer designed for immersion within the spray. This laser-based instrument employs a light diffraction technique for counting and sizing drops or particles as illustrated in Figure 4.5 (b). Local measurements (probe volume of $10cm^3$) were taken at 12 radial stations starting at 0.5 m and separated by 0.5 m, positioned 1 m below the nozzle. Measurements were taken at each station for 1 minute at 50 Hz providing 300 local drop size distribution realizations. The drop sizes were measured at the same circumferential stations as the volume flux experiments and demonstrated similar axisymmetric behavior. It should be noted that the local drop size distributions obtained from the Malvern are spatially-based measurements calculated by combining instantaneous realizations of drop size distribution within the sampling volume. The velocities of the drops are not measured preventing the calculation of flux-based drop size distributions, such as those obtained for the initial spray.

4.4 Results and Analysis

Atomization and dispersion measurements are reported for the Basis Nozzles and the more complex Standard Nozzles. These measurements provide insight into how the spray is formed in fire sprinklers and provide quantitative information for developing and validating sprinkler spray models.

4.4.1 Atomization Measurements

Planar Laser Induced Fluorescence (PLIF) flow visualization measurements reveal that the spray in the Standard Nozzle is formed from two orthogonal streams as shown in Figure 4.6. The PLIF images were acquired in planes perpendicular to the central tine at three distances from the central axis of the nozzle. In Figure 4.6 (b), the first location (12.7 mm) corresponds to the edge of the deflector showing that the flow traveling along the tine and through the spaces between them. The second location (22.7 mm) shows a tine stream traveling radially outward parallel to the tines and an orthogonal space stream created from the flow forced through the spaces between the tines. Both streams have significantly disintegrated by the time they reach the third location (62.7 mm). The flow split between these streams is important in determining the sheet thickness for the respective streams, which is a key factor governing drop size. Flow split measurements in the Standard Nozzle over a range of pressures revealed that 51% of the flow is directed into the tine stream and 49% of the flow is directed into the space stream. Because the space surface area on the deflector

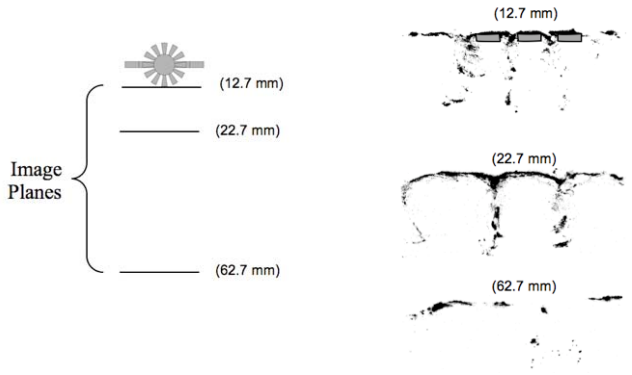

Figure 4.6 Inverted PLIF images depicting flow through sprinkler spaces; (a) Top view of measurement locations; (b) Three-dimensional stream generated with a tined deflector [11].

(33%) is smaller than the tine surface area (67%), the measured flow split will produce a flow bias through the space resulting in a thinner sheet exiting off the tine than that generated with a simple solid deflector.

High-speed flash photography was used to determine sheet break-up locations. Figure 4.7 (a) shows the break-up location distribution of the sheet exiting off the tine for the standard nozzle at 1.4 bar highlighting the stochastic behavior of the break-up process. In Figure 4.7 (b), the average dimensionless sheet break-up location for each experimental condition is presented with respect to the Weber number along with data from Huang [38], who proposed a semi-empirical correlation for his axisymmetric sheets described as

$$r_{bu} / D_0 = 625We^{-1/3}, \tag{4-3}$$

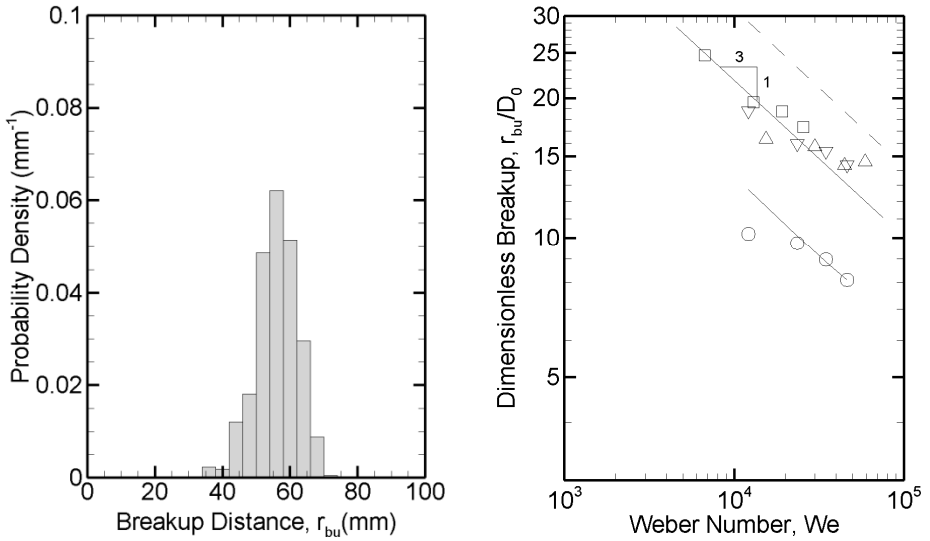

Figure 4.7 Sheet breakup locations; (a) Sheet breakup statistics for Standard Nozzle (D_0=6.4mm, Tine) at 1.38 bar; (b) - - - - Huang Correlation, —— Correlation for basis and standard nozzle, □ Basis Nozzle (D_0=3.5mm), ▽Basis Nozzle (D_0=6.4mm), △Basis Nozzle (D_0=9.7mm), ○Standard Nozzle (D_0=6.4mm, Tine).

The break-up distance of the Basis nozzle for all three orifice diameters correlates well with one another and follows the $We^{-1/3}$ scaling law proposed by Huang. The empirical correlation for the Basis nozzle in this study was determined to be

$$r_{bu} / D_0 = 473 We^{-1/3}, \tag{4-4}$$

which falls below the correlation determined by Huang. This discrepancy could result from the different methods for creating the horizontal, axisymmetric sheets. Huang used two opposed impinging jets to create his radially expanding sheets, while a single jet impinging upon a flat deflector surface was used in this study. Sheets created with the Standard Nozzle break up sooner than that of the Basis Nozzle at a similar orifice diameter. This behavior may result from the flow creating a thinner sheet than expected due to the spaces in the deflector as previously described. Earlier break-up for the Standard Nozzle may also result from three dimensional flow

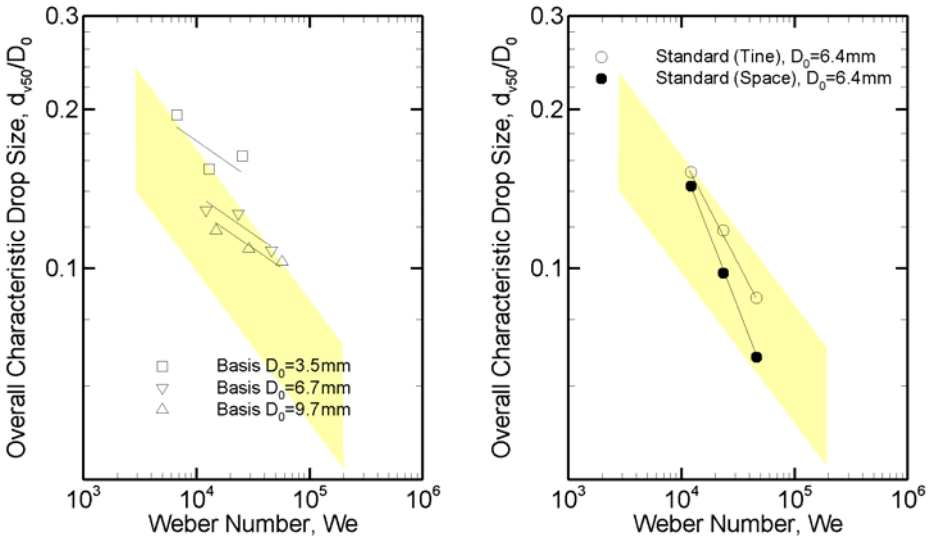

Figure 4.8 Dimensionless Volume Median Diameter (D_{v50}/D_0); (a) □ Basis Nozzle (D_0=3.5mm), ▽Basis Nozzle (D_0=6.4mm), △Basis Nozzle (D_0=9.7mm); (b) ○ Standard Nozzle (D_0=6.4mm, Tine), ● Standard Nozzle (D_0=6.4mm, Space).

disturbances on the radially expanding sheet caused by flow through the space. The break-up data for Standard Nozzle appears to follow the $We^{-1/3}$ at higher pressure conditions, although this trend breaks down at the lowest pressure (0.69 bar).

4.4.2 Drop Size

Overall flux-based drop sizes were determined from shadowgraphy measurements described in § 4.3.4. Figure 4.8 (a) shows that the overall drop size measurements for the Basis Nozzles follow a power law behavior slightly weaker than the highlighted $We^{-1/3}$ region. The highlighted region corresponds to the operating regime for typical sprinklers with $3\times10^3 < We < 2\times10^5$ and $0.06 < d_{v50}/D_0 < 0.2$. In this study, the coefficient of this power law appears to be related to the orifice size. The impact of geometry on the power law coefficient has also been mentioned in previous studies for sprinklers [2, 13, 19, 20, 23]. Figure 4.8 (b) shows the drop size behavior from the more complex Standard Nozzles having a power law behavior stronger than the expected $We^{-1/3}$. It is interesting to note that the thicker tine stream generates distinctly larger drops than the thinner space stream.

The drop size distributions for the Basis and Standard Nozzles appear to follow a Log-Normal Rosin-Rammler distribution described by

$$CVF = \begin{cases} \dfrac{1}{\sqrt{2\pi}} \displaystyle\int_0^d \frac{1}{\sigma d} e^{-\frac{[\ln(d\ /\ d_{v50})]^2}{2\sigma^2}} dd & (d \le d_{v50}) \\ 1 - e^{-0.693\left(\frac{d}{d_{v50}}\right)^{\gamma}} & (d_{v50} < d) \end{cases}, \qquad (4\text{-}5)$$

where γ is a correlation coefficient, $\sigma = 2\left((2\pi)^{1/2}(\ln 2)\gamma\right)^{-1} = 1.15/\gamma$, found empirically. Larger γ corresponds to a narrower drop size distribution. The drop size

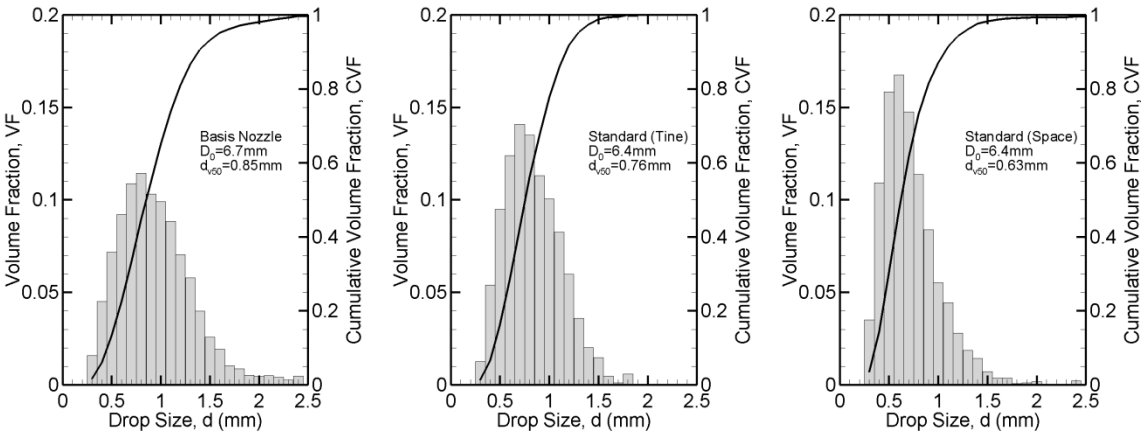

Figure 4.9 Drop size distribution at 1.4 bar; (a) Basis Nozzle (D_0=6.7mm); (b) Standard Nozzle (D_0=6.4mm, Tine); (c) Standard Nozzle (D_0=6.4mm, Space).

is given by, d_{v50}, the volume medium diameter, which is usually used as a characteristic spray drop size. Figure 4.9 shows that the distribution is slightly wider for the Basis Nozzle with γ = 3.0 than for the Standard Nozzles with γ = 3.3 and 3.6 for the tine and space streams respectively. Typically, the Log-Normal Rosin-Rammler distribution follows the actual distribution within 3% in our experiments.

4.4.3 Dispersion Measurements

Results from volume distribution experiments are presented in terms of a dimensionless linear volume density, $q' = (q'' / q''_{avg})(2r')$, and a dimensionless radial location, $r' = r / R$ as shown in Figure 4.10. The Basis Nozzle results presented in Figures 4.10 (a) and (b) demonstrate the effect of increasing the orifice diameter. As the orifice diameter increases the linear density peak shifts radially outwards, indicating more volume is delivered at extreme dimensionless radial locations, reflecting a greater contribution from large drops. In contrast, pressure has a much

smaller effect on the dimensionless volume density distribution as all four experimental pressure condition curves in each graph have similar shape. Comparisons between the Standard Nozzles aligned with the tine (0º station) and

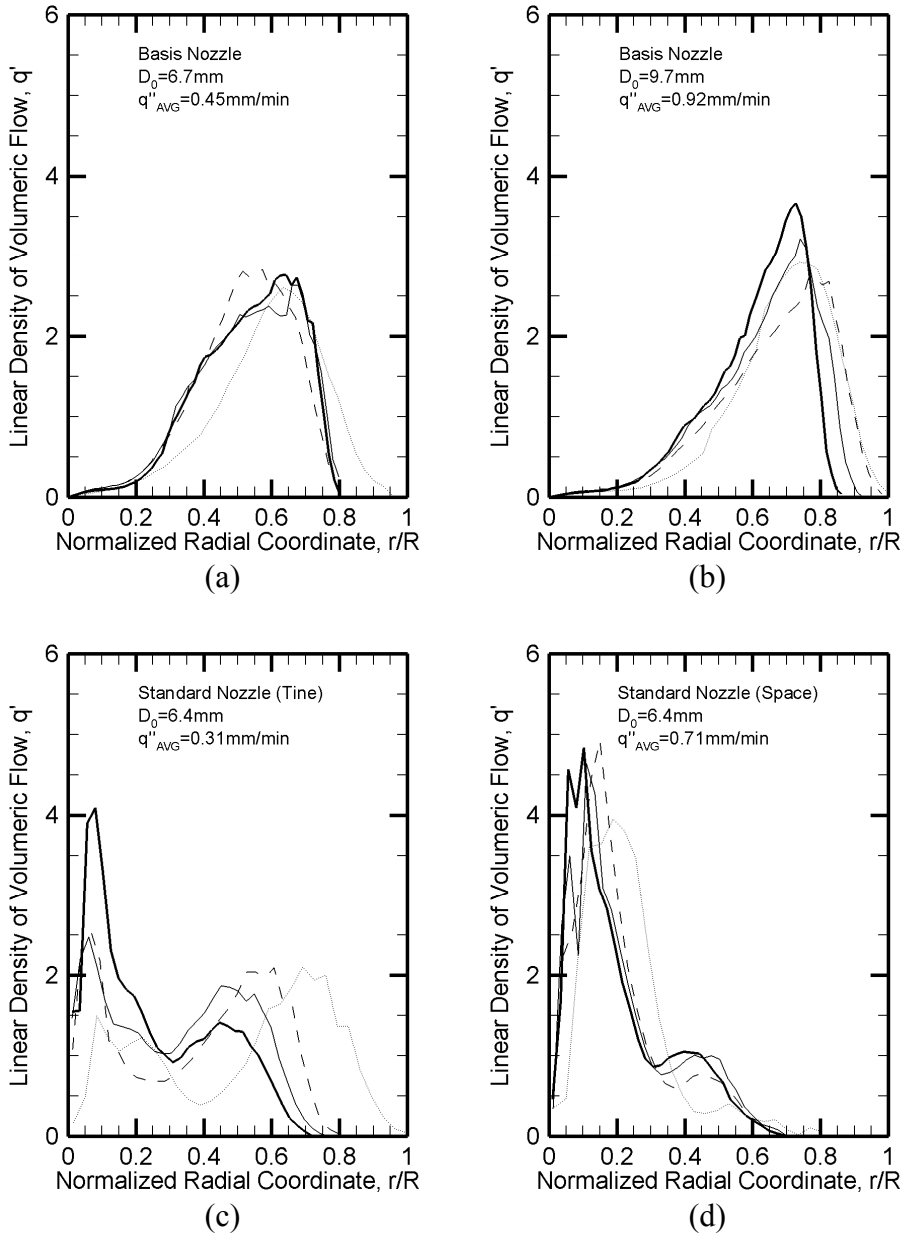

Figure 4.10 Linear Density of Volumeric Flow, ⋯⋯ 0.69 bar, - - - - 1.38 bar, — — 2.07 bar, —— 2.76 bar; (a) Basis Nozzle (D_0=6.4mm); (b) Basis Nozzle (D_0=9.7mm); (c) Standard Nozzle (D_0=6.4mm, Tine); (d) Standard Nozzle (D_0=6.4mm, Space).

space (15º station) are provided in Figures 4.10 (c) and (d), respectively. Comparison of these figures reveal that the more complex geometry of the Standard Nozzle with tines and a boss generate a strikingly different volume distribution pattern when compared to the Basis Nozzle with similar orifice diameter (Figure 4.10 (a)). At both azimuthal measurement locations, Figure 4.10 (c) and (d) show two volume density peaks corresponding to overlapping space and tine streams. Unlike the Basis Nozzle, the volume density of the Standard Nozzle depends significantly on the pressure, especially for measurements aligned with the tine (0º station).

Local spatial-based drop sizes were determined from the Malvern measurements described in § 4.3.7. Local drop size measurements were performed at 0.5 m stations spanning the entire sprinkler spray. Figure 4.11 (a) and (b) shows the local drop size for the Basis Nozzles and Standard Nozzle as a function of dimensionless radial location. As drops initiated near the deflector disperse, they are separated by drag effects in the air resulting in smaller drops traveling shorter distances and larger drops traveling further. The dimensionless location of drops passing through the measurement elevation is thus determined by the size of the drop. It should be noted that the measured local drop size at extreme measurement locations does not continue its increasing trend. The measured peak in local drop size is non-physical, but attributed to limitations of the Malvern instrument, which is only capable of measuring sprays with d_{v50} less than approximately 0.8 mm. Below this limit, the local drop size from the Basis Nozzles over a range of pressures and sizes correlate well with the dimensionless radial location as shown in Figure 4.11 (a). This correlation shows that for a given nozzle configuration, drops of a specific size will

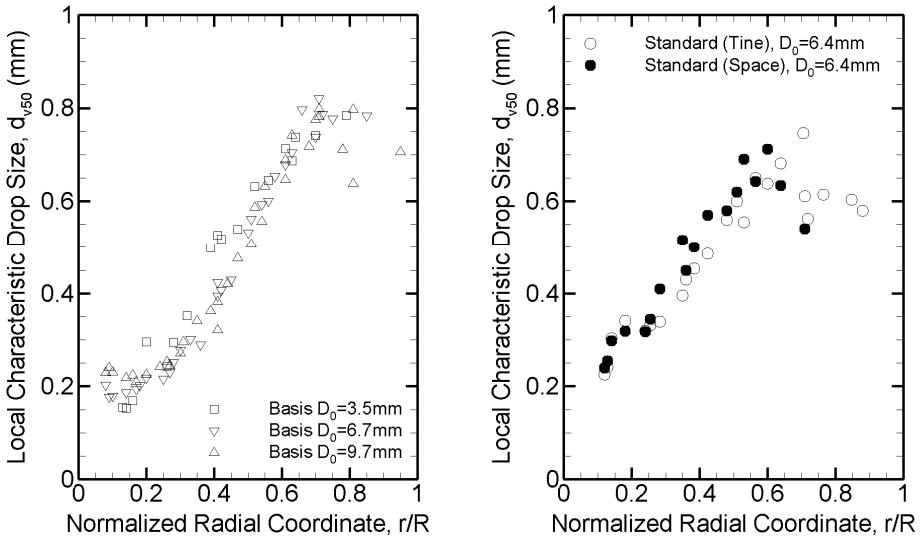

Figure 4.11 Local drop size (dv50); (a) □ Basis Nozzle (D_0=3.5mm), ▽Basis Nozzle (D_0=6.4mm), △Basis Nozzle (D_0=9.7mm); (b) ○Standard Nozzle (D_0=6.4mm, Tine), ● Standard Nozzle (D_0=6.4mm, Space).

travel to a certain *r/R* determined by drag effects and independent of the size of the nozzle and the injection pressure. In other words, the local drop size depends on drag effects, quantified by *r/R*, and the initial drop size and velocity distributions which are determined by the nozzle configuration. A slightly different local drop size profile is generated with the Standard Nozzles as shown in Figure 4.11 (b) with good correlation for the space and tine streams over a range of operating pressures.

4.5 Conclusion

Full scale experiments have been conducted to characterize the initial sprays from a number of nozzle configurations representing simple sprinkler geometries. Sheet break-up scaling laws are consistent with results from previous researchers. The overall drop size of the sprays generated with the Basis Nozzle show slightly weaker *We* dependence than the expected $We^{-1/3}$ scaling law as the pressure is modified, while

the orifice size adjusts the drop size scaling factor. Stronger *We* effects are observed in the Standard Nozzle having more realistic geometric features including tines and a central boss further demonstrating geometry effects on the initial drop size. The boss and tines in the Standard Nozzle completely modify the volume distribution pattern introducing more flow into the central portion of the spray, especially at azimuthal locations aligned with the space (15º station). After non-dimensionalizing the measurement location, the similarity observed in spatial drop size distributions demonstrated that the local drop size is largely governed by drag effects (determined by the initial drop size) with little dependence on pressure and modest dependence on the geometric details of the nozzle. The experimental data provided in this study with a well characterized initial spray should provide valuable information for evaluation of atomization and dispersion models. Future studies will focus on developing scaling laws that include nozzle geometry effects. More detailed near-field measurements of the initial spray including spatially resolved measurements of drop size and velocity are also planned.

Chapter 5: A Comprehensive Methodology for Characterizing Sprinkler Sprays

N. Ren, Howard R. Baum, A. W. Marshall*

Department of Fire Protection Engineering

University of Maryland, College Park, MD, USA

5.1 Abstract

Sprinklers are widely used in fire suppression applications. The suppression performance of these sprays is determined by their ability to penetrate the fire to reach burning surfaces below, while dispersing water throughout the hot fire environment. Spray penetration and dispersion are governed by the initial drop size and velocity characteristics of the spray, which depend on the injection conditions and sprinkler configuration. In this study, the initial spray is fully characterized using a laser-based shadowgraphy and particle tracking velocimetry system producing nearly a million simultaneous drop size/velocity realizations for each sprinkler spray. Near-field spray characteristics are established from local measurements, which are mapped in a spherical coordinate system consistent with the kinematics of the spray. A novel data compression scheme is introduced to generate analytical functions describing the sprinkler spray based on the measurements. These functions are useful for initiating the sprinkler spray in computational fluid dynamics (CFD) based spray dispersion and fire suppression modeling. This framework also reveals physical characteristics of the initial spray not easily recognized from raw data. The near-field spray measurements and associated data compression approach are validated by

comparing volume density measurements 1 m below the sprinkler with volume density predictions generated from spray dispersion calculations initiated with the analytical spray functions.

5.2 Introduction

The function of the sprinkler is to prevent fire growth by effectively dispersing water over a wide area within the fire environment. This dispersion is achieved by breaking a continuous stream of liquid into a spray of discrete drops with wide range of sizes and velocities. While fire suppression sprays control the fire through a number of mechanisms which include wetting, cooling, blowing, oxygen depletion, and radiation attenuation, the primary suppression mechanism for sprinklers is wetting. The performance of sprinklers is determined by their initial spray characteristics and their interaction with the fire. Sprays with large drops readily penetrate the fire plume to wet combustible materials and control fire growth; however, these sprays require a high volumetric flow rate for effective dispersion. Alternatively, sprays with small drops effectively use their volume to generate a large number of drops facilitating dispersion. These small drops also have a high surface to volume ratio for rapid evaporation, reducing fire gas temperatures and associated heat feedback to fuel surfaces. However, small drops easily lose their initial momentum making it difficult to penetrate the fire plume. Optimizing the drop size for fire plume penetration and dispersion is critical for fire suppression performance.

Traditionally, sprinkler performance has been evaluated through testing. However, with the advent of the Fire Dynamics Simulator (FDS) first released in 2000 [62], modeling of fire phenomena with computational fluid dynamics (CFD)

tools is becoming increasingly popular. Some early computational studies [10, 54, 56, 67] focused on studying the interaction between fire plumes and sprinkler sprays; however, without detailed knowledge of initial spray characteristics, dispersion predictions, typically quantified through analysis of volume flux to the floor, is not very satisfying.

Early spray characterization focused on far-field measurements due to diagnostic limitations [2, 13, 23]. Most of these studies focused on volume flux distribution and drop size measurements. The volume flux distribution is a major criterion for sprinkler evaluation, because it shows the ability of a sprinkler to effectively disperse water over the protected area. The volume flux usually has a very high peak directly below the sprinkler, and decreases dramatically when moving radially outwards. Despite this high peak, only a small portion of the overall flow is contained in this centerline area making it relatively unimportant to sprinkler performance. Previous drop size characterization measurements primarily focused on quantifying the volume median diameter, d_{v50}, obtained from drop size distributions in sprinkler sprays. Dundas [13] used a high-seed photographic and laser shadowing technique to measure drop size distributions from six sprinklers with nozzle diameters ranging from 3.1 – 25.4 mm and with pressures ranging from 0.345 – 5.25 bar. Dundas's research confirmed the correlation first proposed by Heskestad [50] that $d_{v50} / D_0 = CWe^{-1/3}$, where D_0 is the orifice diameter and C is a constant depending on sprinkler geometry, We is Weber Number defined as $We = \rho U^2 / \sigma$. Dundas summarized the C value from different researchers showing values in the range $1.74 < C < 3.21$. Detailed sprinkler measurements have also been reported by Yu [2],

Prahl and Wendt [9], Widmann [19], and Sheppard [3]. They also verified that drop size could be reasonably correlated with $We^{-1/3}$; however, the respective coefficients vary with sprinkler configuration.

The overall measured drop size was used to generate sprinkler sprays in early spray dispersion modeling studies. Notable work on sprinkler spray modeling has been conducted by Alpert [54]. Further improvements were performed by Bill [55] and Nam [10]. In their study, the sprinkler spray was introduced by assigning the measured drop size, volume flow rate, discharge speed and discharge angle of 275 trajectories. The trajectories were adjusted manually so that the predicted volume density on the floor would match the experiments. Similar ideas have been incorporated into current CFD tools where the user can map out the initial spray by specifying the local velocity and flux fraction details for arbitrary solid angles. However, tabulating these values for the entire sprinkler spray is prohibitive. Furthermore, the ability to include local drop size information at a given solid angle is required to completely characterize the spray.

In this study, detailed measurements have been conducted near the sprinkler discharge (i.e. the near-field) to characterize the initial sprinkler spray. A comprehensive framework for representing these detailed measurements in a compact format has been established for sprays analysis and modeling. This framework provides the opportunity to establish a high-fidelity spray initiation database (at least for the most popular sprinkler models) useful for widespread and consistent sprinkler dispersion and fire suppression analysis.

5.3 Approach

An ESFR pendent sprinkler with K-factor of 201.5 L/(min·bar$^{1/2}$) and a Tyco D3 spray nozzle with K-factor of 80.6 L/(min·bar$^{1/2}$) were used to generate the unconfined sprays characterized in this study. The deflector in pendent sprinklers is typically divided by spaces and tines with a central boss supported by two frame arms. The ESFR sprinkler has 10 tine and space pairs while the Tyco D3 nozzle has 12 tine and space pairs. It should be noted that the spray is characterized at azimuthal stations bisecting the two frame arms where the effect of 'shadowing' can be neglected. The effect of frame arm 'shadowing' on initial spray and dispersion characteristics is not considered in this study. The drop size and velocity distribution are measured just outside the sheet breakup region using a combined shadowgraphy and particle tracking velocimetry system developed by LaVision GmbH. This system is capable of measuring individual drop sizes and velocities simultaneously with a lower drop size limit of approximately 0.2 mm. The radial distribution of volume flux was also measured with a mechanical patternator placed 1 m below each sprinkler. Comparisons are made between volume flux measurements and dispersion simulations initiated with the measured spray characteristics providing an indirect method for validating the spray initiation approach. The measurements are conducted at injection pressures of 1.4 and 2.8 bar.

The initial drop size and velocity measurement setup are shown in Figure 5.1. For these measurements, a dual-cavity frequency doubled Nd:Yag laser was used to produce 30mJ/pulse of 532 nm light. The beam was directed though a 50 mm diffuser and expanded to approximately 200 mm with a Fresnel lens. A 4MP digital camera

fitted with a 50 mm Canon *f* /1.4 lens was aimed at the illumination field and focused approximately 100 mm in front of the Fresnel lens producing a 150 mm square field of view with a depth of field of approximately 28 mm. The sprinkler spray was directed in front of the illumination field and through the camera's imaging region partially blocking the light received by the camera and producing distinct shadow images of drops. The pulsed laser and camera were synchronized to provide double images of the drops separated by a short time interval (~ 60 μs). Spatial calibration and image-processing provides the drop sizes in each image; while, the drop

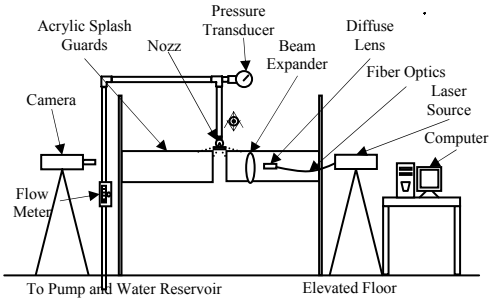

Figure 5.1 Experiment setup

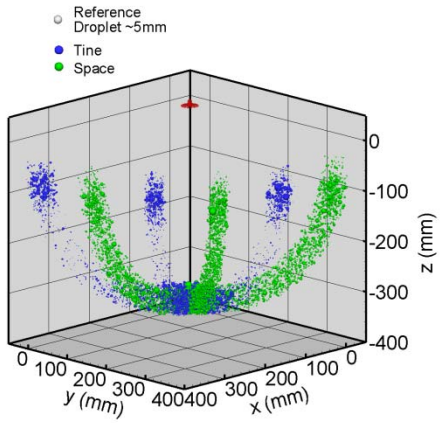

Figure 5.2 Visualization of measured drop sizes and locations on spray initiation sphere (Tyco ESFR sprinkler, 1.1bar)

velocities were determined through comparison of drop trajectories obtained from image pairs and the image pair separation time. Two hundred image pairs were obtained providing hundreds of thousands of simultaneous drop sizes and velocities at a given imaging station (i.e. 150 × 150 × 28 mm imaging region). The sprinkler was traversed and rotated to sweep out a large spherical interrogation region (from multiple imaging stations) extending radially between approximately 100 mm and 400 mm. These imaging stations are azimuthally aligned with the unique tine and space features of the deflector. The measurement regions are rotated about the axis of the sprinkler assuming rotational symmetry and neglecting frame arm effects to visualize the sprinkler spray. Figure 5.2 shows a reconstructed 3-D spherical view of the sprinkler spray based on the shadowgraphy measurements. After individual images and imaging stations are combined, the shadowgraphy measurements produce almost one million drop measurements at each test condition, providing a large sample for reliable statistics.

Volume Density

Radial volume density distributions were obtained using a 6 m long mechanical patternator positioned 1 m below the sprinkler deflector and aligned azimuthally with the distinct tine and space features about the deflector. A characteristic dispersion length scale, R, first introduced by Prahl and Wendt [9], was employed to facilitate analysis of the measurements. This reference quantity provides a maximum radial location that the spray can reach without air friction, and is given by

$$R = U(2h/g)^{1/2}, \tag{5-1}$$

where h is the measurement elevation below the nozzle (i.e. 1 m), g is the gravitational constant, and U is the maximum initial spray velocity. The resulting volume density distributions in the $r^* = r/R$ coordinate describe the relative effect of drag on dispersion. The dimensionless linear density of dispersed volume flow, q', is given by

$$q' = \frac{q''}{Q/\pi R^2}\left(2r^*\right), \tag{5-2}$$

where q'' is the area volume density and Q is the nozzle flow rate. The linear density provides a measure of volume flux weighted by the radius taking into consideration that more volume is captured by the larger area as the radius is increased.

Spray Initiation

These critical quantities for spray initiation are available from stochastic analysis of the measurements. It is daunting to consider the task of characterizing these sprays by tabulating measurements from individual sprinklers at every operating condition. However, a detailed analysis of the measurements reveals that a more compact representation of the initial spray is possible. This compressed formulation facilitates generalization over changes in operating conditions and nozzle geometries.

The initial sprinkler spray can be completely characterized in terms of the following critical quantities; drop location (radius, elevation angle, azimuthal angle), drop velocity, drop diameter, and drop density available from stochastic analysis of the measurements. Although a formidable task, initialization tables for these quantities could be generated for individual sprinklers at various operating conditions; however, a more compact representation of the initial spray provides the framework

for generalized characterization over a range of operating conditions or even nozzle geometries. In this compact representation, only a few physically coherent parameters are required, with experience potentially enabling approximation of spray details even when comprehensive measurements are not available.

Because sprinkler sprays demonstrate highly stochastic behavior, the spray is generated by specifying a number of individual drops determined from stochastic distributions based on experimental measurements of these quantities. Each initial drop is given four properties on a unit sphere, which include azimuthal angle ψ, elevation angle θ, dimensionless drop size, *d*, and dimensionless drop velocity, *u*. The droplets are generated on the surface of a sphere originating from the center of the deflector with radius equal to the initiation distance (typically about 0.35 m to complete spray formation). Analysis of the measurements reveals that drops move radially outward from this origin (i.e. velocity angle determined from position angle) so that only the velocity magnitude requires independent consideration. The spray is completely described in terms of the volume probability density based on solid angle

$$\int_{\theta}\int_{\psi}\int_{u}\int_{d} f_V(\theta,\psi,u,d)d\theta\cdot d\psi\cdot du\cdot dd = 1, \tag{5-3}$$

where the integral represents the complete collection of unique drops accounting for the entire spray volume. The azimuthal angle, ψ, for a drop is determined by randomly choosing an outcome between 0 and 1 and selecting the corresponding ψ according to the cumulative distribution function

$$F_V(\psi') = \int_0^{\psi'} f_V(\psi)d\psi, \tag{5-4}$$

where $f_V(\psi)$ represents the volume probability density in ψ integrated over all elevation angles, drops and velocities described by

$$f_V(\psi) = \int_\theta \int_u \int_d f_V(\theta,\psi,u,d)d\theta \cdot du \cdot dd \ . \tag{5-5}$$

Similarly θ is specified through random selection from the outcome space (ranging between 0 and 1) of the conditional probability cumulative distribution function

$$F_V(\theta \mid \psi') = \int_0^\theta f_V(\dot{\theta} \mid \psi')d\dot{\theta} \ , \tag{5-6}$$

where $f_V(\theta \mid \psi')$ represents the conditional volume probability density in θ at a specific azimuthal station ψ' given by

$$f_V(\theta \mid \psi') = \frac{\int_u \int_d f_V(\theta,\psi',u,d)du \cdot dd}{\int_\theta \int_u \int_d f_V(\theta,\psi',u,d)d\theta \cdot du \cdot dd} \ . \tag{5-7}$$

The local drop size distribution is given by the Cumulative Volume Fraction (CVF), which is

$$F_V(d \mid \theta',\psi') = CVF(d) = \int_0^d f_V(\dot{d} \mid \theta',\psi')d\dot{d} \ . \tag{5-8}$$

The local drop velocity is given by

$$F_V(u \mid \theta',\psi',d') = \int_0^u f_V(\dot{u} \mid \theta',\psi',d')d\dot{u} \ . \tag{5-9}$$

Using the methods previously described, these cumulative functions are employed to determine the size and velocity of the random drop after the location has been assigned. Although unwieldy, the four dimensional probability density, $f_V(\theta,\psi,u,d)$, is available from the nearly one million drop size realizations at each test condition. However, more tractable compressed forms of the important conditional probabilities required for spray generation (i.e. Eqs. 5-4, 5-6, 5-8, 5-9)

have been formulated to gain insight into the spray characteristics and to facilitate CFD integration.

The spray characteristics vary azimuthally because of the periodic tine and space geometry of the sprinkler deflector. These distinct spray characteristics were measured separately in this study. Fourier series were used to create a continuous interpolating function between adjacent space and tine measurements. For example, the continuous interpolated cumulative distribution function for assigning azimuthal location (and corresponding number density) can be generated from

$$\begin{aligned} F_V(\psi) &= A(\psi)F_V(\psi_{Tine}) + \big(1 - A(\psi)\big)F_V(\psi_{Space}) \\ A(\psi) &= \frac{a_0}{2} + \sum_{n=1}^{\infty} a_n \cos\frac{n\pi}{T/2}\psi \end{aligned} . \qquad (5\text{-}10)$$

where T is the angle sum of one tine and one space, a_0 and a_n are Fourier coefficients for a square wave determined from the deflector geometry by integrating over the first tine ($\psi = 0°$) defined as

$$a_n = \frac{2}{T}\int_{-T_{tine}/2}^{T_{tine}/2} \cos\frac{n\pi}{T/2}\psi d\psi . \qquad (5\text{-}11)$$

Typically, three coefficients ($n = 2$) provide a good azimuthal approximation of the measured data. For determining the elevation angle locations, $f_V(\theta \mid \psi')$ is first curve-fit with a Gaussian distribution to capture the typical local peak in the elevation flux profile created by the tine stream. After subtracting this characteristic from the measured data, Legendre polynomial functions are used to curve-fit the remainder. The continuous interpolated cumulative distribution function for locating the elevation angle of random drops (and corresponding density) is given by

$$f_V(\theta \mid \psi') = \frac{f_{v0}}{\sqrt{2\pi}\sigma}\exp\left(-\frac{(\theta-\theta_0)^2}{2\sigma^2}\right) + \sum_{n=0}^{\infty} C_n(\theta)P_n\big(\cos\theta\big), \qquad (5\text{-}12)$$

where f_{v0} is the magnitude of the local volume flux peak, θ_0 is the elevation angle location of the peak (i.e. a characteristic initial trajectory angle), σ characterizes the width of the local peak. P_n are the Legendre polynomials, and C_n are the Legendre polynomial coefficients determined from the experimental data.

Continuous functions for local drop size distribution are created by first generating continuous functions describing the local characteristic drop size, d_{v50}, and distribution width parameter, γ, using Legendre polynomials defined as

$$\begin{aligned} f(d_{v50} \mid \theta', \psi') &= \sum_{n=0}^{\infty} C_n(d_{v50}) P_n(\cos\theta') \\ f(\gamma \mid \theta', \psi') &= \sum_{n=0}^{\infty} C_n(\gamma) P_n(\cos\theta') \end{aligned}, \tag{5-13}$$

Local drop size distributions are generated from these parameters using a combined Log-Normal Rosin-Rammler function

$$CVF(d) = \begin{cases} \dfrac{1}{\sqrt{2\pi}} \int_0^d \dfrac{\gamma / 1.15}{\dot{d}} \exp\left(- \dfrac{\left(\ln(\dot{d} / d_{v50})\right)^2}{2(1.15/\gamma)^2} \right) d\dot{d} & (d < d_{v50}) \\ 1 - \exp\left(-0.693 (d / d_{v50})^{\gamma}\right) & (d > d_{v50}) \end{cases}. \tag{5-14}$$

first suggested by FM Global [10]. Local velocity characteristics can be described with the continuous function. No provision has been included in the current modeling approach to generate local velocity distributions or to generate a local drop size / velocity correlation. This correlation will undoubtedly occur during dispersion due to drag effects. However, it is not clear that a strong drop size / velocity correlation should appear in the near-field (i.e. at spray initiation). Because aerodynamic drag forces have only acted over a very limited time at spray initiation, the simplifying assumption of a characteristic local velocity for all drops at a given location is used.

5.4 Results

Table 5.1 summarizes the compression methodology introduced in the previous section where the measured volume flux distributions, drop size distributions, and velocity distributions (all azimuthally aligned with the space and tine deflector features) are used to generate analytical functions describing the spatial variation of the drop density, size, and velocity with elevation angle. These Legendre polynomials and Gaussian functions are defined through a series of coefficients determined from the detailed measurements. These coefficients provide average values and profile shapes for their respective spray characteristics. Table 5.1 also illustrates the treatment of the azimuthal variation of the spray characteristics using Fourier series with coefficients determined from the nozzle geometry. Transforming the complex stochastic spray into this compact physically accessible framework provides insight into the essential spray features and facilitates quantitative comparisons between sprinklers.

Table 5.1 Spray Initiation Parameters

				Elevation Direction, θ				
				Gaussian			Legendre Polynomials	
							Avg	Shape
Flux / Location		Azimuthal Direction, ψ	Fourier Series a_0, a_n – Deflector Geometry	Tine	f_0	θ_0 σ	C_0	C_n/C_0
				Space	f_0	θ_0 σ	C_0	C_n/C_0
d	d_{v50}			Tine	N/A		C_0	C_n/C_0
				Space			C_0	C_n/C_0
	γ			Tine			C_0	C_n/C_0
				Space			C_0	C_n/C_0
v				Tine			C_0	C_n/C_0
				Space			C_0	C_n/C_0

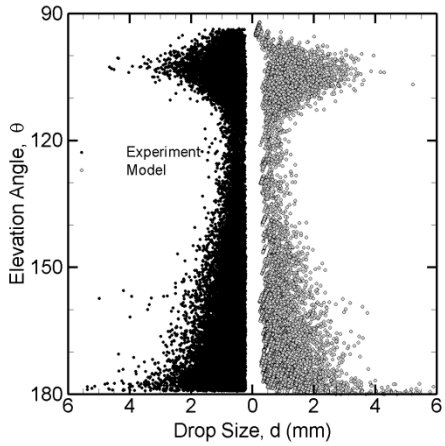

Figure 5.3 Scattered plot comparison between measurement and model at $\psi = 0°$ (Tyco ESFR Sprinkler, 1.1 bar)

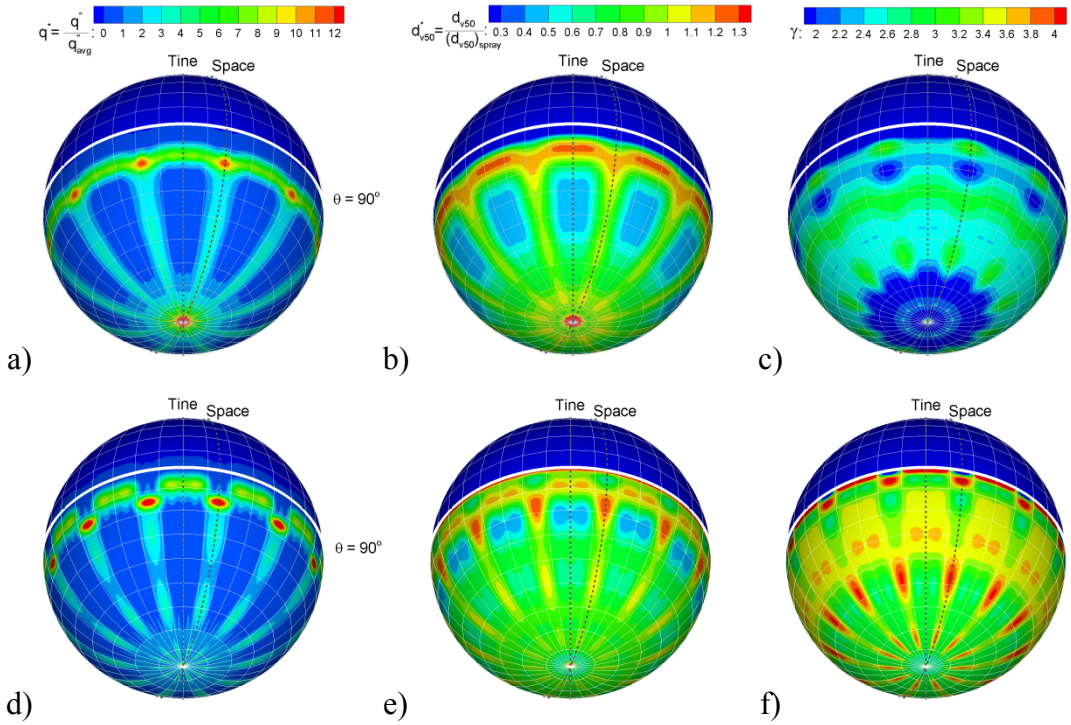

Figure 5.4 Spherical contour maps from analytical expressions; (a-c) Tyco ESFR sprinkler at 1.1 bar; (d-e) Tyco D3 sprinkler at 1.9 bar; (a, d) Flux normalized by average flux; (b, e) Local d_{v50} normalized by overall d_{v50}; (c, f) Local γ

A drop size scatter plot overall elevation angles at an azimuthal location aligned with the tine ($\psi = 0°$) is provided in Figure 5.3. The scatter plot compares measured spray data and spray data generated from the compressed spray description. The analytical expression is capable of generating a spray with details remarkably close to the measurements. This excellent agreement was obtained with $n = 10$ for flux and drop size; however, n as low as 5 also demonstrates good agreement. The analytical expressions also help to quantify the spray characteristics through their parameters. For example, at the tine location of $\psi = 0°$, the spray parameters, $\theta_0 = 110°$, and $\sigma = 3.5°$ and $q_0^* = q_0'' / q_{avg}'' = 8$ describe the spray angle (i.e. peak location), peak width, and peak flux normalized by the average flux at the initiation radius.

Generating the spray with these analytical expressions provides unique insight into the structure of the spray. Figure 5.4 (a-c) shows flux and drop size characteristics for a Tyco ESFR sprinkler at injection pressure of 1.4 bar. The sprinkler is positioned in the center of the unit sphere. The strong variations in flux about the sphere owing to the tine and space geometry are immediately evident. The space stream produces a relatively uniform flux with elevation angle; while the tine stream produces a relatively uniform flux azimuthally. The flux quantity, q^*, describes the local flux normalized by the average flux over the entire unit sphere (i.e. spray initiation radius). Even with this sprinkler geometry optimized to distribute the flow, local fluxes azimuthally aligned with the space and at elevation angles close to the deflector can be over 10 times that of the average flux. Figure 5.4 (b-c) reveal that larger drops are generated from the tine streams at elevation angles close to the

deflector than from the space streams although the width of the local drop size distributions described by gamma is relatively uniform over the unit sphere.

To evaluate the compression scheme further, flux measurements 1 m below the deflector were compared with dispersion predictions initiated with the compressed spray description. The analytical spray was generated in a quiescent air environment and tracked from the initiation location using an in-house model. However, not every drop in the spray is tracked in this approach. Instead, each drop has a coefficient representing a collection of drops with similar properties (i.e. location, drop size, velocity). The coefficient is adjusted to conserve the volumetric flow rate. In each time step Δt, for a group of N drops generated and introduced into the spray at the initiation location, the coefficient of each drop is given by

$$C_N = \frac{Q \cdot \Delta t}{N \cdot \rho \pi/6 \, d_N^3}. \tag{5-15}$$

Drag equations were included to provide one way coupling between the quiescent air and the spray, described by

$$\frac{d\overrightarrow{u_d}}{dt} = \vec{g} - \frac{3}{4}\frac{\rho_{air}}{\rho_l}\frac{C_d}{d}\left(\overrightarrow{u_d} - \overrightarrow{u_{air}}\right)\left|\overrightarrow{u_d} - \overrightarrow{u_{air}}\right|. \tag{5-16}$$

where C_d is the drag coefficient, ρ_{air} is gas density, ρ_l is drop density, u_{air} is gas velocity, u_d is drop velocity. The simplifying assumption of one way coupling is expected to be valid in this momentum dominated region of the spray. To further simplify the spray description, only the zeroth order Legendre polynomial was used to describe the velocity (i.e. average spray velocity). Although higher order descriptions of the spray would capture spatial variations in velocity, the simplifying

assumption of a single characteristic velocity at initiation was explored. Comparisons between the predicted and measured flux distribution are provided in Figure 5.5 (a). The linear density of volumetric flux shows good agreement between the predicted and measured fluxes 1 m below the nozzle revealing not only the accuracy of the compression approach, but also the suitability of the simplified air-drop coupling for particle tracking near the nozzle exit. However more careful coupling may be required further away from the sprinkler.

It is interesting to compare spray characteristics between sprinklers in Figure 5.4 and 5.5. Strong similarities are observed in the shape functions between the large Tyco ESFR sprinkler and the much smaller Tyco D3 nozzle in Figure 5.4. Despite their very different sizes and geometries, both nozzles possess distinct tine and space spray features. The ESFR sprinkler directs more flow downward while the D3 nozzle has higher fluxes near the 'equator'. It should also be noted that the larger values of γ

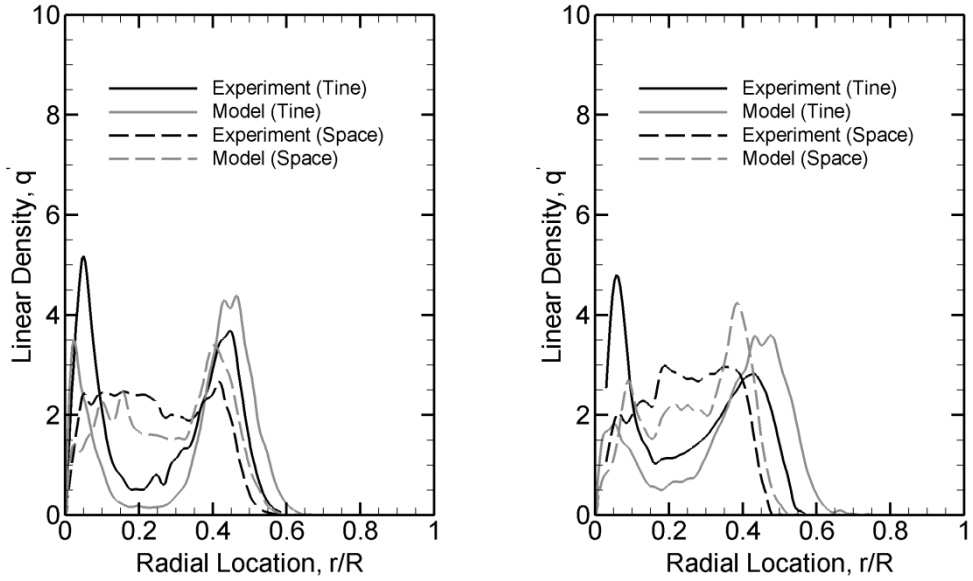

Figure 5.5 Linear Volume density 1 m below the sprinkler; (a) Tyco ESFR Sprinkler, 1.1 bar; (b) Tyco D3 Sprinkler, 1.9 bar

indicate that the drop size distribution is narrower for the D3 nozzle. Figure 5 shows that these similar shape functions at spray initiation produce similar flux profiles 1 m below the nozzle with uniform and double peaked linear densities aligned at locations azimuthally aligned with the spaces and tines, respectively.

5.5 Conclusion

The detailed initial spray measurements performed in this study reveal the strong relationship between the sprinkler geometry and the resulting spray pattern. The measured volume flux and drop size distributions demonstrate strong directional dependence with azimuthal and elevation angles. Correct specification of these quantities is essential for accurate prediction of spray dispersion and volume density distribution at the floor. A framework has been established to compress the extensive initial spray data using compact analytical functions capable of high-fidelity spray generation for CFD integration. The compact formulation of the initial spray is capable of generating sprays, which closely resembles the measurements. Furthermore, dispersion predictions initiated with the analytical functions agree well with volume density measurements obtained 1 m below the sprinklers providing additional validation of both the compact initial spray formulation and detailed spray measurements. Finally, the compact analytical functions reveal strong similarities between initial spray characteristics for different sprinkler geometries. Establishing a sprinkler database within this framework may provide further insight to quantify typical features of these sprays and thus help to remove the widespread uncertainty associated with specifying the initial sprinkler spray in CFD analysis.

Chapter 6: Characterizing the initial spray from large Weber number impinging jets

N. Ren, A. W. Marshall*

Department of Fire Protection Engineering

University of Maryland, College Park, MD, USA

6.1 Abstract

The spray from an expanding and fragmenting liquid sheet formed by orthogonal impact of a jet onto a deflector was explored in this study. Four impinging jet nozzles were characterized with jet Weber numbers ranging from 10^3 to 10^5. The sheet breakup location and spray drop size distributions were quantified under various configurations using short exposure time photography and shadowgraphy techniques. Experimental results confirmed that the breakup distance follows a -1/3 power law with Weber number. However, the drop size behavior was much more complicated, depending not only on the jet Weber number, but also on the free jet length before deflector impact (i.e. distance between orifice and deflector). The free jet length can modify the sheet breakup mode and associated drop sizes. Drop size scaling laws were developed based on injector geometry and injection conditions from the atomization physics to correlate experimental data and explain the effect of sheet breakup mode on drop size distribution.

6.2 Introduction

Atomization studies of expanding liquid streams began in 1883 by Savart [68] who investigated the atomization of round jets in various configurations. By the

1950's and 1960's, Squire [28], Hagerty and Shea [30], Taylor [69, 70], Dombrowski [24, 26] had developed linear stability analyses to predict the sheet breakup and drop sizes including the effects of surface tension force, pressure force, inertia force and viscous force. Dombrowski compared his predictions with experiments conducted with fan spray nozzles, which produced expanding liquid sheet sectors. More recently, Villermaux and Clanet [39, 40] studied atomization of expanding liquid sheets generated by injection of jet onto a flat round deflector. A relatively small deflector was used to minimize viscous boundary layer effects on the sheet. This viscous effect is completely eliminated by forming an expanding sheet with two impinging co-axial jets as described by Huang [38]. These impacting jet configurations have a number of applications such as rocket engine injection, not the least of which is fire sprinklers especially at high Weber number.

The most important factor determines the sheet atomization process is the jet Weber number. Huang's research provides sheet breakup distances over a wide range of Weber numbers which is up to 3×10^4. He found different breakup regimes, in which the sheet breakup distance may increase ($We < 800$) or decreases ($We > 2000$) with Weber number. Recently, Clanet and Villermaux studied those two regimes corresponding to the smooth expanding sheet and the flapping expand sheet respectively. Their experiments confirmed Hunang's results. Furthermore, they provided mean drop size within these two regimes, which also have different scaling laws with Weber number. The Weber range in Clanet and Villermaux's experiments never exceed 2×10^4, with jet diameter less than 5 mm, which is almost the same Weber number range as Huang. In this study, breakup dcharacteristics of the

impacting jet configuration in the high *We* range are explored to gain insight into spray formation in fire sprinklers having similar configuration, albeit with significantly more complex deflector geometries.

Liquird sheet stability theory and modeling have been investigated by only a few researchers including Squire, Hagert, Taylor, and Dombrowski. Squire and Dombrowski's formulated stability equations based on two dimentional waves infinite in the third dimension; while Weihs [37] equations were based on axisymmetric two dimensional waves, properly accounting for thinning of the radially expanding sheet. These complex equations simplified to provide similar results as Dombrowski in the near field. However, far away from the impingement point, the axisymmetric expansion influences the sheet instability by reducing the amplitude of the waves on the sheet. This limitation on wave growth was beautifully illustrated by Crapper et al. [31]. Their photograph shows that if the sheet does not breakup too soon, the wave growth is retarded that the wave amplitude may in fact begin to decrease. However, if the sheet breakup distance is short, the two dimensional linear theory is still valid. In this study, we exploit the linear theory to develop, scaling laws describing the large Weber number spray characteristics, breakup distances and drop size.

6.3 Analysis

The scaling laws for this study are based on combining free surface boundary layer theory first presented by Watson [46] and linear sheet stability analysis introduced by Dombrowski's. A brief illustration of the atomization physics is provided in Figure6.1. An unstable expanding sheet is formatted by impinging a

liquid jet onto a round deflector. This sheet eventually breaks up into small liquid fragments. In the figure, these fragments are assumed to take the form of ring-like ligaments. These ligaments ultimately break up into droplets of various sizes. In his model, sinusoidal waves are assumed for the disturbance, with considering the balance of pressure, surface tension, inertial and viscous forces. When the wave amplitude is small compared to the wavelength, the instability of the expanding sheet can be described by linear stability theory [26], which yields

$$\left(\frac{\partial f}{\partial t}\right)^2 + \frac{\mu}{\rho_l} n^2 \left(\frac{\partial f}{\partial t}\right) - \frac{2(\rho_a n U^2 - \sigma n^2)}{\rho_l T} = 0, \qquad (6\text{-}1)$$

where t is time, f is a dimensionless wave growth defined by $f = \ln(A/A_0)$, A is the wave amplitude and A_0 is initial wave amplitude, μ is the liquid viscosity, T is sheet thickness, n is wave number defined by $n = 2\pi/\lambda$, and λ is wavelength. The first term in Eq. (6-1) is related with inertial force, the second term is related with viscous

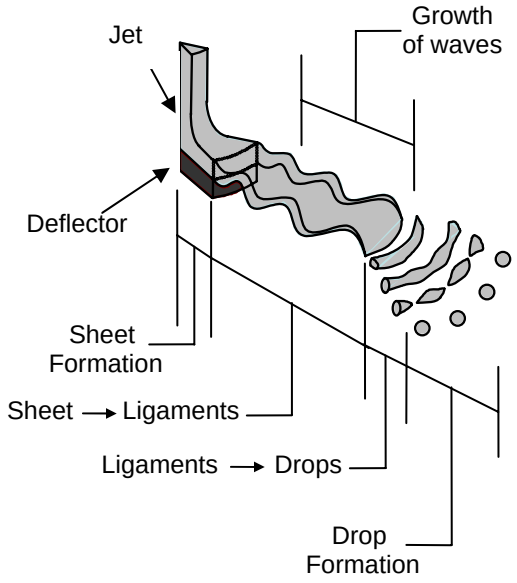

Figure 6.1 Description of atomization process [21]

force and the last two terms are related with pressure force and surface tension force. The wave number and wavelength are arbitrary: however, one specific wave number, referred to as the most unstable wave, will maximum the wave growth rate.

Eq. (6-1) shows that the sheet velocity, *U,* and sheet thickness, *T* are two important parameters governing the wave growth rate. Due to the friction on the deflector, the sheet velocity is not the same as the jet velocity, which in turn will change the sheet thickness. Watson's theory based on free-surface boundary-layer concept was used to estimate the sheet velocity and thickness at the edge of the deflector. In order to show the effect of viscous interaction with the deflector, a non-dimensional sheet thickness is defined as the actual thickness normalized by the inviscid sheet thickness solution, which is given by

$$\beta = \frac{T}{T_0} = \frac{U_{Jet}}{U_{Sheet}}, \tag{6-2}$$

where $T_0 = D_0^{\,2} / 8r$. The sheet thickening factor β is determined by the jet Reynolds number and deflector size, which could be estimated by

$$\beta = \begin{cases} 1 + 0.196\,\mathrm{Re}^{-1/5}\left(\dfrac{r}{D_0}\right)^{9/5} & r < r_l \\ 1.022 + 0.179\,\mathrm{Re}^{-1/4}\left(\dfrac{r}{D_0}\right)^{9/4} & r > r_l \end{cases}. \tag{6-3}$$

where *Re* is the jet Reynolds number and $r_l = 0.183 D_0\,\mathrm{Re}^{1/3}$ is the location where the viscous boundary layer reaches the free surface [46].

The expression for wave number from the viscous dispersion equation is too complex for scale analysis. To facilitate the development of scaling laws, an inviscid model is used. The wave dispersion Eq. (6-1) simplifies to

$$\frac{\partial f}{\partial t} = \left(\frac{2(\rho_a n U_{sheet}{}^2 - \sigma n^2)}{\rho_l T} \right)^{\frac{1}{2}}. \tag{6-5}$$

The wave with the maximum growth rate can be determined from

$\partial(\partial f / \partial t) / \partial n |_{n_{crit}} = 0$, yielding

$$n_{crit} = \frac{\rho_{air} U_{sheet}{}^2}{2\sigma} = \frac{\rho_{air} We}{2\rho_l D_0 \beta^2} = \frac{\rho^* We}{2D_0 \beta^2}. \tag{6-6}$$

where $\rho^* = \rho_{air} / \rho_l$ is the dimensionless density, $We = \rho_l U_{jet}^2 D_0 / \sigma$ is the jet Weber number. The dimensionless wave growth rate leading to breakup is thus given by

$$\frac{\partial f}{\partial t} = \rho^* U_{sheet} \left(\frac{rWe}{2D_0 r_d T_d \beta^2} \right)^{\frac{1}{2}}, \tag{6-7}$$

Recognizing $dr = U_{sheet} dt$, provides spatial growth rate expression

$$\frac{\partial f}{\partial r} = \rho^* \left(\frac{rWe}{2D_0 r_d T_d \beta^2} \right)^{\frac{1}{2}}. \tag{6-9}$$

As the dimensionless amplitude increases to a critical value f_0, the sheet will break. In this study, the critical amplitude is a function of nozzle configuration. Integrating Eq. (6-9) and reformatting yields

$$\frac{r_{bu}^*}{r_d^*} = \left(1 + \frac{3 f_0}{2\rho^* r_d^*} \left(\frac{2 T_d^* \beta^2}{We} \right)^{\frac{1}{2}} \right)^{\frac{2}{3}}. \tag{6-10}$$

where $r_{bu}^* = r_{bu} / D_0$, $r_d^* = r_d / D_0$, $T_d^* = T_d / D_0$, are dimensionless sheet breakup distance, dimensionless deflector radius and dimensionless sheet thickness respectively. Eq. (6-10) shows the break-up distance is a complex function of Weber

number. However, the equation can be simplified if $\frac{3f_0}{2\rho^* r_d^*}\left(\frac{2T_d^*\beta^2}{We}\right)^{\frac{1}{2}} \rangle\rangle 1$, which means the sheet break-up distance is much larger than the radius of the deflector. Under this condition, the dimensionless sheet break-up distance is simplified to

$$\frac{r_{bu}^*}{r_d^*} = \left(\frac{3f_0}{2\rho^* r_d^*}\right)^{2/3} \left(2T_d^*\beta^2\right)^{1/3} (We)^{-1/3}. \tag{6-11}$$

For the same nozzle, the sheet break-up distance would follow $We^{-1/3}$.

Following Dombrowski [26], the diameter of the ligament can be found in terms of the wave number and sheet breakup distance assuming the sheet breaks every half wave length. Because the sheet break-up distance is much larger than the sheet wavelength, the ligament mass can be simplified as

$$\begin{aligned} m_{lig} &= \pi\rho_l T_{bu}[(r_{bu} + \pi / n_{crit})^2 - r^2{}_{bu}] \\ &\approx 2\pi^2 \rho_l T_{bu} r_{bu} / n_{crit} \\ &\approx \pi^2 \rho_l \frac{d^2{}_{lig}}{2} r_{bu} \end{aligned} . \tag{6-12}$$

From Eq. (6-12), the ligament diameter will be

$$d_{lig} \approx 2\left(\frac{T_{bu}}{n_{crit}}\right)^{\frac{1}{2}} = 2\left(\frac{D_0 r_d T_d \beta^2}{r_{bu}\rho^* W_e}\right)^{\frac{1}{2}}, \tag{6-13}$$

The characteristic drop size is proportional to the ligament diameter

$$d = Cd_{lig} = C\frac{\left(D_0 r_d T_d \beta^2\right)^{\frac{1}{2}}}{\left(r_d^{3/2} + \frac{3f_0}{2\rho^*}\left(\frac{2D_0 r_d T_d \beta^2}{We}\right)^{\frac{1}{2}}\right)^{\frac{1}{3}} \left(\rho^* We\right)^{\frac{1}{2}}}. \tag{6-14}$$

The dimensionless form of droplet diameter is

$$d^* = \frac{d}{D_0} = C \frac{\left(T_d^* \beta^2\right)^{\frac{1}{2}}}{\left(1 + \frac{3 f_0}{2 \rho^* r_d^*} \left(\frac{2 T_d^* \beta^2}{We}\right)^{\frac{1}{2}}\right)^{\frac{1}{3}} \left(\rho^* We\right)^{\frac{1}{2}}}. \quad (6\text{-}15)$$

If the break-up distance is much larger than the radius of deflector, the dimensionless droplet diameter is simplified to

$$d^* \approx C\left(\rho^*\right)^{-1/6} \beta \left(f_0 \cdot We\right)^{-1/3}. \quad (6\text{-}16)$$

Eq. (6-16) shows the primary factors that determine the spray characteristic drop size. The spray Weber number is already known as the most important parameter for atomization. The thickening factor β has a linear effect on the drop size and the sheet breakup distance f_0 affect the drop size the same way as Weber number. The coefficient C is a constant number for all nozzles. Due to the stochastic behavior during the atomization process, C can be only determined from the experiments according to which characteristic drop size is used. For d_{v50}, C is approximately 0.9.

6.4 Measurements

The experimental set-up is illustrated in Figure 6.2. A high flow rate pump was used to provide the water supply. To minimize the fluctuation of the pump, a long smooth PVC 40 mm diameter pipe was used to provide a smooth connection with the nozzle. The flow inside this pipe was fully turbulent (max: $Q \sim 160$ lpm, Re $\sim 10^5$). Pressure losses in the section of the pipe downstream from the pressure transducer were accounted for to determine the actual nozzle injection pressure. The nozzle illustrated in Figure 6.3 produce a jet which was injected orthogonally onto a horizontal deflector to create a radially expanding sheet. Both sheet breakup distance

and spray drop size distribution were quantified. The spray formation was visualized using a Canon 40D 10.1 MP Digital SLR camera, placed above the nozzle to capture the sheet break-up process. Two Canon EX Series flashes operating with a minimum discharge time of 15.6 μs were synchronized and bounced off of flash reflectors to illuminate the liquid sheet from different angles.

The sheet breakup distance characterization was conducted using a shadowgraphy based imaging technique as shown with the dashed lines in Figure 6.2. A dual-cavity frequency doubled NdYag laser was used to produce 30 mJ / light pulses at 532 nm. The beam was directed through a 50 mm diffuser and expanded to approximately 200 mm with a Fresnel lens. A 4 MP digital camera fitted with a 50 mm Canon f1.4 lens was aimed at the illumination field and focused approximately 100 mm in front of the Fresnel lens producing a 150 mm square field of view with a depth of field of approximately 28 mm. Spatial calibration and image-processing provides sheet breakup location in each image. Twenty images were obtained for each nozzle at each injection pressure with ten breakup locations picked randomly in the azimuthal direction in each image. Sheet breakup distance statistics were generated from the image analysis.

The drop size measurements were performed using a shadowgraphy technique similar to that of the sheet breakup measurements. However, these measurements were obtained primarily from side view measurements as shown by the laser and optics drawn with solid lines in Figure 6.2. The acrylic splash guard partitions allowed only the desired portion (5 cm thick) of the spray to enter the focal plane of the camera where the shadows of the droplets on the bright background were

captured. The pulsed laser and camera were synchronized to provide double images of the drops separated by a short time interval (~ 60μs). The double pulsed images provided drop size and displacement information useful for determination of the drop velocity using Particle Tracking Velocimetry (PTV). The drop size and velocity information is used to determine flux based drop size statistics. The distance between

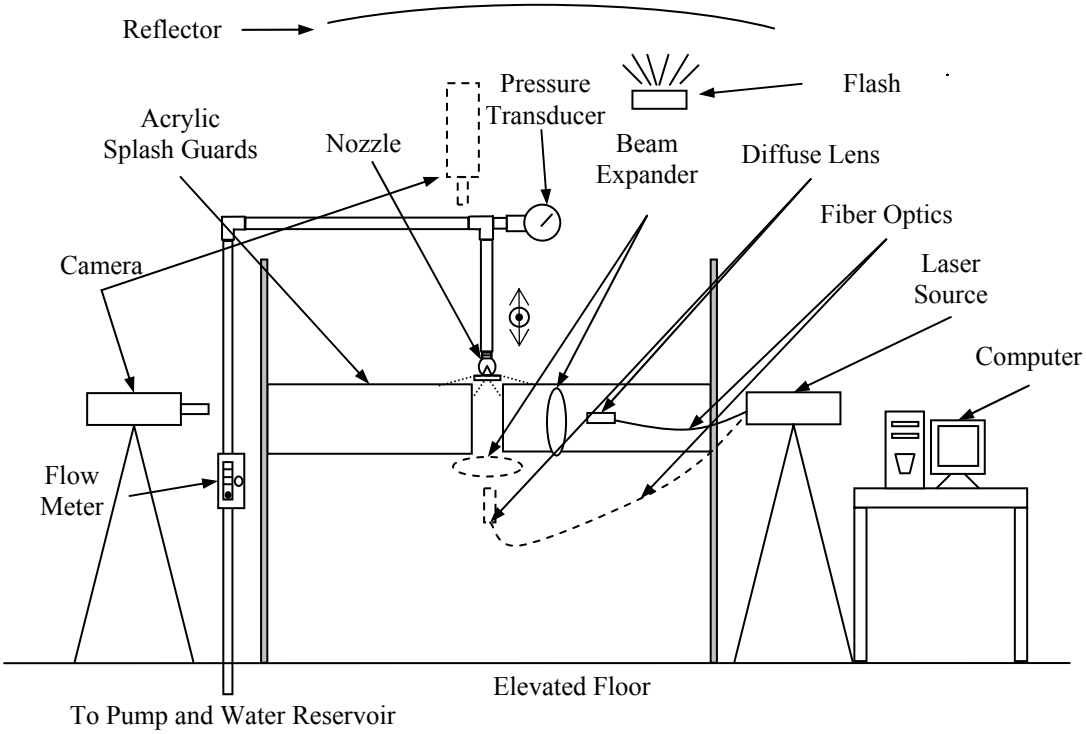

Figure 6.2 Diagram of experimental set-up.

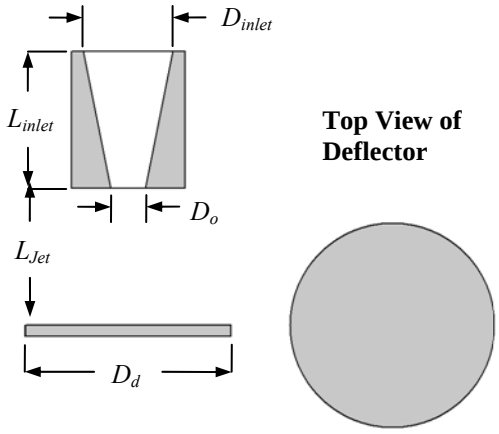

Figure 6.3 The Anatomy of the Nozzle.

the nozzle and measurement locations ranges from 400 mm to 900 mm depends on the nozzle sizes to ensure that breakup is complete so that measurements are obtained on initial sprays that are fully formed.

The drop size measurements have been compared with those in the literature to validate the measurement technique used in this study. The drop size for validation is obtained from top view shadowgraphy images as shown in Figure 6.4. Figure 6.5 shows a comparison between drop size measurements in this study with those performed by Clanet and Villermaux [40]. Although the volume median diameter, d_{v50}, is primarily used in the current analysis, drop size statistics were generated for the arithmetic mean diameter to facilitate comparison. The shadowgraph measurements are in good agreement with those obtained by Clanet and Villermaux showing nearly constant drop size over the *We* measurement range. Unfortunately, measurements below We < 2×10^3 were not practical due to limitations of the water supply and nozzle configurations used in this study.

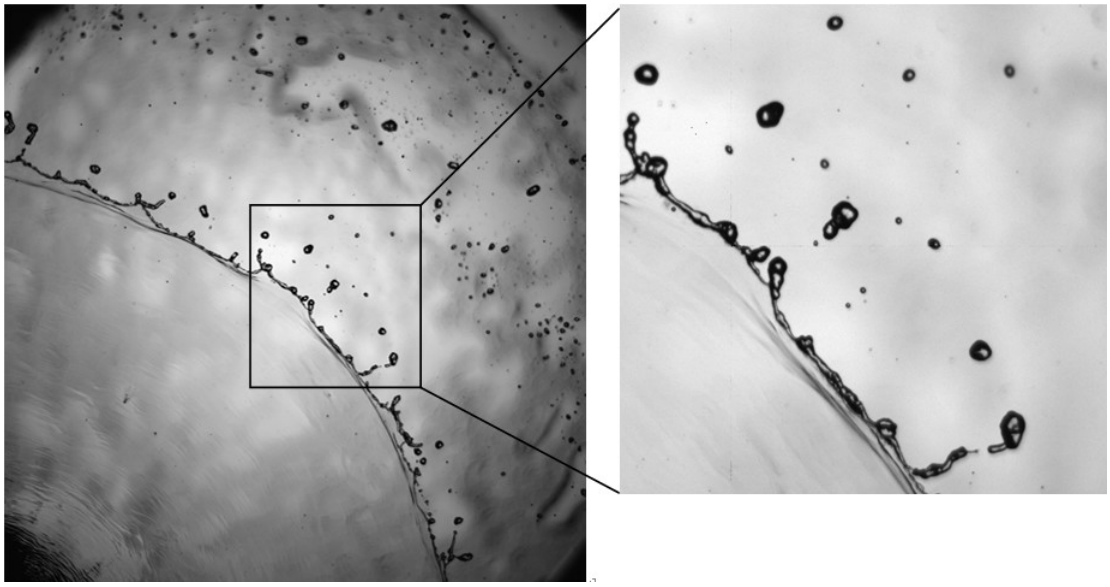

Figure 6.4 Top view shadowgraphy image, B-M nozzle, We=4500.

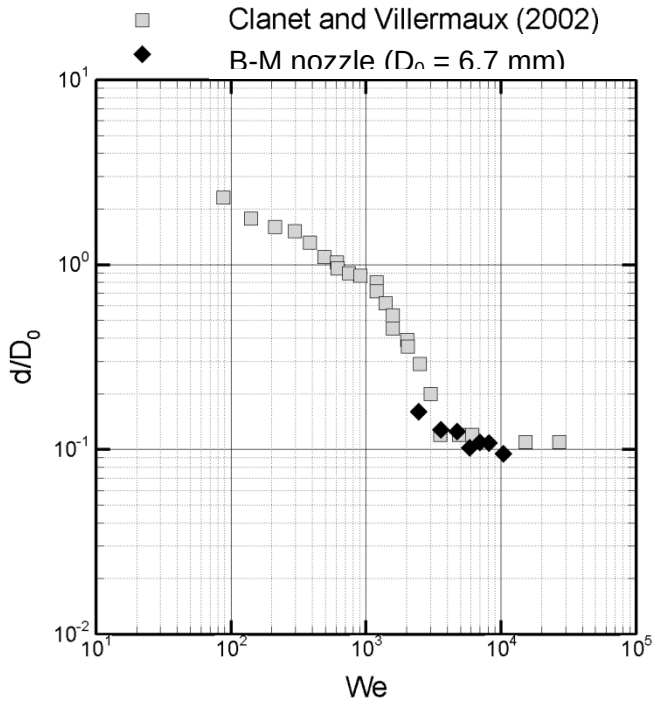

Figure 6.5 Dimensionless arithmetic mean drop size comparison with Clanet and Villermaux.

Four nozzles are used producing jet diameters ranging from 3.5 mm to 12.3 mm. The geometry of the nozzle is shown in Figure 6.3. Two jet lengths (L_{jet}) were tested for each case. The nozzle geometries are detailed in Table. 6.1.

Table 6.1 Nozzle geometry.

Nozzles		B-S	B-M	B-L	B-XL
Nozzle Characteristics	D_{inlet} (mm)	16.5			
	L_{inlet} (mm)	25.4			
	L_{jet} (mm)	25.4 / 76.2			
	D_o (mm)	3.5	6.4	9.7	12.3
	K-Factor (lpm/bar$^{1/2}$)	7.2	25.9	61.9	100.8
Deflector	D_d (mm)	38.0			

6.5 Results

Qualitative discussions of the breakup process will be followed by a description of the different sheet breakup modes. Finally, the characteristic drop sizes of the sprays will be compared with the scaling laws developed from analysis.

6.5.1 Qualitative Results

Basic features of the spray can be observed in the intermediate *We* (7000) and large *We* (15300) spray photographs provided as Figure 6.6 (a), (b) and (c), respectively. In the current study $We < 10^3$ are considered to small; while, $We > 10^4$ are considered large. For these intermediate and large *We* cases, the spray is not smooth with short and long wavelength waves appearing on the sheet. This result is consistent with previous studies that determined that the critical *We* for transition from smooth sheets to flapping sheets occurs at $We = 10^3$. The short wavelengths do not grow considerably in amplitude while the longer waves increase dramatically in amplitude as they progress downstream. In fact, close to the deflector, long waves are hardly visible; while they are easily observed near the edge of the sheet at the breakup location. Figure 6.6 (b) also reveals the presence of small holes appearing on the sheet. Holes close to the breakup location are thought to result mainly from pinching of the locally thin sheet at large wave amplitude. Alternatively, holes close to the deflector are thought to result mainly from random satellite drops floating around the vicinity of the sheet, which may fall infrequently on the sheet triggering premature locally isolated sheet breakup. Figure 6.7 shows side view images of sectors split from the axi-symmetric sheets beginning 150 mm away from the deflector edge. These images also reveal the presence of undulating large amplitude waves and show

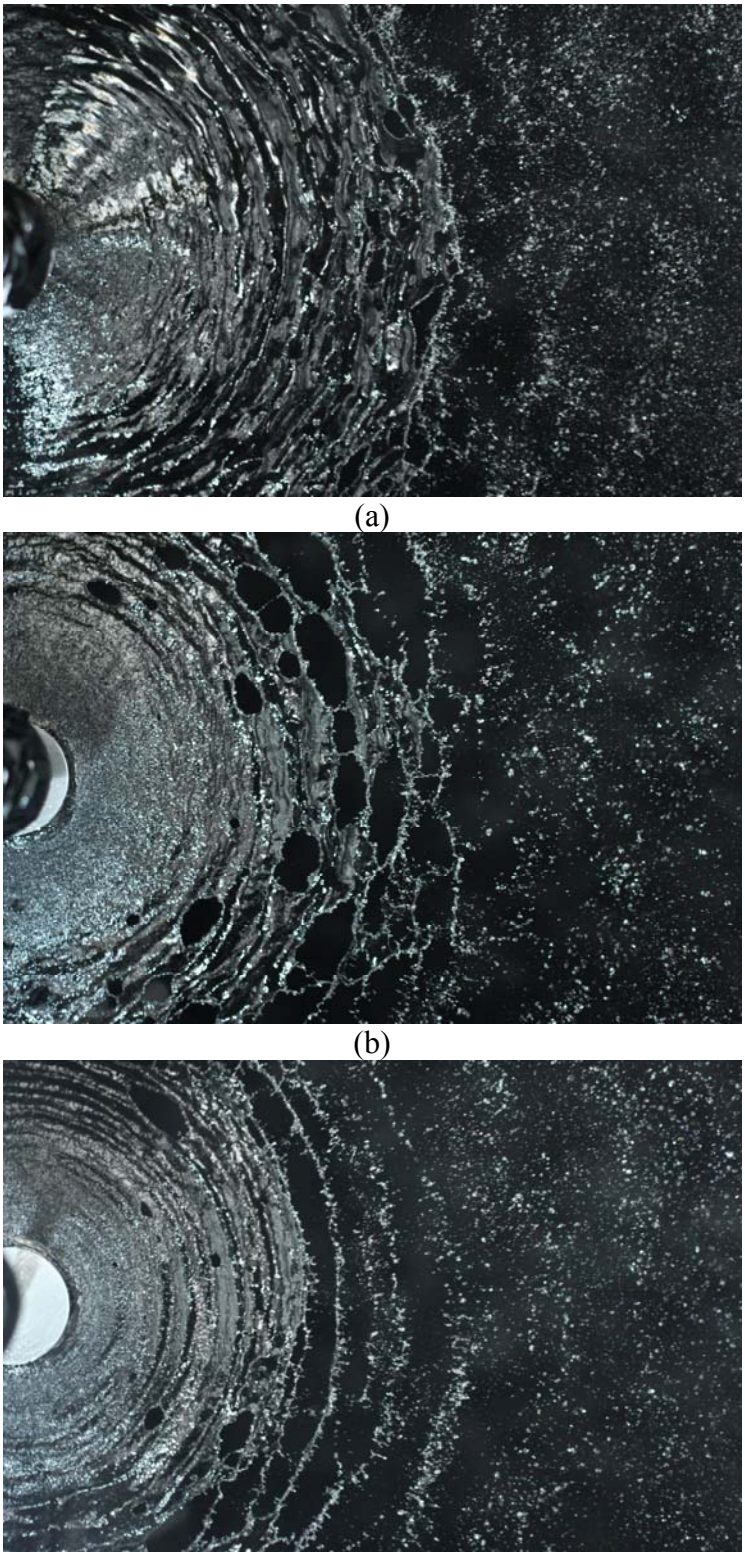

Figure 6.6 Top view photographs of expanding sheets. (a) B-S nozzle, L_{jet}=25.4 mm, We=7000; (b) B-L nozzle, L_{jet}=25.4 mm, We=15300; (c) B-L nozzle, L_{jet}=76.2 mm, We=15300.

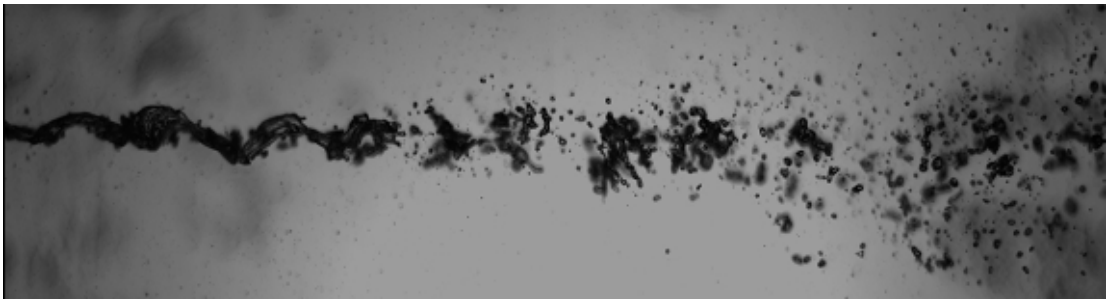

(a)

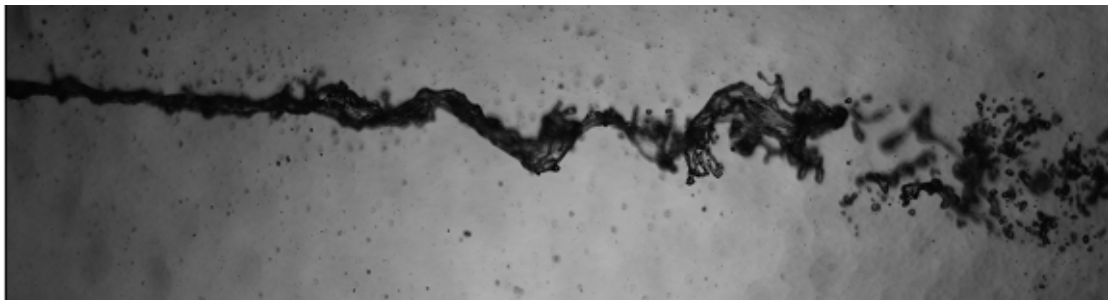

(b)

Figure 6.7 Side view shadowgraphy images of expanding sheets; (a) B-L nozzle, L_{jet}=25.4 mm, We=12300; (b) B-XL nozzle, L_{jet}=25.4 mm, We=15800.

a transition in breakup mode. In Figure 6.4 (a), these waves break up directly into drops. While at slightly higher *We*, the sheet breaks up into fragments with few drops present at the sheet breakup location and the formation of drops is delayed until the fragments disintegrate into drops.

6.5.2 Sheet breakup modes

Huang [38] and others have demonstrated that when $We < 10^3$, the sheet breakup distance increases linearly with *We*; however, when $We > 10^3$ the sheet breakup distance decreases with *We*, following a (-1/3) power law decay. In the current study, additional factors were found to effect sheet breakup behavior. The jet length, L_{jet}, plays an important role in the breakup process as shown in Figure 6.6. For L_{jet} = 25.4 mm, holes are generated at the edge of the sheet for reasons previously described in

Figure 6.6 (b). These holes form fragments that appear to contract into *irregular* ligaments that ultimately breakup into drops. When L_{jet} is increased to 76.2 mm, a noticeable change in the breakup behavior is observed shown in Figure 6.6 (c). The fragmented sheet contracts directly into *regular* ring-like ligaments that disintegrate into drops consistent with Dombrowski's breakup formulation [26].

Recently, Ahmed et al. [43] described breakup behavior in sheets generated with splash nozzles as occurring through Rayleigh-Plateau (R-P) instability or Rayleigh-Taylor (R-T) instabilities. The R-P instability occurs due to surface tension force by minimizing the surface area. The R-T instability occurs due to density difference between two fluids in gravity. As the instability develops, downward-moving irregularities are quickly magnified into sets of inter-penetrating Rayleigh–Taylor fingers. In this case, The R-T instability occurs by the contraction of the liquid sheet. Small finger like ligaments are created at the edge of sheet due to the difference of acceleration rate. This R-P instability is observed at the thick rims that are formed at the slow moving edges of the sheet sectors formed by the splash plates. Alternatively, the R-T instability occurs at the leading edge of the sheet where cusps are formed eventually breaking up into drops. In the current study, the R-T instability is observed clearly in the intermediate *We* regime ($10^3 < We < 10^4$) as shown in Figure 6.6 (a). Drops are formed directly from the sheet despite the presence of large amplitude waves at breakup and no ligaments are formed. As the *We* is increased, the sheet breaks up with holes surrounded by thick rims that coalesce with other holes to form irregular ligaments as described previously in Figure 6.6 (b). Ahmed et al. also observed the coalescing hole behavior using large *Re* instead of large *We* for a regime

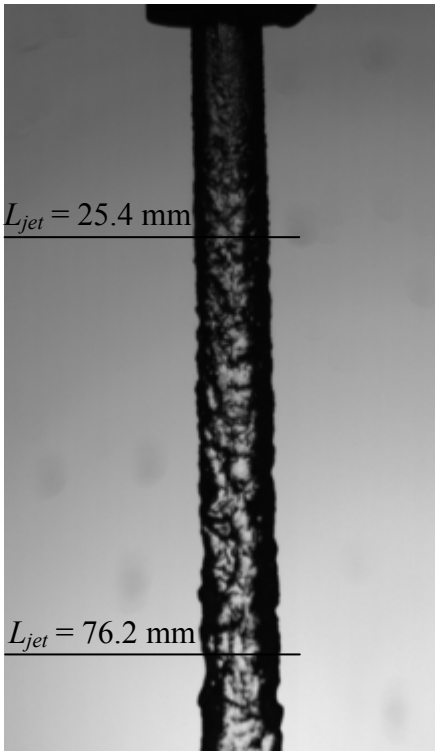

Figure 6.8 Shadowgraphy image of jet, B-L nozzle, We = 15300

criterion; however, they noted that no regular ring-like ligaments were observed due to Kelvin-Helmholtz (K-H) instabilities as first suggested by Dombrowski [26]. In the current study, these distinct ring-like ligaments were in fact observed provided sufficiently large L_{jet} as shown in Figure 6.6 (c). The basis for the importance of L_{jet} is immediately apparent from Figure 6.8. As L_{jet} increases, disturbances have more time to grow before impacting the deflector, producing larger initial sheet disturbances. These larger sheet disturbances reach critical amplitude faster resulting in shorter breakup distances. The associated thicker sheets at breakup may prevent the pinching and associated holes resulting in a more distinct breakup structure.

6.5.3 Scaling Sheet breakup distance and drop size

To better understand sheet breakup distance and drop size behavior, scaling laws developed for sheet breakup distance in Eq. (6-11) and for drop size in Eq. (6-16) should be considered. These equations show that the sheet breakup depends not only on the *We*, but also the critical dimensionless amplitude, f_0, and the sheet thickening factor, β. The critical dimensionless wave amplitude f_0, describes the ratio of the amplitude at breakup to the initial wave amplitude. This parameter can be estimated from the sheet breakup location scaling law from Eq. (6-11) and shown in Figure 6.10. In Dombrowski's analysis [26], f_0 is assumed to be a constant of 12; however, analysis in this study reveals that although f_0 remains constant with changes in injection pressure, the parameter does change with nozzle geometry and is especially sensitive to L_{jet}. Table 6.2 lists the critical f_0 for all the nozzles. For the larger L_{jet}, the critical dimensionless amplitude is smaller consistent with the larger amplitude initial disturbance, reflecting a shorter sheet breakup distances.

Also important in the sheet breakup distance and drop size scaling is the sheet thickening factor due to viscous deceleration of the sheet along the deflector described in Eq. (6-3). In this study, the sheet thickness and associated velocity at the edge of the deflector is not measured. However, the velocity of the drops near the sheet breakup location can be obtained from shadowgraphy measurements in order to

Table 6.2 Dimensionless critical wave amplitude.

f_0	B-S	B-M	B-L	B-XL
L_{jet} (25.4 mm)	8	12	12	10
L_{jet} (76.2 mm)	6	8	6	5

estimate the average sheet velocity for comparison with the theory. For this estimate, the reduction in the sheet velocity due to drag forces is assumed to be small due to the relatively short sheet breakup distance (O [0.1 m]). Figure 6.13 shows the comparison of the theoretical sheet thickening factor with estimates form drop velocity measurements. The sheet thickening effect is important especially for small nozzle (B-S nozzle), which will increase the sheet thickness by 70% above that of the 'frictionless' deflector. For nozzles with large diameter jets, the thickening effect is smaller and decreases slowly with jet Reynolds number. However, the thickening factor has a linear effect on the drop size and should not be ignored especially for large deflectors.

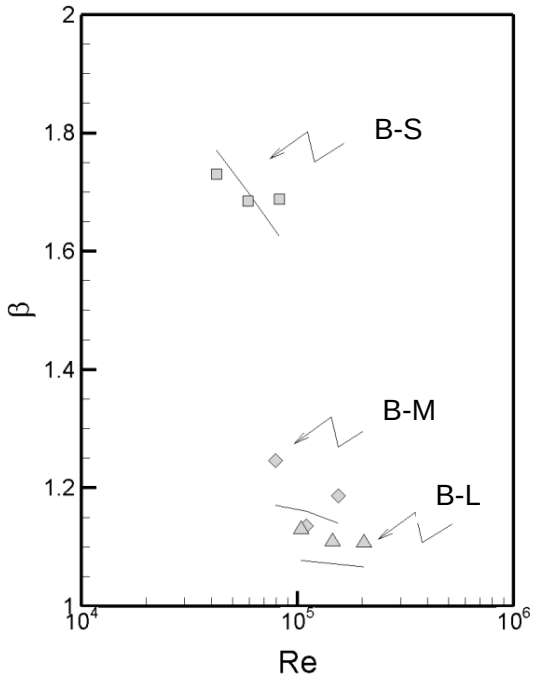

Figure 6.9 Sheet thickening factor at the edge of deflector.

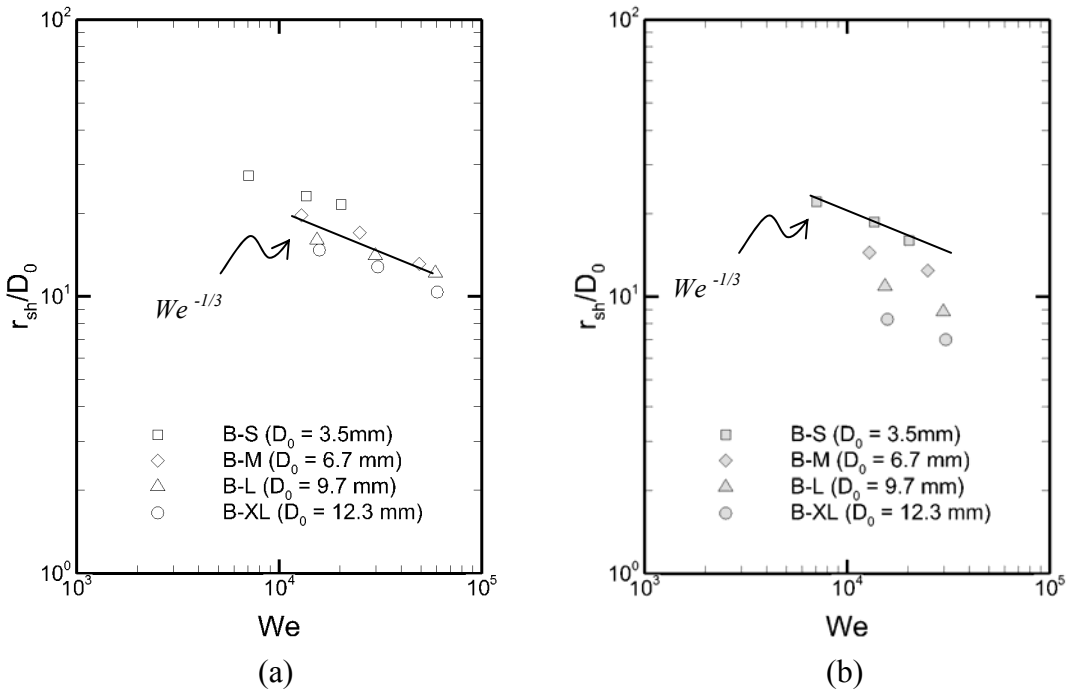

Figure 6.10 Dimensionless sheet breakup distance; (a) L_{jet} = 25.4 mm; (b) L_{jet} = 76.2 mm.

Nozzle geometry effects on sheet breakup distance are shown in Figure 6.10. It is clear that the breakup distance follows a (-1/3) power law decay with *We* for all nozzles. However, as the L_{jet} increases (and f_0 decreases), the sheet breakup distance decreases due to the presence of larger initial disturbances. The importance of β is also clear from this figure when comparing the larger dimensionless breakup distance of the B-S nozzle to that of larger nozzles with significantly smaller sheet thickening factors.

Drop size dependence on *We* is provided in Figure 6.11 for a range of nozzle configurations. For L_{jet} = 25.4 mm, the B-XL nozzle follows a (-1/3) power law with We; however, the smaller nozzles have a weaker *We* dependence. When L_{jet} is increased to 76.2 mm, characteristic drop sizes increase and the *We* number

dependence for all nozzles approach the (-1/3) power law with the exception of the smallest B-S nozzle which appears to maintain its weak *We* dependence following a (-1/6) power law.

After considering the sheet breakup location and sheet thickening effect, the drop size is provided in Figure 6.12 using the scaling law developed in Eq. (6-16). At low d^*, corresponding to high Weber number, the prediction match the experiment well both for small and large L_{jet}. For large d^*, the prediction is much higher than the measurements owing to differences in the breakup modes. As mentioned in the previous section, there three breakup modes were observed in this study, which are

- Rim (Rayleigh-Taylor breakup mode), drops formed directly at the edge of sheet.
- Hole breakup mode, irregular ligaments formed at the location of sheet breakup.
- Ligament breakup mode, ring like ligaments formed at the breakup location.

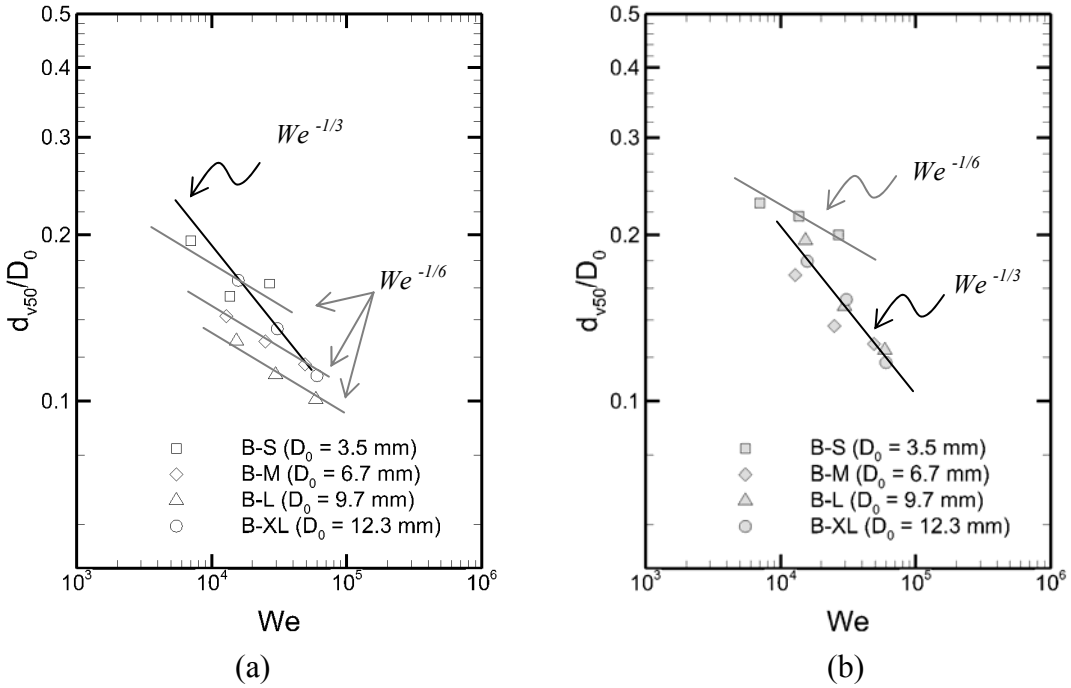

Figure 6.11 Dimensionless d_{v50}; (a) L_{jet} = 25.4 mm; (b) L_{jet} = 76.2 mm.

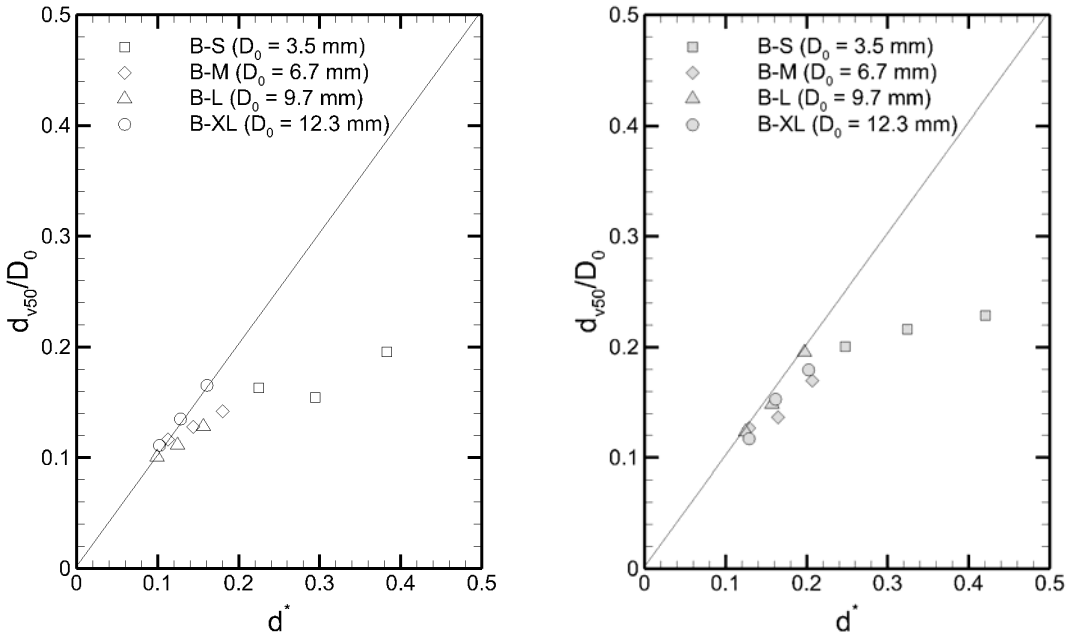

(a) (b)

Figure 6.12 Prediction of dimensionless volume median diameter; (a) L_{jet} = 25.4 mm; (b) L_{jet} = 76.2 mm.

There is a competition between these three breakup modes. When jet Weber number is small, rim breakup mode is more likely to occur. Under this breakup mode, the drop size will be much smaller than the prediction using Dombrowski's model. As the jet Weber number increase, holes are created in the sheet near the edge. Compared to the ligament breakup mode, the total fragment length in the hole breakup mode is longer, leading to a smaller ligament diameter. And the drop size will also be smaller than the ligament breakup mode. In Figure 6.12 (a), the B-M,L nozzles with L_{jet} = 25 mm breakup in this mode and the drop size is smaller than the prediction. In Figure 6.12 (b), the B-M,L,XL nozzles break up in ligament mode and the drop size follows the scaling law very well. Figure 6.12 shows there seems to be a critical d^* = 0.2, above which sheet the sheet breaks up more in rim breakup mode (occurring for the B-S) nozzle and the prediction is not suitable any more.

6.6 Conclusion

Laser based shadowgraphy measurements were performed to quantify the sheet breakup and drop size behavior produced from impinging a jet onto a horizontal round deflector. Effects of nozzle geometry and Weber number were investigated. Three sheet breakup modes (rim, hole, and ligament) were observed during the experiments. Both jet Weber number and jet length determine the sheet breakup mode. Increasing the jet Weber number and/or jet length promotes breakup in the ligament mode. Dimensionless scaling laws based on Dombrowski's linear sheet instability theory were developed including the viscous interaction with the deflector and initial disturbance size. Measurements validate the drop size scaling law when $d^* < 0.2$ corresponding to the high weber number range.

Chapter 7: Summary

A comprehensive study of sprinkler sprays was performed with emphasis of the initial spray characteristics. Several sprinkler geometries were investigated during the tests, ranging from the simplest nozzle (impinging jet onto round deflector, '*ideal sprinkler*') to actual fire sprinklers. The contributions of this research can be categorized into three main areas, which include 1) determination of sprinkler spray formation mechanisms; 2) development of a sprinkler spray scaling laws; 3) development of an analytical sprinkler initiation framework.

7.1 Sprinkler Spray Formation Mechanisms

The spray was visualized from several points of view using powerful imaging techniques. Imaging the spray formation process revealed that the pendent sprinkler sprays have three dimensional structures comprised of horizontal sheets from the flow along the times and vertical sheets from the flow forced through the slots. These sheets generated by the tines and slots have similar behavior to that generated by the 'ideal sprinkler'. The sheet breakup mode from actual sprinkler sprays was found closest to the ligament breakup mode observed in 'ideal sprinkler' sprays.

Imaging the spray formation process also revealed three sheet breakup modes (*rim, hole and ligament breakup modes*) depending on the nozzle geometry, injection pressure as well as the jet length (distance between the nozzle and deflector), which had not been reported before. The sheet breakup modes are found to govern the drop formation with breakup mode determining the drop size scaling law.

7.2 Sprinkler Spray Scaling Laws

Scaling law based on the spray formation physics were developed, which clearly show the drop size behavior under different breakup modes. Sheet breakup distances were demonstrated to follows a -1/3 power law decay with Weber number. Measurements of overall characteristic drop size, d_{v50}, follow a -1/3 power law decay with Weber number for fire sprinklers. However, the drop size for ideal sprinklers shows complex behavior related to the sheet breakup modes. In the ligament breakup mode, the drop size also follows -1/3 power law decay with Weber number. In rim breakup mode, the drop size has a weaker decay (~ -1/6) with Weber number.

7.3 Analytical Sprinkler Spray Initiation Framework

Detailed measurements of the sheet breakup distance, initial spray drop size, and initial velocity measurements were conducted using a laser diagnostic technique based on Shadowgraphy. For drop size measurements, the spray was characterized in the near field (~ 0.3 m from the sprinkler after completion of breakup) along the tine flow and slot flow, respectively. Detailed drop size, velocity and flux profiles were obtained along elevation direction. These spray measurements reveal a strong stochastic behavior with highly non-uniform distributions of drop size, velocity, and drop number around the sprinkler head. An analytical representation of the initial spray characteristics was developed using a combination of Fourier series and Legendre Polynomials to describe the local flux, drop size, and drop velocity distributions. This formulation allows the detailed description of the spray distribution to be compressed into a series of physically meaningful coefficients. The formulation is also easily integrated into CFD codes to provide a detailed

representation of the initial spray. A simple dispersion analysis was performed, accounting only for droplet drag in the quiescent air environment. Prediction of volume density 1 m below the sprinkler head was compared with the measurement with good agreement, further validating measurements and the initiation framework.

Appendices: Shadowgraphy Technique and Data Analysis

The spray was characterized in the near field using Shadowgraphy technique to visualize the droplets. Shadowgraphy is based on high-resolution imaging with pulsed backlight illumination. This idea has been adopted in the early spray measurements, in which the backlight illumination was provided by a high-speed flash in the microsecond order of magnitude [13]. The backlight flash illumination can 'freeze' the droplets and a clear image can be taken by the camera. The quality of the image depends on the resolution of the camera, flash duration and droplet velocity. For higher speed droplets, shorter flash duration is needed to freeze the drop motion. The current backlight is provided by a high-speed dual-pulses laser, being the flash speed set in the nanosecond order of magnitude; this exposure is capable of freezing droplet motion of more than 100m/s. Being Shadowgraphy developed for measuring drop size and velocity simultaneously with high fidelity, it yields more advantages than other traditional spray characterizing techniques, such as Phase Doppler Interferometry (PDI), Phase Doppler Particle Analyzer (PDPA), *Malvern Spraytec*, etc.

A.1 Hardware

The general configuration of a Shadowgraphy apparatus is illustrated in Figure 6.1. The system is developed by *LaVision* with *DaVis* software package [65]. A Nd:YAG laser is used to provide the backlight source. A high-resolution camera is aligned with the backlight and the focal plane is between the camera and the backlight. The initiation of the laser is controlled by the Q-Switch [65] which

normally consists of a polarizer and a Pockels cell crystal driven by high voltage. The laser pulse has duration of few nanoseconds with a Gaussian intensity profile across the beam section. The light released from the laser is infrared with wavelength of 1064nm. The frequency will be doubled by a Second Harmonic Generator (SHG) to convert the infrared to green light with wavelength of 532nm. Approximately, one-third of the energy is available after the light is converted and the power of laser after conversion is about 30mJ per pulse. The time interval between Q-Switch1 and Q-Switch2 controls time interval between the two laser pulses *dt*. The range of *dt* depends on the hardware configuration, with a minimum range determined by the two frame transfer time (~1μs) and maximum range depend on laser and camera frequency (~0.1s). For sprinkler spray, the drop velocity is in the order of 10m/s. *dt* can be set between 50 and 100μs to get an optimal velocity calculation depending on the sprinkler operating pressure.

The laser light is conducted using a 1 m optical fiber to a fluorescence plate diffuser. The diffuser converts the green laser light to an orange bright background. The diameter of the diffuser is 4 cm in the experiments. The size of the diffuser is not sufficiently large to cover wide spray areas and detect a sufficient number of droplets. A Fresnel lens is used to expand the bright background of the diffuser. The shape of the Fresnel lens is a square, with of 22 cm side. The largest bright area obtained in the image is a square of about 17 cm. A 4-Megapixel (2048×2048) Image Pro X Charge Coupled Device (CCD) camera, fitted with a 50mm Canon *f*1.4 lens was used as the image recorder. The resolution of the system depends on the image area recorded. In the current study, the size of effective image area is about 17 cm, corresponding to

0.083mm/pix. Moreover, the smallest droplet can be resolved for a diameter of 5 pixels, which corresponds to a droplet size about 0.21mm. The resolution can be improved by reducing the image area; however, Putorti [20] reported that 98% of the water from typical fire sprinklers consists of droplets larger than 0.2 mm. In order to obtain a maximum imaging area, the current image resolution is kept constant for the entire sprinkler characterization. There are no limits on the maximum drop size, while the traditional measuring techniques show some difficulties in measuring large size droplets, (e.g: *Malvern Spraytec*).

A.2 Drop Sizing and Velocity Algorithm

Detailed drop-sizing and velocity algorithms are provided in the manual of *LaVision* Sizing Master Shadow [65]. A brief introduction on the algorithm may be helpful for parameter setting discussed in following sections.

A drop-sizing algorithm includes few steps as shown in Figure A.1. The first step is to provide a reference background. The reference can be either obtained from a recorded image or calculated from the experimental images. Usually, if the quality of the experimental images is sufficiently good, the background can be used from the recorded image. Otherwise, if the experimental image is blurry or diffused by high-density sprays, the reference image should be determined through a calculation. There are several methods for calculating the reference image, which will be discussed in detail in next section. The next step is to invert the image by subtracting the spray image from the background (reference image). The shadow of the droplet will have higher gray-scale level after the inverting. The following step is called *First Segmentation*. A global threshold is used to detect the drops. The global threshold is

relative to the difference between maximum and minimum intensity of the inverted image. All the areas above the global threshold are isolated for the next step of the analysis. Smaller peaks are usually produced by the background noise or by out of focus droplets and are ignored for further analysis. After the areas above the threshold are isolated, rectangular boxes are set around the isolated areas, which are called "bounding boxes" and defined by AOI (Area of Interested) expansion through a user-defined percentage. A high-level and low-level of thresholds are used to calculate the high-level and low-level drop diameter. The final drop diameter results as the average of these two diameters. If the drop shadow is clear and the intensity profile is sharp, the high-level and low-level diameter will be very close; otherwise, the low-level diameter is larger than the high-level diameter. There are some corrections to be applied after the drop detection. The first one is called *Border Correction*. If the droplet is detected within the image area, the drop size is valid. However, some of the drop shadows may touch the border of the image area. Larger drops show higher chance to touch the border than the smaller drops, thus implying a correction to compensate the large drops. In this study, the imaging area is a square of about 17 cm × 17 cm. The actual area used in the analysis is a square 15 cm × 15 cm. Therefore, all the drops lie inside the image area and border correction is not necessary. However, if the whole image area is used, the border correction should be applied. Another correction is the *Depth of Field Correction*. Large droplets have a larger depth of field than smaller ones. Large drops are more easily detected than smaller drops. The depth-of-field correction compensates the smaller drops, considering their

Image Pre-processing
(Shadow Image Smoothing)

Invert Image
(Reference – Shadowgraph)

Normalize Image
(Reference – Shadowgraph)/Reference

First Segmentation
Global Threshold defined as the percentage between maximum and minimum intensity, for separating the droplets. Then AOI expansion applied for each droplet.

Second Segmentation
Droplets will be separated according to AOI expansion. High level and low level thresholds are used to find the two corresponding drop diameter. The final diameter is the average of these two diameters

Border Correction
Assume the imaging area is W × H, and then each droplet will be weighted with $\frac{W \cdot H}{(W-d)(H-d)}$

Depth of Field Correction
Assume the depth of field for each droplet is *DOF(d)*, and then each droplet will be weighted with $1/DOF(d)$

Velocity Calculation
Droplets on the image pairs are correlated by drop size and allowed shift. To obtain a good velocity calculation, the initial drop shift should be provided as accurate as possible. Then a interrogation window size will be defined helping to find the drop pairs.

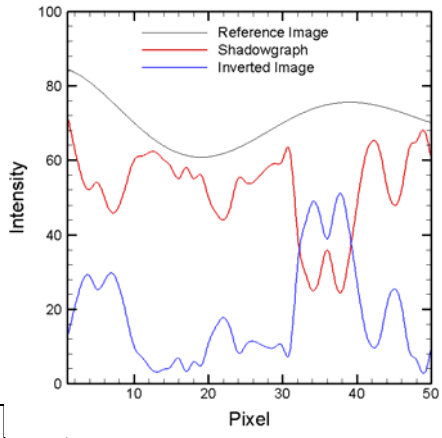

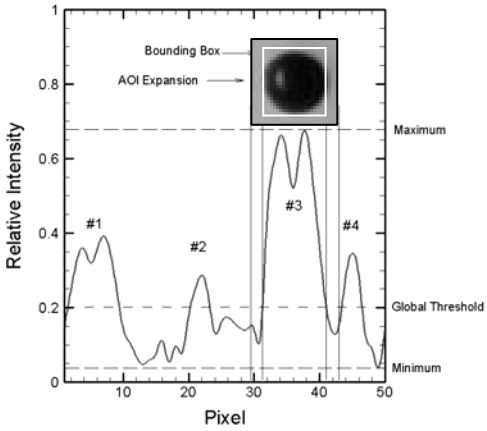

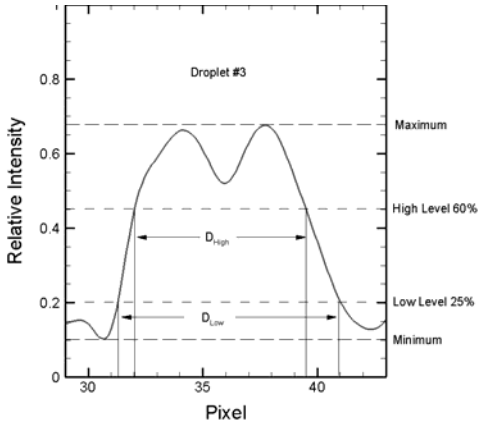

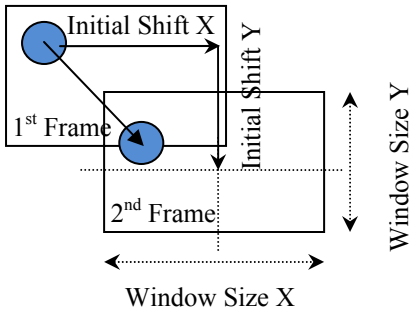

Figure A.1. Shadowgraphy Processing Procedure

smaller depth of field. In this study, the depth of field correction is performed in the post processing analysis.

After the drop sizing has been carried out, the drop velocity is then calculated using the correlation between the image pair. The information of droplet position and size is stored in two separate lists. After all source images have been analyzed, the velocity calculation is realized on the two resulting lists. The drop size and allowed shift are used to identify pairs of drops.

A.3 Parameter Setting for Sprinkler Sprays (Sensitivity Analysis)

There are several options for each parameter in the image-processing procedure. The optimum setting depends on the quality of the image as well as the spray properties, such as drop size, density, velocity, etc. Because there are thousands of images, it is not feasible to process each image by its optimum settings. Actually, finding the optimum setting itself is not easy. In this section, a sensitivity analysis is performed to investigate the effects of parameter setting on the statistical results. A group of suggested parameters is provided, which can be applied to all possible scenarios of sprinkler sprays to obtain good statistical results. Most notably:

- Imaging Pre-processing
  - No smoothing
  - 3 × 3 average
  - 3 × 3 median
  - 3 × 3 peak filter
  - Subtract minimum
- Reference Image Calculation

- Sliding maximum filter
    - Filter length for (Sliding) maximum filter
- Strict sliding maximum filter
- Real maximum filter
- Maximum of each source image

- Reference
    - Ignore areas with less than (x%) of maximum intensity
    - Normalize images by reference image
- Global Threshold
- Particle Segmentation
    - Low level threshold
    - High level threshold
    - AOI expansion
- Recognition Filter
    - Maximum low level area = (x%) of high level area
    - Minimum area
    - Maximum area
    - Height & Width
    - Minimum centricity
    - Remove particles touching the image border
- Interrogation Windows
    - Initial windows size (X, Y)
    - Final windows size (X, Y)

- Pass & Decrease size
- Diameter deviation
- Initial Shift

- Statistical and Output Parameters
  - Apply border correction
  - Apply depth of field correction
  - Ignore diameter (below/above)

In the image pre-processing section, the source shadowgraph image is processed to improve the quality of the source image. The option of *no smoothing* means to skip the pre-processing procedure. If the quality of the source image is good, this option may be chosen. The option of *3 × 3 average, 3 × 3 median* and *3 × 3 peak filter* are used to reduce the noise in the source image. In order to use *3 × 3 peak filter*, a threshold for peak filter must be provided, which is not easy to be applied to all the scenarios. Thus, *3 × 3 peak filter* option is ignored in the present analysis. In order to apply the *3 × 3 average, 3 × 3 median* option, it is better to also select *subtract the minimum* option when the shadow of the drops are not completely black. In the *reference image calculation* option, the first two options are more suitable for sprinkler sprays, and the last two options are not discussed. *The filter length for sliding maximum filter* should be 1.5 times bigger than the largest droplet. In sprinkler sprays, the stable droplet never exceeds 6 mm, corresponding to 72 pixels. Therefore, *the sliding maximum filter* is set at 150 pixels, in case of some large unstable ligaments. For the reference section, it is better to use the option of *normalize image by reference image*, which is useful to recognize droplets in the dark area. The global

threshold is very important for the first segmentation. High threshold only recognizes fewer droplets with clear shadow, while low threshold recognizes more droplets with the possibility to misconceive background noise as drops. The optimum global threshold will be discussed in detail. The *low level threshold*, *high level threshold* and *AOI expansion* are used in second segmentation. The combination of these three setting together with the option of *maximum low level area/high level area* can be used to filter out some undesired drops. A proper choice of these parameters may yield to good statistical results. The *minimum/maximum area*, and *height/width* option is kept unchecked, because those options will be included in the post-processing analysis discussed in next section. The option of *remove particles touching the image border* is not important in this study, as already emphasized. If the imaging area comparable to the drop size, this option should be carefully selected together with the option *apply border correction*. The shape of a small droplet is closer to a circle than a large droplet. The *minimum centricity* option is used to filter out large droplet with distorted shapes. This option can also be used to filter out large ligaments, which haven't totally breakup into droplets. In order to get good results on velocity calculation, the time difference, *dt*, between the two image frames should be correctly set during the experiment. Basically, a large droplet shift increases the accuracy of the velocity measurement. The minimum shift should be at least 3 pixels and about half the size of the smallest particle to avoid ambiguities during velocity calculation. This setting also depends on the droplet density. Low-density sprays may allow larger droplet shifts. For high-density sprays, a large droplet shift may give rise to difficulties in finding the correct droplet pairs. In the sprinkler spray measurements, a

possible droplet shift can be about 1 ~ 2 mm, corresponding to 13 ~ 25 pixels. The typical spray velocity is in the order of 10 m/s, allowing a *dt* of 100 ~ 200 μs. For the velocity calculation, the initial shift can be estimated by $U_{jet} \cdot dt$. The initial window size can be estimated also by $U_{jet} \cdot dt$. The option of *pass* and *decrease size* can be set as 2 and 1.5 respectively, which works fine for most of the spray scenarios. Basically, low spray densities and small image areas result in better velocity calculation. In this study, the image area compared to the drop size is very big. Small droplets usually have low velocity magnitude. Thus, in the velocity calculations, small droplets may be represented by "bad" vectors (i.e.: large amplitude and random direction). Those vectors are filtered out in the post-processing analysis. Because small drops only carry a tiny portion of the total flux, those removed small droplets do not affect the total spray distribution. The experiments in this study show that almost all the large droplets have good velocity vectors.

Only the important parameters are used in the sensitivity analysis. A test matrix is provided in Table A.1. During the analysis, some parameters work better than others and they are tested more frequently. The drop segmentation is the focus of the study. Eight parameters are analyzed, and the last two columns of the table are the results with valid recognized drop number and d_{v50}. Four representative images are used in the sensitivity analysis. Those four sets of image pairs represent different image quality summarized in Figure A.2. The last row of the table provides a suggested parameter setting, which works for all the images and has been used for the final data processing.

Table A.1 Test Matrix for Parameter Sensitivity Analysis (drop size and drop number refer to Image (a) in Figure A.2)

Pre-Processing	Reference	Global threshold	Low threshold	High threshold	AOI expansion	Max. Low Area	Centricity	Drop Number	d_{v50} *(mm)*
No smoothing	Strict Sliding Maximum	50%	40%	60%	50%	150%	50%	716	3.12
3x3 average	Strict Sliding Maximum	50%	40%	60%	50%	150%	50%	547	3.09
3x3 median	Strict Sliding Maximum	50%	40%	60%	50%	150%	50%	706	3.08
No smoothing	Sliding maximum	50%	40%	60%	50%	150%	50%	658	3.05
3x3 average	Sliding maximum	50%	40%	60%	50%	150%	50%	548	3.09
3x3 median	Sliding maximum	50%	40%	60%	50%	150%	50%	653	3.05
No smoothing	Strict Sliding Maximum	30%	40%	60%	50%	150%	50%	710	3.18
3x3 average	Strict Sliding Maximum	30%	40%	60%	50%	150%	50%	508	3.26
3x3 median	Strict Sliding Maximum	30%	40%	60%	50%	150%	50%	733	3.17
No smoothing	Strict Sliding Maximum	70%	40%	60%	50%	150%	50%	517	3.10
3x3 average	Strict Sliding Maximum	70%	40%	60%	50%	150%	50%	476	3.10
3x3 median	Strict Sliding Maximum	70%	40%	60%	50%	150%	50%	531	3.09
3x3 median	Strict Sliding Maximum	50%	30%	70%	50%	150%	50%	110	3.66
3x3 median	Strict Sliding Maximum	50%	30%	70%	50%	200%	50%	528	3.29
3x3 median	Strict Sliding Maximum	50%	40%	60%	20%	150%	50%	858	3.09
3x3 median	Strict Sliding Maximum	50%	40%	60%	50%	150%	60%	653	2.77
3x3 median	Strict Sliding Maximum	50%	40%	60%	50%	150%	40%	728	3.11
3x3 median	Strict Sliding Maximum	40%	40%	60%	30%	150%	40%	878	3.12

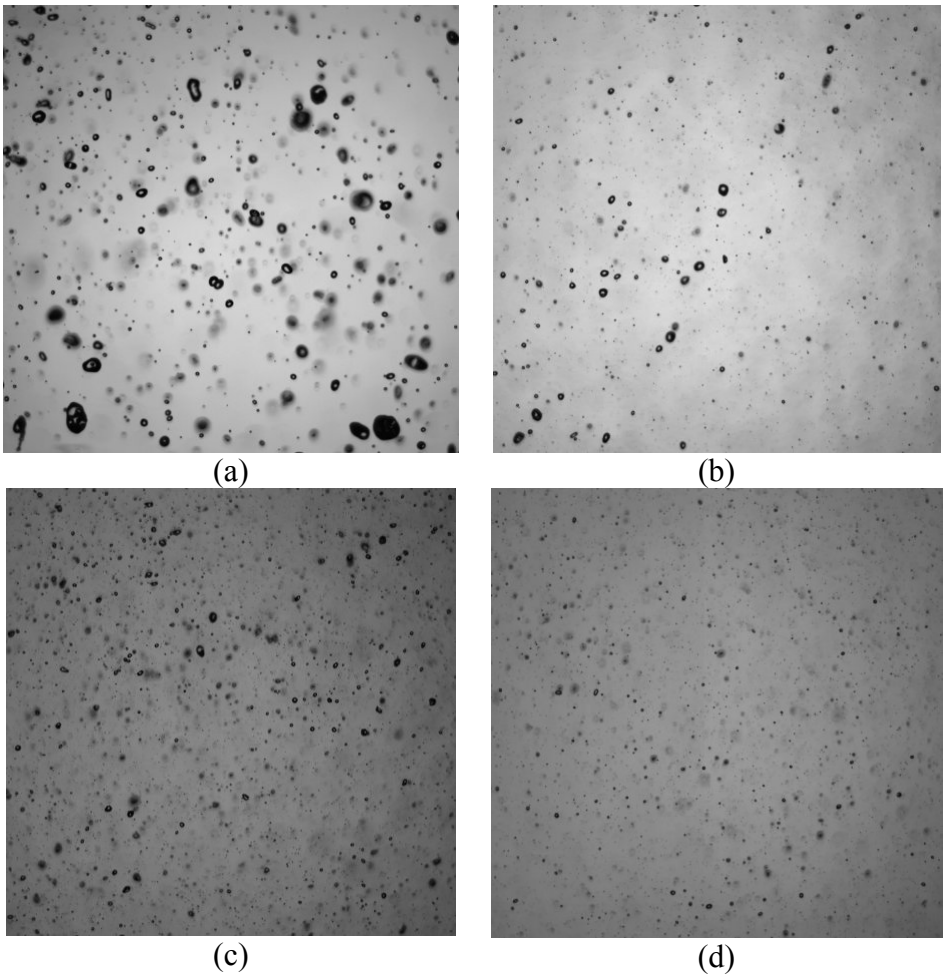

Figure A.2. Four representative images; (a) High drop density, large drop diameter, high image quality; (b) Low drop density, medium drop diameter, high image quality; (c) High drop density, medium drop diameter, low image quality; (d) High drop density, small drop diameter, low image quality.

Regardless of image quality and spray characteristics, the statistic drop size and drop number is sensitive to the post process settings for all images. Figure A.3 shows the drop size through different settings. The average drop size is the average of the 18 drop sizes by different post processing settings as described in Table A.1. Generally, the drop size decreases as the valid drop number when smaller droplets are recognized during the post processing. Using the recommended settings in the last row of Table A.1 may yield to recognize most of the droplets and the drop size is close to the average. This setting can be used as a universal setting for sprinkler spray post-processing in this study.

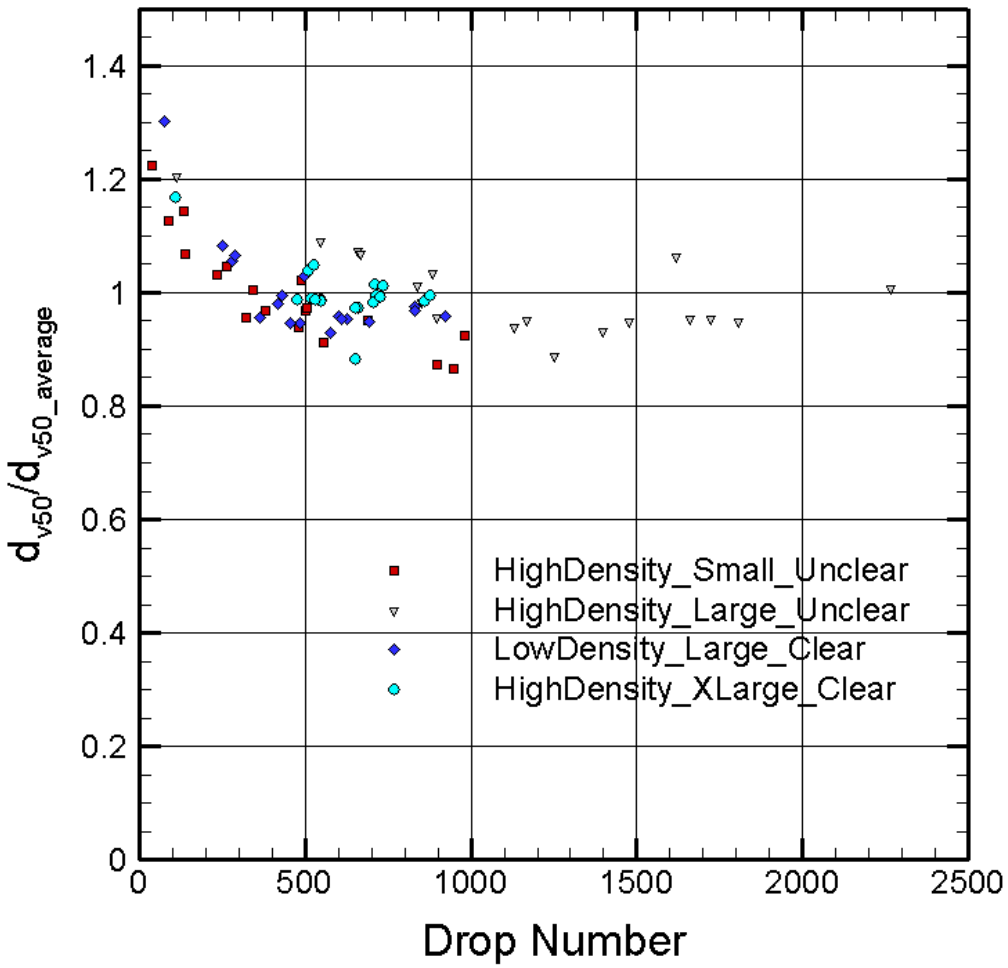

Figure A.3. Statistic drop size obtained from different post-processing settings for the four representative images. The drop size is normalized by the average drop size, which is obtained from different settings.

A.4 Post-Processing Analysis

The spatial spray distribution is not uniform and highly affected by the sprinkler geometry. In order to obtain the overall spray characteristics, the measurement area should be large enough to cover the whole spray area. In the near field, the sprinkler can be treated as a point where all the drops come from. In order to map out the detailed spray characteristics, the whole sphere with the sprinkler in the center should be covered.

However, because of the large amount of measurements, this is not feasible. In order to simplify the problem, the spray can be categorized as three basic flow streams with reference to the sprinkler geometry. They are tine, slot and arm streams. The tine streams and slot streams represent the largest share of the spray. And they are symmetric along the azimuthal direction. In this study, the tine streams and slot streams are the main objective of investigation. The measurement location is aligned with these two streams and perpendicular to the horizontal deflector plane; finally, the overall spray can be re-configured using these double stream characteristics, as shown in Figure A.4. The effective area used in the imaging area is a square of 15 cm × 15 cm. One single measurement would not be capable of covering the whole spray area representative of a generic stream. Therefore, several measurements at different locations are performed and then combined to build an overall detection. At each measurement location, 100 or 200 image pairs are taken depending on the spray density. The effective drop number after combining the various experimental data at different locations stands between 10^5 and 10^6, thus providing a smooth spray distribution.

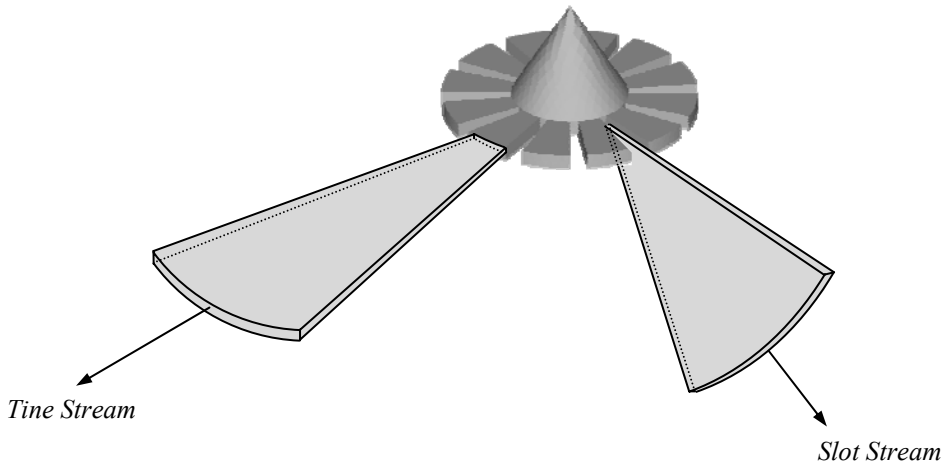

Figure A.4. Sheets Geometry

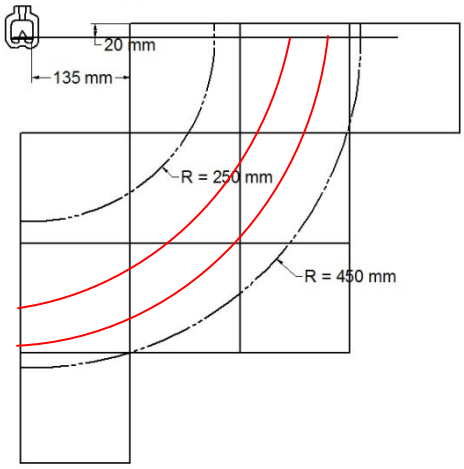

Figure A.5. Measurement Location

As discussed in previous section, border correction in this study appears to be unnecessary; on the other hand, depth-of-field correction is required. The depth of field is a function of drop size, *DOF(d)*, can be determined in the experiments. The data is post-processed in spherical coordinate as shown in Figure A.6, where θ is the elevation angle and ψ is the azimuthal angle. The measurement area is sub-divided into several concentric circles, each one having a vertical extension of 50 mm starting from 250 mm and ending at 400 mm. The droplets outside the concentric circle region are discarded. Drop size distribution is thus calculated every 50 mm. The volume fraction of drop-size distribution in a certain drop size bin range, $d_i<d_j<d_{i+1}$, is given by

$$f(d_i) = \frac{\sum_{d_i<d_j<d_{i+1}} d_j^3 u_j r_j \sin\theta_j / DOF(d_j)}{\sum_{j=1}^{N_{drop}} d_j^3 u_j r_j \sin\theta_j / DOF(d_j)}. \qquad \text{(A-1)}$$

Not only the overall drop size can be obtained, the local drop size is also available by applying Eq. (A-1) to a certain area, which is generically identified by an angular expression (e.g.: $[\theta, \theta+\Delta\theta]$, $[\psi, \psi+\Delta\psi]$).

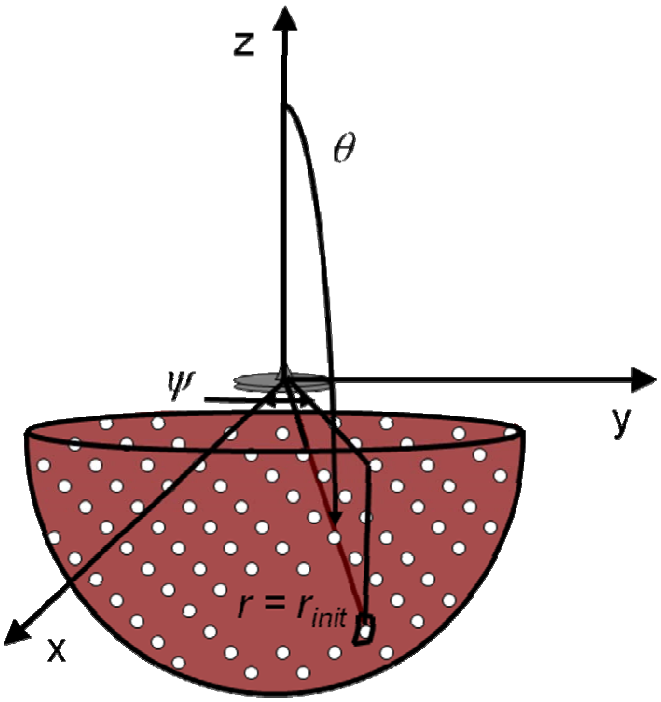

Figure A.6. Spherical ccoordinates for drop locations

Bibliography

1. NFPA *13 Code and Standard*. 2002, Quincy, MA.
2. Yu, H. *Investigation of Spray Patterns of Selected Sprinklers with the FMRC Drop Sizing Measuring System*. in *First International Symposium on Fire Safety Science*. 1986. New York.
3. Sheppard, D.T., *Spray Characteristics of Fire Sprinklers*, in *Mechanical Engineering*. 2002, Northwestern University: Evanston, IL, 60201. p. 206.
4. UL, *UL 199*: Chicago.
5. UL, *UL 1716: Chicago.*
6. NFPA, *NFPA Handbook*.
7. Chen, T.-S., *Measurements of water density and drop size distributions of selected ESFR sprinklers.* Journal of Fire Protection Engineering, 1994. **6**(2):.
8. White, F., *Viscous Fluid Flow*. 2006.
9. Prahl, J.M. and B. Wendt, *Discharge Distribution Performance for an Axisymmetric Model of a Fire Sprinkler Head.* Fire Safety Journal, 1988. **14**(1-2): p. 101-111.
10. Nam, S., *Development of a computational model simulating the interaction between a fire plume and a sprinkler spray.* Fire Safety Journal, 1996. **26**(1): p. 1-33.
11. Blum, A.F., *Discharge Characteristics of Canonical Sprinkler Sprays*, in *Fire Protection Engineering*. 2006, University of Maryland - College Park: College Park, MD, 20740.
12. Chen Yao, A.S.K., *Effect of Drop Size on Sprinkler Performance*, in *74th Annual Meeting of the National Fire Protection Association*. 1970: Toronto.
13. Dundas, P.H., *The Scaling of Sprinkler Discharge: Prediction of Drop Size*. 1974: Norwood.
14. S. J. Walmsley, A.J.Y., *A study of the spray produced by fire suppression sprinkler systems*, in *8th International conference on liquid atomization and spray systems*. July, 2000: CA, USA.
15. Do, C., *Stream-wise Discharge Characteristics of Pendant Sprinkler Sprays*, in *Department of Fire Protection Engineering*. 2009, University of Maryland: College Park.
16. Ning Ren, A.B., Ying-Hui Zheng, Chi Do, Andre W. Marshall, *Quantifying the Initial Spray from Fire Sprinklers*, in *9th Symposium on Fire Safety Science*. 2008, International Association of Fire Safety Science: Karlsruhe, Germany.
17. Gandhi PD, S.D., *Using PDPA in evaluation of sprinklers*, in *Fire Suppression and Detection Research Application Symposium*. 1999: Orlando, FL.

18. Widmann, J.F., D.T. Sheppard, and R.M. Lueptow, *Non-intrusive measurements in fire sprinkler sprays.* Fire Technology, 2001. **37**(4): p. 297-315.

19. Widmann, J.F., *Phase Doppler interferometry measurements in water sprays produced by residential fire sprinklers.* Fire Safety Journal, 2001. **36**(6): p. 545-567.

20. Putorti, A.D., *Simultaneous measurements of dro size and velocity in large-scale sprnkler flows using particle tracking and laser-induced fluorescence*, in *Mechanical Engineering*. 2004, University of Michigan - Ann Arbor: Ann Arbor, MI, 48109.

21. Wu, D., D. Guillemin, and A.W. Marshall, *A modeling basis for predicting the initial sprinkler spray.* Fire Safety Journal, 2007. **42**(4): p. 283-294.

22. Pilch, M. and C.A. Erdman, *Use of Breakup Time Data and Velocity History Data to Predict the Maximum Size of Stable Fragments for Acceleration-Induced Breakup of a Liquid-Drop.* International Journal of Multiphase Flow, 1987. **13**(6): p. 741-757.

23. Heskestad, G., *Proposal for Studying Interaction of Water Sprays with Plum in Sprinkler Optimization Program*. 1972: Norwood.

24. Dombrowski, N. and P.C. Hooper, *The Effect of Ambient Density on Drop Formation in Sprays.* Chemical Engineering Science, 1962. **17**(4).

25. Fraser, R.P., et al., *Drop Formation from Rapidly Moving Liquid Sheets.* Aiche Journal, 1962. **8**(5): p. 672-680.

26. Dombrowski, N. and W.R. Johns, *The Aerodynamic Instability and Disintegration of Viscous Liquid Sheets.* Chemical Engineering Science, 1963. **18**(3).

27. Grant, G., J. Brenton, and D. Drysdale, *Fire suppression by water sprays.* Progress in Energy and Combustion Science, 2000. **26**(2): p. 79-130.

28. Squire, H.B., *Investigation of the Instability of a Moving Liquid Film.* British Journal of Applied Physics, 1953. **4**(Jun): p. 167-169.

29. Lamb, *Hydrodynamics*. 1932, London: Cambridge University Press.

30. Hegerty, S., *A study of stability of plane fluid sheets.* Journal of Applied Mechanics, 1955. **22**.

31. Crapper, G.D., N. Dombrowski, and G.A.D. Pyott, *Large-Amplitude Kelvin-Helmholtz Waves on Thin Liquid Sheets.* Proceedings of the Royal Society of London Series a-Mathematical Physical and Engineering Sciences, 1975. **342**(1629).

32. Li, X.G. and R.S. Tankin, *On the Temporal Instability of a 2-Dimensional Viscous-Liquid Sheet.* Journal of Fluid Mechanics, 1991. **226**: p. 425-443.

33. Dombrowski, N., D. Hasson, and D.E. Ward, *Some Aspects of Liquid Flow through Fan Spray Nozzles.* Chemical Engineering Science, 1960. **12**(1).

34. Dombrowski, N. and P.C. Hooper, *The Performance Characteristics of an Impinging Jet Atomizer in Atmospheres of High Ambient Density.* Fuel, 1962. **41**(4): p. 323-334.

35. Weber, angew. Math Mech., 1931.

36. Hasson and Mizrahi, J. Trans. Inst. Chem. Engrs., 1961. **39**.

37. Weihs, D., *Stability of Thin, Radially Moving Liquid Sheets.* Journal of Fluid Mechanics, 1978. **87**(Jul): p. 289-298.

38. Huang, J.C.P., *Break-up of Axisymmetric Liquid Sheets.* Journal of Fluid Mechanics, 1970. **43**.

39. Clanet, C. and E. Villermaux, *Life of a smooth liquid sheet.* Journal of Fluid Mechanics, 2002. **462**: p. 307-340.

40. Villermaux, E. and C. Clanet, *Life of a flapping liquid sheet.* Journal of Fluid Mechanics, 2002. **462**: p. 341-363.

41. Lin, S.P. and W.Y. Jiang, *Absolute and convective instability of a radially expanding liquid sheet.* Physics of Fluids, 2003. **15**(6): p. 1745-1754.

42. Ren, N., *Analysis of Spray from Canonical Fire Suppression Nozzles*, in *Department of Fire Protection Engineering*. 2007, University of Maryland: College Park.

43. Ahmed, M., et al., *Characteristics of liquid sheets formed by splash plate nozzles.* Experiments in Fluids, 2008. **44**(1): p. 125-136.

44. Senecal, P.K., et al., *Modeling high-speed viscous liquid sheet atomization.* International Journal of Multiphase Flow, 1999. **25**(6-7): p. 1073-1097.

45. Paolo E. Santangelo, P.T., Beatrice Pluvirenti, Paolo Valdiserri, *DISCHARGE AND DISPERSION ANALYSIS in WATER MIST SPRAYS: Experimental and Numerical Analysis*, in *11th Triennial International Annual Conference on Liquid Atomization and Spray Systems*. 2009, ICLASS: Vail, Colorado, USA.

46. Watson, E.J., *The Radial Spread of a Liquid Jet over a Horizontal Plane.* Journal of Fluid Mechanics, 1964. **20**(3): p. 481-499.

47. Ibrahim, E.A. and T.R. McKinney, *Injection characteristics of non-swirling and swirling annular liquid sheets.* Proceedings of the Institution of Mechanical Engineers Part C-Journal of Mechanical Engineering Science, 2006. **220**(2): p. 203-214.

48. Yokoi, S., *Study on the prevention of Fire Spread Caused by Hot Upward Corrent*. 1960.

49. Yao, C. *Overview of Sprinkler Technology Research*. in *Fifth International Symposium of Fire Safety Science*. 1998.

50. G. Heskestad, R.G.B. *Modeling of thermal responsiveness of automatic sprinklers*. in *Second International Symposium of Fire Safety Science*. 1988.

51. Ruffino, P. and M. diMarzo, *The simulation of fire sprinklers thermal response in presence of water droplets.* Fire Safety Journal, 2004. **39**(8): p. 721-736.

52. Cooper, L.Y., *The interaction of an isolated sprinkler spray and a two-layer compartment fire environment. Phenomena and model simulations.* Fire Safety Journal, 1995. **25**(2): p. 89-107.

53. Li, K.Y., et al., *A mathematical model on interaction of smoke layer with sprinkler spray.* Fire Safety Journal, 2009. **44**(1): p. 96-105.

54. Alpert, R.L., *Numerical modeling of the interaction between automatic sprinkler sprays and fire plumes.* Fire Safety Journal, 1985. **9**.

55. Bill, R.G., *Numerical simulation of actual delivered density measurements.* Fire Safety Journal, 1993. **20**.

56. Chow, W.K., *Numerical simulation on cooling of fire-induced air flow by sprinkler water sprays.* Fire Safety Journal, 1991. **17**.

57. N. A. Hoffmann, E.R.G., N. C., Markatos, *Mathematical modelling of fire sprinkler systems.* Applied Math. Modeling, 1989. **13**.

58. Novozhilov, V., et al., *A computational fluid dynamics study of wood fire extinguishment by water sprinkler.* Fire Safety Journal, 1997. **29**(4): p. 259-282.

59. Hua, J.S., et al., *A numerical study of the interaction of water spray with a fire plume.* Fire Safety Journal, 2002. **37**(7): p. 631-657.

60. Novozhilov, V., *Fire Suppression Studies.* Thermal Science, 2007. **11**(2): p. 20.

61. Watkins, A.P., Heat and Mass Transfer and Combustion in Reciprocating Engines, 1989.

62. McGrattan, K., *FDS User Guide (Version 5)*. 2009.

63. McGrattan, K., *FDS Technical Reference Guide (Version 5)*. 2009.

64. Fleming, R.R., *Atuomatic Sprinkler System Calculations*. 2002, Qunicy, MA: SFPE Handbook.

65. LaVision, *Sizing Master Shadow*. 2007, Gottingen, Germany.

66. Malvern, *Malvern/INSITEC application note*. 1994.

67. Nam, S., *Numerical simulation of the penetration capability of sprinkler sprays.* Fire Safety Journal, 1999. **32**(4): p. 307-329.

68. Savart, F., *Memoire sur la consistitution des veines liquids lances par des orifices circularies en mince paroi.* Ann. De Chim., 1983. **53.**

69. Taylor, G., *The Dynamics of Thin Sheets of Fluid .2. Waves on Fluid Sheets.* Proceedings of the Royal Society of London Series a-Mathematical and Physical Sciences, 1959. **253**(1274).

70. Taylor, G., *The Dynamics of Thin Sheets of Fluid .3. Disintegration of Fluid Sheets.* Proceedings of the Royal Society of London Series a-Mathematical and Physical Sciences, 1959. **253**(1274).